

ULTRAFAST STUDIES OF IONIC LIQUIDS AND THE ROLE OF
NANOSTRUCTURAL ORGANIZATION

A DISSERTATION
SUBMITTED TO THE DEPARTMENT OF CHEMISTRY
AND THE COMMITTEE ON GRADUATE STUDIES
OF STANFORD UNIVERSITY
IN PARTIAL FULFILLMENT OF THE REQUIREMENTS
FOR THE DEGREE OF
DOCTOR OF PHILOSOPHY

Kendall Stanley Fruchey

May 2011

© 2011 by Kendall Stanley Fruchey. All Rights Reserved.
Re-distributed by Stanford University under license with the author.

This dissertation is online at: <http://purl.stanford.edu/dc048cw1328>

I certify that I have read this dissertation and that, in my opinion, it is fully adequate in scope and quality as a dissertation for the degree of Doctor of Philosophy.

Michael Fayer, Primary Adviser

I certify that I have read this dissertation and that, in my opinion, it is fully adequate in scope and quality as a dissertation for the degree of Doctor of Philosophy.

Hongjie Dai

I certify that I have read this dissertation and that, in my opinion, it is fully adequate in scope and quality as a dissertation for the degree of Doctor of Philosophy.

Richard Zare

Approved for the Stanford University Committee on Graduate Studies.

Patricia J. Gumpert, Vice Provost Graduate Education

This signature page was generated electronically upon submission of this dissertation in electronic format. An original signed hard copy of the signature page is on file in University Archives.

ABSTRACT

Ionic liquids are a quickly emerging class of neoteric solvents composed of organic and inorganic ions that remain liquid at room temperature. Their properties are diverse and often unique, bridging the continuum between polar and nonpolar, molecular and ionic. One property which has garnered special attention is the possibly ubiquitous existence of ordering in the bulk liquid, known as nanostructural organization. Resulting from the energetics of balancing the strong electrostatics of ions with steric considerations, it has been suggested that ionic liquids with sufficiently large alkyl substitutions should form distinct regions of polar and non-polar groups within the bulk solvent structure. The characteristics of this ordering, and even its very existence, have been heavily debated topics in ionic liquid research. Two ultrafast fluorescence experiments are discussed which attempt to assess the extent and role of nanostructural organization in the solvent properties of prototypical ionic liquids. Additionally, an Optical Kerr Effect study is described with the aim of understanding the role of Li in ionic liquid electrolytes.

Time dependent fluorescence depolarization measurements studied the rotational friction experienced by small charged and nonpolar dye molecules in a series of ionic liquids with increasing alkyl chain lengths. Two distinct behaviors were observed. For a charged pyranine-derivative dye, strong interaction between the dye molecules and ionic liquid leads to a greater rotational friction than the Debye-Stokes-Einstein hydrodynamic theory predicts. The magnitude of this increase scales with the size of the ionic liquid cation. For the nonpolar dye perylene, the rotational friction was less than the slip boundary condition of hydrodynamic theory. Moreover, increasing alkyl chain length

causes the rotational behavior to converge on that experienced by the dye in a purely alkane environment. The causes of these trends are discussed, leading to the conclusion that different regions of the nanostructured environment are being assessed. The nonpolar dye is segregated into the nonpolar region of the ionic liquid, so that the rotation friction describes the structure of this region. The charged dye is interacting with the ions in the hydrophilic region. The results shed light on some aspects of nanostructural organization as it applies to ionic liquids as solvents.

To assess the spatial characteristics of nanostructural organization, donor-donor excitation transfer was examined. The time dependence of the excitation transfer is strongly sensitive to the distribution of donors and acceptors in solution. Using a dye molecule that is anticipated to segregate into the nonpolar regions, the altered distribution of dye molecules resulting from nanostructural organization will be evident in the excitation transfer. Fluorescence depolarization can be used to monitor the excitation transfer. Observables for an isotropic and structured distribution of dye were calculated, and compared to fluorescence experiments. Based on the fits, an upper bound on the radius of 6-8Å is placed on the size of the hydrophobic regions of nanostructural organization, modeled as spheres.

The transport properties of ionic liquids as electrolytes are strongly and negatively affected by the addition of lithium. To understand this, Optical Heterodyne Detected Optical Kerr Effect studies were performed on a pure and lithium loaded imidazolium ionic liquid. Mode-coupling theory was tested in the pure liquid, and found to be capable of describing the dynamics. Mode-coupling theory was then used to understand the results in the lithium loaded samples. Changes in parameters from the mode-coupling

theory fits occur at a lithium mole fraction of 0.2. This is discussed in terms of outside MD simulations to understand and substantiate the changes in ionic liquid structure leading to the loss of ion mobility.

ACKNOWLEDGEMENTS

Spending likely 7% of your life in graduate school means there are a number of people to thank. First and foremost is my family. I can't even put into words what it means to have a spouse like Vanessa. Supporting me personally and financially, she is a soul mate of the finest caliber. So much can be said, yet none of it need be as her devotion was steadfast and unwavering. Although Genny arrived relatively late to the party, she too is an inspiration as I write and finish. My parents were always there, and necessarily so. To each of you I owe my eternal thanks.

I would also like to thank my advisor, Dr. Michael Fayer. His expectations and guidance helped me grow, both in technical realms as disparate as nonlinear optics to glassblowing, and also in defining my identity as a scientist. He was an outstanding resource. Another benefit of working for Mike is his uncanny ability to attract the best people to his lab. I have had the privilege of working with a number of people who impacted me deeply. Jie Li was my first student mentor, and showed infinite patience in teaching me as well as cleaning up my first year mistakes. Never let a first year near a spray duster. David Spry was also an outstanding mentor and friend, accepting me onto his system and giving me the tools to carry out the bulk of the research in this thesis. Ilya Finkelstein and Alexi Goun also helped me carry out experiments on their system, and provided unique perspectives on any task at hand.

Adam Sturlaugson deserves special commendation for joining my project during the hardest part of the laser build. He has endured four letter words to score a million points in scrabble, the agony of defeat far worse than a skier on Wide World of Sports, and yet throughout remained adamantly cheerful and committed. His work ethic is unrivaled, his

friendship unquestioned. Christian Lawler likewise has earned my thanks, for helping to build and maintain the fluorescence setup.

Friendships were as defining a characteristic as science during graduate school. A few are named, but none forgotten. Daniel Rosenfeld has always been a cherished source of conversation, comment, coffee, and opinion. Why go to Swain when he the library sits across from you? Jean Chuang was part climbing partner, part hiking adventurer, and fulltime friend. The “lunch table.” What would I have done without you? Sam, William, David, Griffin, Charles, Adrienne, Hassan, Amy, Noah, Mike, and others. This will likely come back to bite any of you in future political office. To Soup Night, to the Fayer Lab, to the Chemistry Support Staff, and to anyone who is still reading this far into a thesis acknowledgement section, “Thank you.”

TABLE OF CONTENTS

Abstract	iv
Acknowledgements	vii
List of Figures	xii
Chapter 1. Introduction to Room Temperature Ionic Liquids	1
1.1 Ionic Liquid Fundamentals	1
1.2 Nanostructural Organization	4
1.3 References	9
Chapter 2. Optical Heterodyne Detected Optical Kerr Effect	
Spectroscopy	11
2.1 Introduction to Optical Kerr Spectroscopy	11
2.2 References	16
Chapter 3. Time Correlated Single Photon Counting	17
3.1 Introduction to Time Correlated Single Photon Counting	17
3.2 Experimental Implementation	20
3.3 References	30
Chapter 4. Optical Kerr Effect Studies of Ionic Liquid / Lithium	
Mixtures	31
4.1 Introduction	31
4.2 Experimental Setup	36
4.3 Results and Discussion	38
4.4 Concluding Remarks	51
4.5 Acknowledgements	52

4.6 References	53
Chapter 5. Dynamics in Organic Ionic Liquids in Distinct Regions	
Using Charged and Uncharged Orientational	
Relaxation Probes	55
5.1 Introduction	55
5.2 Experimental Setup	58
5.3 Results and Discussion	60
5.3.1 Perylene	62
5.3.2 MPTS	68
5.4 Concluding Remarks	73
5.5 References	75
Chapter 6. Electronic Excitation Transfer Probing of Ionic Liquid	
Nanostructure	79
5.1 Introduction	79
5.2 Electronic Excitation Transfer Theory	82
5.3 Experimental Methods	88
5.4 Results and Discussion	91
5.4.1 Model Calculations	91
5.4.2 Experimental Results	97
5.5 Concluding Remarks	104
5.6 Acknowledgements	104
5.7 References	105
Appendix 1. Ti:Sapphire Oscillator System	109

A1.1 Introduction	109
A1.2 Theoretical Background	109
A1.3 Oscillator Construction	110
A1.4 References	123
Appendix 2. Other Experiments	124
A2.1 Introduction	124
A2.2 Berry Psuedorotation in Iron Pentacarbonyl	124
A2.3 Photoacid Dynamics in Hydrate Ionic Liquids	125
A2.4 2D-IR of Metal Carbonyls in Ionic Liquids	128
A2.5 References	132

LIST OF FIGURES

Figure 1.1	Examples of Ionic Liquids	2
Figure 3.1	Principles of TCSPC.....	18
Figure 3.2	TCSPC Experimental Setup.....	21
Figure 4.1	Time Dependent OKE Signal for Pure Bmim NTf ₂	39
Figure 4.2	Temperature Dependent Power Law Coefficients of Bmim NTf ₂	39
Figure 4.3	Mode Coupling Scaling Laws for Bmim NTf ₂	41
Figure 4.4	Phase Transition of Mode Coupling Parameters.....	44
Figure 4.5	Power Laws of Lithium Loaded Ionic Liquid.....	45
Figure 4.6	Debye-Stokes-Einstein Plot for Lithium Mixture	47
Figure 4.7	Mode Coupling Parameters for Lithium Mixture	48
Figure 5.1	Probe Molecule Structures	57
Table 5.1	Shape and Slip Coefficients	62
Figure 5.2	DSE Plot for Perylene.....	63
Table 5.2	Rotational Frictions for Perylene	64
Table 5.3	Ratios of In-plane to Out-of-plane Rotation	65
Figure 5.3	Fluorescence Spectra of Perylene	66
Figure 5.4	DSE Plot for MPTS	69
Table 5.4	Rotational Frictions for MPTS.....	69
Figure 5.5	Fluorescence Spectra of MPTS.....	71
Figure 6.1	Fluorescence Spectra of 9PA	90
Figure 6.2	<G> for Various Model Calculations	92

Figure 6.3	$\langle G \rangle$ for Different Volume Fractions.....	94
Figure 6.4	$\langle G \rangle$ for Different Sphere Packings.....	95
Figure 6.5	Isotropic Fits to the Data.....	98
Figure 6.6	Clustered Sphere Fits to the Data.....	99
Figure 6.7	Regularized Clustered Sphere Fits to the Data	102

Chapter 1: Introduction to Room Temperature Ionic Liquids

1.1 Ionic Liquid Fundamentals

Room temperature ionic liquids (RTILs) are a broad class of relatively new and rapidly evolving molten salts. They are defined as those ionic salts whose melting point is at or below 100°C. Although certain eutectic mixtures of inorganic ions satisfy this definition, the current interest in RTIL research focuses on combinations of ions that include largely substantial organic functionality. Historically, these are first linked to discoveries by Walden that combined certain organic amines and nitric acid and resulted in a conjugate salt that remained liquid even when dehydrated. Though several examples of these protic ionic liquids, as they are now referred to as, were found, the field of ionic liquids remained largely a laboratory curiosity rather than a full fledged field. In fact, the field remained almost completely dormant for almost 60 years, until a mini-renaissance in the 1970's with the discovery that certain combinations of alkyylimidazolium and tetrahaloaluminate yielded a viscous molten salt. At the peak of the oil crisis and with large research efforts underway into fuel cell and battery technologies to solve energy problems, these conductors were considered under a variety of circumstances. As the oil shocks faded and with the increased appreciation for the difficulty in working with the highly unstable tetrahaloaluminate, the field once again subsided. This was a much shorter period of inactivity, as the development of non-coordinating ions to replace the dangerous tetrahaloaluminate created the third Renaissance in RTIL research that is continuing to this day.

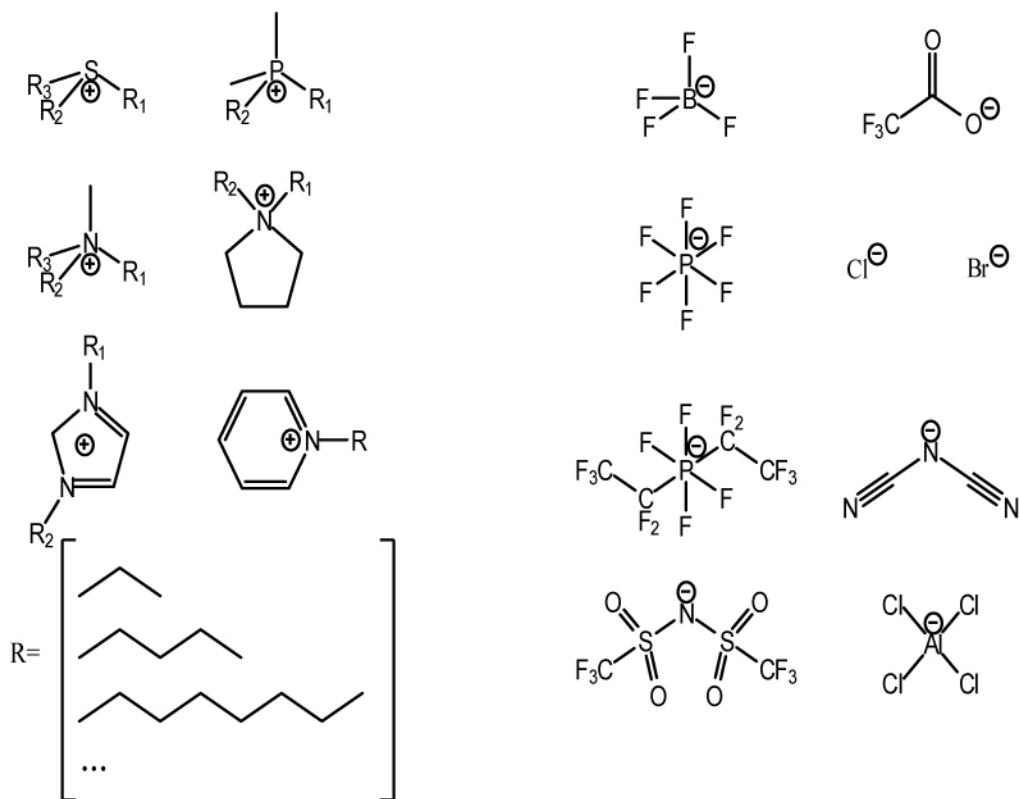


Figure 1.1 Examples of ion combinations that result in aprotic ionic liquids.

The term RTIL is a very broad umbrella under which several different subcategories of similar properties have emerged. The first division is between the protic and aprotic ionic liquid. Most often conceived of when discussing RTILs in literature, the aprotic class has garnered the most research activity and initial interest. In some sense, this is as much a consequence of historical inertia as it is a result of the differences in physical properties which lend themselves to perceived applications. There are a wide range of chemical functionalities present, some of which are demonstrated in Figure 1.1. The key feature is alkylation to create a cationic heteroatom. Before discussing the properties of these ionic liquids, the very notion of such a description needs to be strongly qualified. While certain properties such as non-volatility are common, the richness of discoveries in

the ionic liquid field over the last decade have rendered exemptions to almost every rule and heuristic. The risk of generalizing is to discount these exceptions, many of which are at least as important if not more so than those that follow the rule.

None the less, there are a number of fairly universal properties that make RTILs interesting candidates for a number of applications, as well as fundamentally interesting subjects by themselves. The strong ionic forces render many ionic liquids completely non-volatile, at least over the temperature range for which they are chemically stable. Exceptions to this *cause célèbre* now abound, but initially were almost entirely discounted. The non-volatility of the ionic liquid first earned them the moniker of “green solvents,” as they could in theory be almost indefinitely reused. It is somewhat ironic that compounds which are often highly halogenated, toxic, and frequently non-biodegradable were so heavily touted for their green credentials – a view that has receded with further understanding¹. Even without an appeal to their greenness, the nonvolatility makes ionic liquids attractive for reactions and separations². As ionic solutions with wide electrochemical windows, they are often ideal candidates for electrical applications such as electrolytes³ and electrodeposition⁴. What the ionic constitution is of the ionic liquid electrolyte is an oft debated subject. Plots of conductivity vs viscosity, the so called Wald plot, show deviations from linearity. The first interpretation of these results was that the bulk liquid shows strong ionic pairing, leading to the concept of “ionicity,” or how much the constituent ions behave independently^{5,6}. While not fully understood, it blurs the line between associating (molecular like) and ionic (dissociated) characteristics of the bulk ionic liquid.

Protic ionic liquids are combinations of acids and bases that, upon transfer of the proton, lead to an ion pair of sufficiently low melting point. Some examples are salts from alkyl amines or methyl imidazole combined with mineral acids like nitric acid. These tend to be more strongly associating ionic liquids, as evidenced by the fact that a large percentage of them are distillable. In some sense, this makes protic ionic liquids less attractive, as the non-volatility of ionic liquids is one of their major points of interest. For this and other technical reasons, the result has been that protic ionic liquids remain somewhat less studied than their aprotic counterparts. Most indications are that the protic RTILs seem to share most of the key traits of aprotic ionic liquids⁷. Moreover, the acid/base functionality of protic RTILs has particularly lent them to industrial applications. An example is the BASIL process, or Biphasic Acid Scavenging using Ionic Liquids, which is the flagship case of an industrial transformation using ionic liquids. It uses an alkyl imidazole base to form the protic ionic liquid 1-H-3-alkylimidazolium chloride on encounter with HCl byproduct. The proto-ionic liquid base is then regenerated via proton extraction. This process highlights a number of the properties of interest that have motivated work on ionic liquids, including their phase stability, chemical stability, and non-volatility.

1.2 Nanostructural Organization

One property of both protic and aprotic RTILs which has been of strong interest in the physical chemistry community is the concept of nanostructuring in ionic liquids. The exact definition of nanostructuring, *vide infra*, has remained elusive. Several explanations and descriptions abound, with the ineffability underscoring the confusion on the matter. The structure of many prototypical ionic liquids is very amphiphilic, with

hydrophilic and hydrophobic sections. These regions are often described in terms of head and tail groups, borrowed from the surfactant lexicon. An ionic liquid like 1-alkyl-3-methylimidazolium would therefore be described as having a polar, hydrophilic “head” of the imidazolium ring and anion group, as well as a nonpolar “tail” formed by the alkyl chain. For short alkyl chains the line is a blurry one, but for longer alkyl chains the system clearly resembles a number of surfactants. Nanostructuring, also called nanostructural segregation or nanostructural heterogeneity, describes the tendency for the two systems to separate in the bulk liquid phase. From the geometric properties of the molecule, this is frequently described in terms similar to micelle formation. The non-polar alkyl tails coalesce into a hydrophobic pocket, surrounded by thin layers of head groups forming hydrophilic channels. The cause of this separation is energetic. The Coulomb force for bare ions is very large, such that satisfying the charge ordered layering of cations and anions together to minimize the Coulomb force dominates the structure. The process is similar to accommodating and minimizing Madelung energy in an ionic crystal. In the ionic liquid, the optimal strategy for minimizing this force is the expulsion of the tails from the charged regions to allow better ion solvation.

While elements of selective solvation are not unusual in liquid structure, the strength and persistence of the domains created by nanostructural organization were somewhat unexpected. They were first detected in the radial distribution functions and spatial distributions generated from computational studies.^{8,9} Even from these simulations, the characteristics were difficult to ascertain. While only defined in its broadest sense, the discoveries none the less motivated substantial effort to delineate the extent to which the structures captured in MD simulations bore out in reality. This is a difficult task, as the

nanostructuring is not well organized and persistent only on moderate timescales, i.e. nanoseconds. While early evidence was suggestive¹⁰⁻¹², the first major experimental find was a strong pre-peak in the liquid X ray scattering¹³. The X ray data had all of the hallmarks expected of nanostructuring in the RTIL. It was weak or non-existent for alkyl chains that were too short, less than butyl. The length scale it was correlated with increased approximately linearly with increasing alkyl chain length, as well as the definition and strength of the peak. This feature was then found in a number of ionic liquids¹⁴⁻¹⁸, and nanostructuring became reasonably established and assumed to be widespread throughout many different functionalities of ionic liquids.

Recently, the concept of nanostructural organization has been challenged on a number of fronts. The two strongest challenges were from attempts to understand the underlying sources of the X ray scattering data. The basis of the challenge is the question of what particular feature is causing the well resolved pre-peak in the X ray scattering data. These features, known as the first sharp diffraction peak or FSDP, are not unique to ionic liquids. They appear in many amphiphilic systems, such as long chain alcohols. Although there are also elements of selective solvation and hydrogen bonding structure that could be interpreted similarly to the nanostructuring in RTILs, the scattering from these systems are generally interpreted in terms of a second solvation shell effect. From this point of view, the scattering results from next nearest neighbor head groups that are displaced by the long alkyl tail. This interpretation was supported by neutron scattering experiments using deuterium contrasting¹⁹. Since D substitution changes the phase of the scattering signal, selectively deuterating regions of interest can highlight which features in the scattering have their origins on these atoms. Using this process, it was shown that

the neutron scattering, which also contains a prepeak similar to that found in the X ray scattering, resulted from the head groups and not the alkyl chains. Thus, the length dependence in the peak position of the FSDP was the result of increased displacement of the second solvation shell, and not a growing hydrophobic region.

Attempting to resolve these competing points of view, simulations were used to compute radial distribution functions and simulate scattering observables²⁰. The results partially harmonize the tension between the numerous simulations suggesting nanoscale heterogeneity with the lack of direct experimental evidence. Based on their results, the second coordination shell model seems to fit the data, but with a strong catch. The structuring of the ionic liquid to produce this strong second coordination shell effect shows strong similarities to the crystal structure. This structure includes regions of overlapping tails, similar to what is proposed for the structure of the hydrophobic domains. Therefore, while the scattering itself is not resulting from the domains, the second coordination shell provides indirect evidence for their existence. There is still considerable disagreement on this issue, with many experiments being proposed to bridge the gap.

The importance of nanostructuring is significant for many of the applications for ionic liquids. The concept of task-specific ionic liquids, that is building specific functionality into the solvent to actively participate in some facet of the chemistry of interest, depends heavily on incorporating these design parameters. Moreover, evidence from numerous spectroscopic studies^{21,22} and reactions²³ have indicated a rich, hidden layer of interactions between the ionic liquid and solute. From a design point of view, the

importance is on classifying the structure at a level that avoids tautology – with distance and time scales being two important parameters of interest.

1.3 References

- (1) Nelson, W. *Ionic Liquids*; American Chemical Society, New York, 2002; Vol. 818.
- (2) Wasserchild, P. a. W., T. *Ionic Liquids in Synthesis*; Wiley: New York, 2008.
- (3) Seki, S.; Ohno, Y.; Kobayashi, Y.; Miyashiro, H.; Usami, A.; Mita, Y.; Tokuda, H.; Watanabe, M.; Hayamizu, K.; Tsuzuki, S.; Hattori, M.; Terada, N. *J. Electrochem. Soc.* **2007**, *154*, A173.
- (4) Endres, F., MacFarland, D., and Abbott, A. *Electrodeposition from Ionic Liquids*; Wiley: New York, 2010.
- (5) MacFarlane, D. R.; Forsyth, M.; Izgorodina, E. I.; Abbott, A. P.; Annat, G.; Fraser, K. *Phys. Chem. Chem. Phys.* **2009**, *11*, 4962.
- (6) Ueno, K.; Tokuda, H.; Watanabe, M. *Phys. Chem. Chem. Phys.* **2010**, *12*, 1649.
- (7) Angell, C. A.; Byrne, N.; Belieres, J.-P. *Acc. Chem. Res.* **2007**, *40*, 1228.
- (8) Canongia Lopes, J. N. A.; Padua, A. A. H. *J. Phys. Chem. B.* **2006**, *110*, 3330.
- (9) Wang, Y.; Voth, G. A. *JACS* **2005**, *127*, 12192.
- (10) Mandal, P. K.; Sarkar, M.; Samanta, A. *J. Phys. Chem. A* **2004**, *108*, 9048.
- (11) Shigeto, S.; Hamaguchi, H.-o. *Chem. Phys. Lett.* **2006**, *427*, 329.
- (12) Iwata, K.; Okajima, H.; Saha, S.; Hamaguchi, H.-o. *Acc. Chem. Res.* **2007**, *40*, 1174.

- (13) Triolo, A.; Russina, O.; Bleif, H. J.; Cola, E. D. *J. Phys. Chem. B* **2007**, *111*, 4641.
- (14) Triolo, A.; Russina, O.; Fazio, B.; Triolo, R.; Di Cola, E. *Chem. Phys. Lett.* **2008**, *457*, 362.
- (15) Xiao, D.; Hines, L. G.; Li, S.; Bartsch, R. A.; Quitevis, E. L.; Russina, O.; Triolo, A. *J. Phys. Chem. B* **2009**, *113*, 6426.
- (16) Atkin, R.; Warr, G. G. *J. Phys. Chem. B* **2008**, *112*, 4164.
- (17) Kennedy, D. F.; Drummond, C. J. *J. Phys. Chem. B* **2009**, *113*, 5690.
- (18) Greaves, T. L.; Kennedy, D. F.; Mudie, S. T.; Drummond, C. J. *J. Phys. Chem. B* **2010**, *114*, 10022.
- (19) Hardacre, C.; Holbrey, J. D.; Mullan, C. L.; Youngs, T. G. A.; Bowron, D. *T. J. Chem. Phys.* **2010**, *133*.
- (20) Annapureddy, H. V. R.; Kashyap, H. K.; De Biase, P. M.; Margulis, C. J. *J. Phys. Chem. B* **2010**, null.
- (21) Castner, E. W.; Margulis, C. J.; Maroncelli, M.; Wishart, J. F. *Ann. Rev. Phys. Chem.* **2011**, *62*, 85.
- (22) Hardacre, C.; Holbrey, J. D.; Nieuwenhuyzen, M.; Youngs, T. G. A. *Acc. Chem. Res.* **2007**, *40*, 1146.
- (23) Earle, M. J.; Katdare, S. P.; Seddon, K. R. *Organic Letters* **2004**, *6*, 707.

Chapter 2: Optical Heterodyne Detected Optical Kerr Effect Spectroscopy

2.1 Introduction to Optical Kerr Spectroscopy

Optical heterodyne detected optical Kerr effect spectroscopy (OKE) is a non-linear, non-resonant ultrafast experiment useful for accessing several types of dynamics. OKE spectroscopy was first demonstrated as early as 1969 using q-switched lasers¹. Modern optical Kerr experiments nearly universally use the power Ti:Sapphire oscillator to achieve sub-100 fs time resolution. Conceptually, OKE monitors the decay of an induced birefringence caused by the strong optical pulses. The system is stimulated with a strong pump pulse, creating through various mechanisms a partial alignment in liquid. This makes the liquid birefringent, which can be monitored via the depolarization of a time delayed optical probe pulse. As the orientational alignment created by the pump fades through various orientational diffusion processes, the birefringence signal decays. The end result is an observable that can be connected to many of the orientational relaxation processes in the bulk liquid. OKE spectroscopy benefits from several advantages over many other non-linear techniques. It is probe free, and so it can measure dynamics in a system unperturbed by interloping probe molecules. Because it involves no excited state populations, it is not limited by any excited state lifetime. This allows OKE spectra to be taken over many decades of time, as opposed to the normal limitation of five lifetimes where population decay is involved. It is not unreasonable to follow a signal from 10's of femtosecond librations all the way out to 10 microsecond orientational diffusion. This is rather unique, and useful when considering a hierarchy of relaxation mechanisms.

Being non-resonant, the technique can be performed using any non-absorbing laser spectrum. This obviates the need for parametric conversion, greatly simplifying the laser design. The response functions that OKE spectroscopy measure are the same as measured by depolarized light scattering. The advantage in using OKE is a dramatic increase in signal to noise, and broader timescale coverage without shifting equipment (as going from digital autocorrelation to interferometry in light scattering).

More rigorously, OKE spectroscopy is a four-wave mixing technique that accesses certain components of the $\chi^{(3)}$ optical response tensor of the material. For isotropic systems, the component is the isotropic response $\chi_{xyxy}^{(3)}$. The signal is therefore the convolution of the electric fields of the pump and probe with this response function

$$S_i(t) = \iiint E_{pump}(t-t_1)E_{pump}(t-t_2)E_{probe}(t-t_3)\chi_{ijk}^{(3)}(t-t_1, t-t_2, t-t_3) \quad (2.1)$$

There are two interactions with the pump, and one with the probe. The indices refer to polarization dependent components. This material response is connected to the Kerr response of the material, Δn , which is an intensity dependent difference in the refractive index of the two polarized components

$$S(t) = \Delta n(t) = n_{\parallel}(t) - n_{\perp}(t) \quad (2.2)$$

In a typical experiment, an amplified ultrafast pulse is beam split, with the larger component of the power constituting the pump. The pump beam is well polarized with a Glan-Thompson polarizer, and then focused through the sample. This creates the orientational alignment previously mentioned. The probe is first variably time delayed, so that the entire material response can be mapped in time. It is then well polarized at an angle 45° relative to the pump beam. In a homodyne experiment, this 45° beam would then be focused on the excited volume of the sample. Like a polarized beam interacting

with a wave plate, the probe will interact with the birefringence and emerge elliptically polarized – the strength of ellipticity being determined by the refractive index difference and path length. The ellipticity is measured through an analyzing polarizer. By chopping the pump and probe, various scattering components are removed, as well as background signals. Lock-in detection at the characteristic frequency of the chopping scheme thereby affords substantial improvements in signal to noise.

In these experiments, heterodyning can substantially improve the signal to noise of the measurement. To heterodyne, a quarter wave plate is introduced in the probe beam after the setup polarizer. It is rotated slightly, creating a small ellipticity in the probe beam. After interacting with the sample birefringence, the polarization rotated component of the probe field can mix with this field of the probe created by the quarter wave plate. Since the fields add, the square law intensity at the detector is the sum of a both homodyne components, as well as a cross term between the local oscillator (the field created by the wave plate), and the signal. The homodyne signals can be removed through a combination of chopping and phase modulation, because both phases of the local oscillator can be created by the quarter wave plate. The heterodyne signal is stronger than the homodyne signal, and also linearly proportional to the signal instead of quadratically. At long times, this is important for preserving signal to noise. Phase modulating also removes any electrical noise through subtraction.

Microscopically, the birefringence can be interpreted as an alignment of the molecules in response to the pump pulse. The mechanisms through which the molecules are aligned are two-fold. The first is through a torque caused by the intense electric field of the pump. For a molecule that is anisotropically polarizable, the interaction with the field

creates a dipole whose energy is minimized when oriented along the field. Since the field can induce a dipole, it is only a difference in polarizability that is required, and not a permanent dipole. This does disqualify a small class of high symmetry molecules, although they too can be aligned through higher order effects. The magnitude of the alignment is dependent on several related parameters. The first is the strength of the electric field, determined by the pulse energy. The upper limit on this is usually the threshold for white light generation on short pulses, and local heating and lensing at longer times. Stretching the pulses to alleviate white light generation allows more power to be used, and more signal to be generated. The total alignment is going to be inversely proportional to the viscosity of the sample. For very viscous samples such as glasses, the small signals created for this reason can be problematic. A second mechanism for creating the alignment comes from stimulated Raman modes. For sufficiently broadband laser pulses, different colors can mix to drive low frequency Raman modes. While in itself a very interesting and rich source of information on liquids that is only cleanly accessible using OKE, the Raman modes are preferentially driven along the axis of the laser. These vibrating molecules are partially aligned, with the same end result as in the case of orientation through the AC Kerr effect.

Once the ensemble has been partially aligned, it is allowed to evolve field-free for a period of time. During this time, the collective orientational relaxation tends to relax the system and remove the alignment. A distinguishing feature of OKE vs. other techniques that measure orientational relaxation is that OKE measures the total or collective orientational correlation function. This is opposed to the single molecule correlation function, as measured by techniques such as NMR. For situations in which the induced

dipole of nearby molecules does not couple neighbors, the collective orientational correlation function becomes the single molecule correlation, scaled by a factor that depends on geometry and alignment. In isotropic systems, the two are equal². Although all modes collectively work together to relax the alignment, the dominant mode at short time is the libration. Librations correspond to frustrated, oscillating rotations caused by the presence of neighbors. These are sensitive to the interactions and packing of molecules, which is one reason for OKE's sensitivity to liquid structure. At longer times, the orientational diffusion requires the correlated motions of more and more molecules to relax. This culminates in the global relaxation of the solvent. In this regime, the molecules are assumed to undergo rotational diffusion, which means the signal should decay exponentially as the sum of up to 5 weighted exponentials (corresponding to sums and differences of the inertial axes). In practice, the similarity of the different time constants generally yields only one resolvable decay time. This is the particle rotation time, which is connected to the bulk transport properties of the solution.

2.2 References

- (1) Duguay, M. A.; Hansen, J. W. *Applied Physics Letters* 1969, *15*, 192.
- (2) Zhong, Q.; Fourkas, J. T. *J. Phys. Chem. B.* 2008, *112*, 15529.

Chapter 3: Time Correlated Single Photon Counting

3.1 Introduction to Time Correlated Single Photon Counting

Time correlated single photon counting (TCSPC) is a method for measuring the time dependence of repeated events. It is differentiated from the majority of other ultrafast optical techniques in that time resolution is generated chronographically from single events, as opposed to pump-probe type measurements where the time dependence is generated from an optical delay of multiple interactions with the system. The method affords numerous advantages, but is limited to processes on the many picoseconds timescale on account of the limits of fast electronics. For the case of fluorescence, for which lifetimes are frequently a few nanosecond, and molecular rotations occurring on 100 picosecond or greater timescales, the technique is well suited.

TCSPC is conceptually based on the idea of building a waveform by sampling single events from its underlying probability distribution. By repeatedly sampling the function, a histogram can be built from which the waveform itself can be recreated. In fluorescence TCSPC, the waveform is the time dependent fluorescence intensity. The time dependence is created by measuring the arrival time of individual fluorescence photons, relative to an ultrafast UV pulse that excites the chromophores. These arrival times are binned to form a histogram representing the time dependence of the underlying process. This process is depicted in Figure 3.1.

The key requirement for TCSPC is fast repeatability of the measurement. Because the distribution is built up from single events, a significant number of samplings must be made. For uncorrelated rare events defined by an independent probability distribution, the error in any measurement channel is going to be Poisson distributed, meaning the

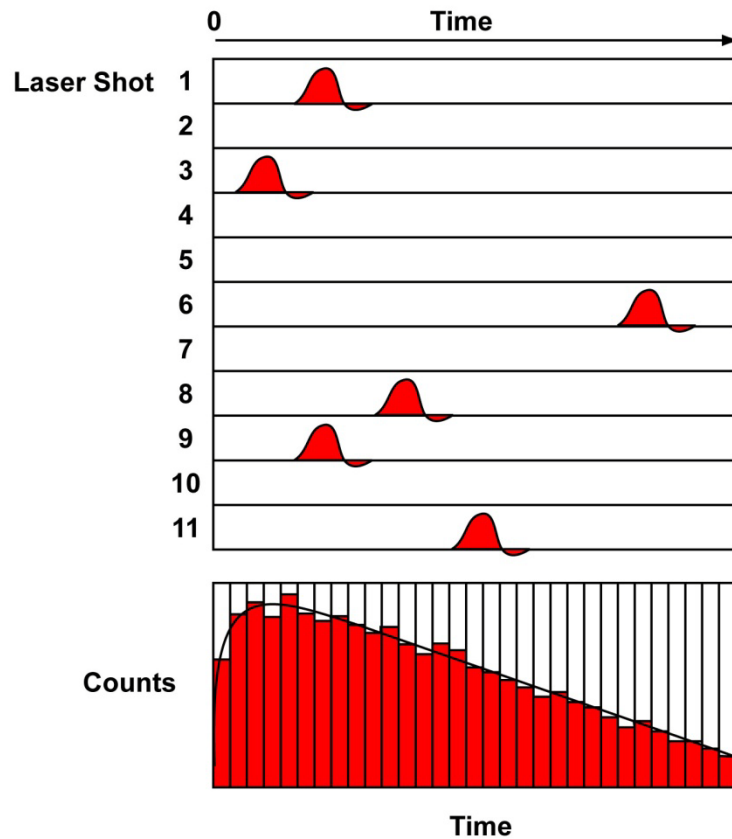


Figure 3.1 The principles of TCSPC. For each laser shot, the single photons are collected and binned in time. Repeated application of this process leads to a histogram representing the time dependence of the process.

variance scales as the mean. Thus, the relative error in any bin scales inversely to the square root of number of counts. At 40kS/s, this enables a simple lifetime measurement to be performed in a couple of minutes with significant accuracy. The method also benefits from the inherent linearity across many decades of signal. Because each photon is measured at the same intensity level in a binary event/no-event manner, there is almost no nonlinearity in the intensity. Coupled with the ability to quickly accumulate

significant counts, TCSPC is able to reliably access dynamics happening at 5 or more lifetimes without distortion.

Besides TCSPC, there are primarily two other techniques for arriving at the time dependent fluorescence intensity, which will briefly be discussed and compared to TCSPC. The first is fluorescence modulation, which sinusoidally varies the intensity of the excitation source¹. The finite duration of the fluorescence lifetime creates a time lag in the fluorescence intensity relative to the excitation modulation. Using lock-in amplification, this phase lag can be very accurately measured. Compared to TCSPC, the primary benefit of this approach is that it can be done using a conventional light source, or with a CW laser – both of which are far less expensive than a Ti:Sapphire laser. The chief disadvantage is that, compared to TCSPC which measures the full time dependence of the fluorescence response in the time domain, modulation based approaches measure only a single quantity. The fact that only a single observable is measured makes model selection much more difficult. For a single component lifetime this is not a serious problem, but for more complex systems such as those with excitation transfer, this can be a severe hindrance.

The other technique that competes against TCSPC is fluorescence up-conversion. Here, two ultrafast pulses are used. The first excites the sample, similarly to TCSPC. But whereas the fluorescence is directly detected in TCSPC, in fluorescence up-conversion, a second ultrafast pulse is used to up-convert the fluorescence, i.e. frequency summed in a non-linear crystal. The interaction between the two fields in the non-linear crystal in effect selects only the fluorescence intensity occurring at the time delay of the second pulse, which is varied. The chief benefit of this technique is the time resolution.

This is determined by the time duration of the amplified optical pulses, which can easily be made less than 100fs. This is in contrast to the 30ps instrument response function in TCSPC. For the fastest processes, fluorescence up-conversion is essential. However, the inefficiency of the up-conversion process makes the signal to noise vastly inferior to that which can be done using TCPSC. Also, while both systems require a Ti:Sapphire oscillator, the up-conversion usually also requires amplification, which substantially increases the cost and operational complexity. Similar to up-conversion, electronic pump-probe spectroscopy can monitor the evolution of the excited state, from which the stimulated emission provides information similar to the fluorescence. It is similar in advantages and disadvantages to fluorescence up-conversion.

3.2 Experimental Implementation

Figure 3.2 is a diagram of the experimental setup. The excitation source for the experiment is a Spectra-Physics Mai Tai Ti:Sapphire laser. The system is designed as a turn-key passively mode-locked Ti:Sapphire oscillator which is tunable over the range of 710nm to 950nm through the inclusion of an intra-cavity slit. The slit is placed in the frequency dispersed segment of the prism dispersion compensators. The system is designed to produce between 1.2 to 1.9W of power at 80 MHz repetition rate, corresponding to 15 to 24 nJ per pulse. The pulses are not transform limited, with approximately 150fs FWHM and a bandwidth of 20nm. The Mai Tai output is synchronized with a fast acousto-optical modulator, which is used to downsample the excitation to 4 MHz. This is done because the time between pulses sets an effective window in which the fluorescence can be measured. For an event lasting longer than the excitation period, there will be ambiguity as to which excitation shot the event is

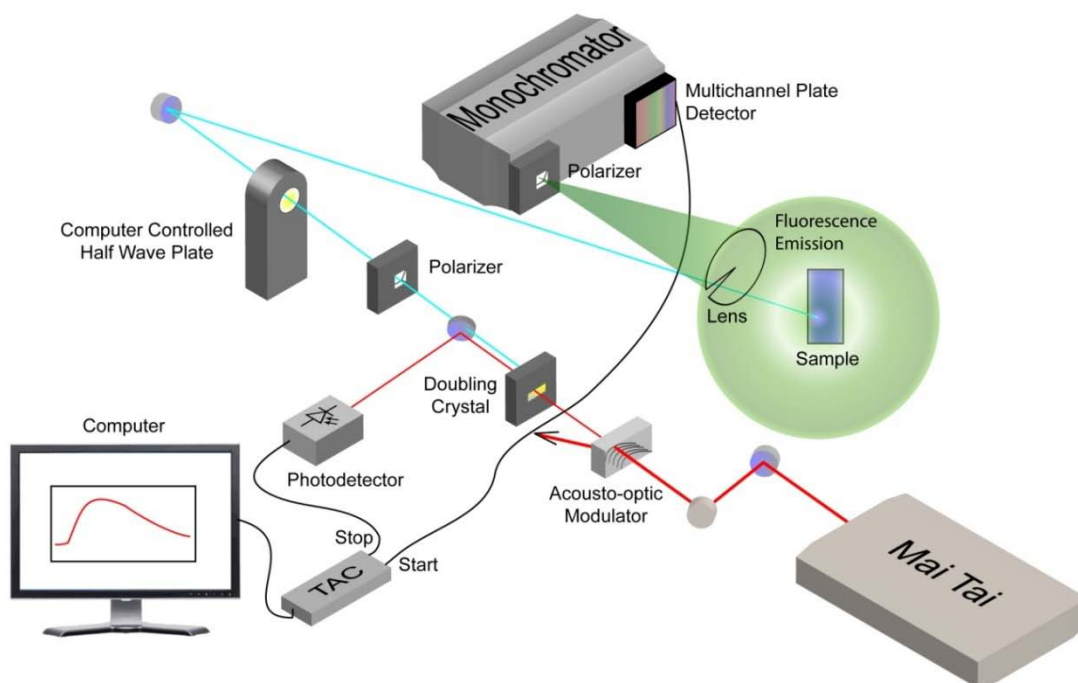


Figure 3.2 The experimental layout of the time correlated single photon counting system.

correlated with, and therefore aliasing. 4MHz is the fastest the current Si acousto-optic modulator can be run, which correlated with the maximum synchronization rate of previous generation of electronics. The new electronics can operate at much higher speeds, including count rates of up to 10 MHz. Since the time window afforded by most dyes is on the order of 50ns, the pulse selection rate could easily be doubled with an upgrade to the acousto-optic modulator to permit faster data collection.

The downsampled pulse train from the acousto-optic modulator is focused onto a type I beta-barium borate (BBO) crystal to generate second harmonic light in the region of 355 to 475nm. This overlaps well with the absorption spectrum of a number of mid-sized chromophores. The doubled light is separated from the fundamental using a Glan-Taylor

prism, since the doubled light is of opposite polarization in type I doubling. The fundamental is focused onto a fast Si PIN photodiode to generate a reference timing signal. The now well polarized second harmonic is sent through a computer controlled half wave plate. This will allow arbitrary polarization selection of the excitation beam relative to the analyzing polarizer, which is fixed in the lab frame. This is done because the gratings in the monochromator are polarization sensitive, which makes rotating the analyzer infeasible. The excitation beam is then impinged on the sample through a slit in the collecting lens at a small angle to minimize the depolarization from the metal mirror.

The sample is held in a variable path length sandwich cell, that can be mounted in a cryostat for computer control. The path length is set to make the sample absorbance less than or equal to 0.3OD to minimize reabsorption fluorescence. Since the absorption and fluorescence spectra of chromophores usually overlap, there is the possibility that a fluorescence photon will be reabsorbed by another chromophore in the sample. While this in itself is not a problem, the newly excited chromophores can emit a fluorescence photon at a time delayed from the original excitation – thereby broadening the effective instrument response. More importantly, the process of reabsorption fluorescence can lead to some depolarization of the emitted fluorescence, which will effect anisotropy measurements. Although the magnitude of this effect depends on Stoke shift and width of absorption and emission spectra, the heuristic of sample optical density $< 0.3OD$ typically ensures no significant contribution. In principle the instrument response of the experiment can be measured from the time dependence of the scattered light from a scattering sample of equal pathlength and optical density. In practice, strong scattering off of defects in the sample glass tend to swamp the scattering from the sample region

itself. This is of little consequence in actual experiments because the excitation light is filtered, but it does prevent a direct measurement of the instrument response. Instead, the time dependence of scattering off a very thin sample (typically a frosted glass microscope slide) is convolved with the response caused by the non-zero pathlength. This is conveniently measured from the scattering peaks off the front and back glass surfaces of the sample cell. In addition, this gives the midpoint of the sample thickness, which can be used to set the condition of $t=0$. While this is not important if the instrument response is deconvolved from the sample response, there is some ambiguity in the assignment if only the longer time ($t>500\text{ps}$) intensity matters, for which deconvolution is unnecessary. In addition to the optical density contribution of the chromophores, the turbidity of the sample must also be kept below a similar limit. This minimizes multiple scattering of the fluorescence before it leaves the sample, which can also lead to depolarization.

Leaving the sample, the fluorescence emission is collected and collimated with a large aperture lens. The fluorescence is then focused through the analyzing Glan-Taylor polarizer onto the entrance slit of a 600 line/mm, single-grating monochromator. The single monochromator is not ideal for ultrafast experiments, as it operates like a grating stretcher adding group velocity dispersion (GVD) and therefore temporally broadening the signal. However, this effect is only calculated to contribute 2ps to the 30ps instrument response. For slower systems including those further described in this work, this is of no consequence. The monochromator provides spectral resolution, both as a way of removing the scattered excitation light, and also as a way of obtaining wavelength information on fluorescence. As an added safeguard against scattered light, which

creates spikes in the data that can be very strong if specularly reflected, a long-pass Schott glass filter is added before the monochromator.

Detection is provided by a bi-alkaline multichannel plate detector. The requirements of TCSPC are very severe regarding detection. Since single photons are being detected, high gain (10^6 to 10^7) is required. In addition, the time characteristics of the detector are central to determining the overall instrument response of the setup. Because constant fraction discrimination is used to receive the electronic pulses from the channel plate, it is not the width of the electronic signal but rather the dispersion in width, known as the transit time spread, that affects time resolution. The transit time spread is the half width of the distribution of arrival times for the many photoelectrons generated by a single detected photon. The conduit for these electrons is small ($10\mu\text{m}$) in a multichannel plate, minimizing transit time spread and leading to its outstanding time performance. The bi-alkaline photosensitive coating is a compromise between extending the sensitivity into the near infrared, and minimizing the thermal electron background. The lower work function required to detect low energy photons causes the increase in thermally excited electrons, which are the dark counts. Fortunately, the intensity distribution of thermal electrons is generally different from that of photo-excited electrons. Luckily, the pulse height distribution for the pulses of interest is higher than that of the thermal background, so that a pulse height discriminator placed before the constant fraction discriminator can remove the majority of dark counts. For the system, the dark count rate is about 80 counts/s, relative to the nominal 40k counts/s at detection.

The detection electronics are at the heart of the TCSPC system. They must detect, discriminate, and bin photon arrivals with picoseconds accuracy at very high rates.

Inputs are the voltage response from the fast Si reference photodiode, and the output of the multichannel plate. The latter is transimpedance amplified to convert the current signal to a voltage without distorting the temporal response. Both inputs are peak height discriminated to remove spurious signals and electrical noise, as well as removing dark counts from the multichannel plate signal. Next the input signals are conditioned using constant fraction discrimination (CFD). This step is crucial to achieving sub-picosecond time resolution, as no photodetectors can create output pulses of comparable width. Furthermore, the CFD removes fluctuations in pulse intensity that would otherwise broaden the time resolution if only peak height discrimination is used. The principle behind CFD is to delay and subtract a lower intensity replica of the signal from itself. For any time-limited signal, this is guaranteed to create a zero crossing at some point subsequent to the peak maximum. This delay is indifferent to pulse height, as both signals are scaled by the intensity fluctuation, and because the triggering event is at zero voltage. The position of this zero crossing is only dependent on the fluctuations in the width of the input, which corresponds to the transit time spread in the detector. While powerful, the CFD approach suffers from sensitivity to electronic noise, most notably ringing caused by impedance mismatch. This ringing has the ability to create spurious zero-crossings, which can prematurely trigger the discriminator in a pattern that replicates the ringing convolved with the fluctuations in the voltage pulse. To remove this artifact, an offset in the voltage level at which the discriminator fires is introduced, and adjusted to be greater than the level of the ringing. This is primarily important on the CFD corresponding to the reference photodiode signal, because the substantial cable delay adds significant impedance, leading to impedance mismatch.

The CDF creates two trigger signals that are sent to a Time Amplitude Converter (TAC), which creates a voltage signal proportional to the time difference between two inputs. The TAC is essentially a capacitor system that is designed to charge at a very stable rate. The start signal initiates the voltage on the capacitor, which begins to store charge and increase in voltage. The stop signal terminates the voltage, which leaves the capacitor charged at a voltage that is proportional to the total time over which the voltage was applied. The charging process is designed as a linear ramp, as opposed to the exponential voltage charging of a capacitor and constant voltage. This process can be made very stable and linear, although a small amount of nonlinearity can distort the signal, especially at longer times. For this reason, different gain and capacitance settings are used for each time window to preserve linearity.

The voltage stored in the capacitor is then digitized in a fast analog to digital converter, and then cleared to ready the circuit for the next laser shot. The ADC process must be both fast (for high count rates) and accurate (to give good time resolution). The speed at which an ADC can be performed is limited by the number of bits, which sets the resolution. To overcome this problem, dithering is used to achieve high accuracy on the ADC while using fewer bits of conversion. The principle is to add a well characterized noise signal to the ADC measurement and oversample the result. With many measurements, it is possible to subtract the noise signal, with the resulting measurement having greater effective bits than the actual number of bits used to perform the ADC. Conceptually, this is similar to the microscopy technique of measuring the point spread function to localize a signal with greater resolution than the diffraction limit. The now digitized voltage is binned and stored in computer memory. The maximum number of

bins, and therefore time resolution at a given range, is determined by the number of effective bits on the ADC, which in this case is 12.

Somewhat counter-intuitively, the TCSPC experiment is run in what is known as delayed Stop-Start mode. This is the mode of choice for signals at high repetition rate. Stop-Start refers to the configuration of detectors as they are routed to the TAC, with a delayed synchronization signal stopping the TAC and the fluorescence detector starting the clock. This is done to minimize the loss to count time. Each time the TAC is initiated by a Start signal, it will run until its predetermined upper limit. Either as a result of reaching the upper limit or receiving a Stop signal, the TAC must be reset – a process that takes about 100ns. If every laser shot triggers the TAC indifferent to whether a fluorescence event was detected or not, then the majority of the fluorescence photons will be lost because the TAC will be blind to them while resetting. By instead only triggering the TAC when a fluorescence photon comes, then the number of lost events will be minimized. At 4MHz excitation and 50ns window, this is not a serious problem because the window plus dead time is less than the repetition rate. However, at longer time intervals, and especially on the older electronics (where the dead time was 1μs), this mode was a necessity. In those cases where the dead time contributes to lost counts, a correction also has to be made to the absolute intensities. This is done by scaling the absolute intensity by the inverse fraction of counting time to total time as²

$$I_{corrected} = I_{measured} * \left(\frac{1}{1 + r_{count} t_{dead}} \right) \quad (3.1)$$

The correction is necessarily a function of counting rate, and rescales the intensity to reflect the total intensity of fluorescence emission. For anisotropy experiments, where

absolute intensities are subtracted, the failure to correct for dead time will create a baseline that may be mistaken for a slow signal.

Another consideration for TCSPC is the count rate. This is usually set at or below 1% of the excitation rate for two related reasons. Assuming the independence of each photon arrival, then the number of detectable photons will follow Poisson statistics. Thus, the ratio of excitations yielding two vs one arriving photon scales as the counting rate. To minimize this for reasons to follow, the counting rate must necessarily be set low. The first has to do with the ability of the discriminator to detect single photons. While the transit time spread in a multichannel plate is small, the actual width of the detected pulse is many nanoseconds. If two photons arrive close together, their sum will yield a broad pulse that is difficult to localize. More importantly, for photons that arrive sufficiently far apart, the dead time of the TAC means that the second photon will not be detected. As only the late photon is discounted, this process creates a bias in the data, shifting the histogram to an earlier time. The magnitude of this effect, known as pile-up, again scales with counting rate. There are two approaches to compensate for pile up. The first is to maintain low counting rates, such that the magnitude of pile-up is able to be neglected. This is the easier approach, and one that is taken for these experiments. But by reducing the counting rate, one is sacrificing counting statistics and therefore signal to noise at a constant counting time. An alternative approach is to run at high counting rates, and then correct for the photon pile up. For a simple histogram such as single exponential lifetime decay, the correction can be analytically derived and applied. In cases with more complex time dynamics, the procedure takes the measured histogram and calculates a time dependent correction to the counts. This is applied, and then iterated using the new

histogram to compute a refined correction. In these experiments, the risk of contamination from pile up on non-trivial waveforms necessitated using lower counting rates.

References

- (1) Lakowicz, J. R. *Principles of Fluorescence Spectroscopy*; 3rd ed.; Springer: New York, 2006.
- (2) Becker, W. *The bh TCSPC Handbook*; 3rd ed.; Becker and Hickl: Berlin, 2008.

Chapter 4: Optical Kerr Effect Studies of Ionic Liquid / Lithium Mixtures

Abstract

Optical heterodyne detected optical Kerr effect experiments were performed on pure 1-butyl-3-methylimidazolium bis(trifluoromethanesulfonyl)imide and on solutions of the ionic liquid containing lithium bis(trifluoromethanesulfonyl)imide. The temperature dependence of the pure ionic liquid spectra was used to test the mode-coupling theory description of the dynamics. The mode-coupling theory fits agreed well with the data, and showed that mode-coupling theory is an accurate descriptor of the system. For the lithium containing solutions, mode-coupling parameters and a related empirical fitting function were used to analyze the data. Many of the trends displayed discontinuous behavior at a lithium salt mole fraction of 0.2.

4.1 Introduction

One application where room temperature ionic liquids are receiving considerable attention is as electrolyte solvents for batteries. The reasons for this interest include the wide electrochemical windows of RTILs¹ and non-flammability. The latter is a serious consideration in Li secondary batteries, where the danger of Li tendrils bridging cathode and anode has resulted in fires in commercial products. Although the assumption of inflammability in ionic liquids has been challenged², they none the less represent a system with significantly reduced hazard. In addition, certain ionic liquids are capable of substantial Li loadings, enhancing carrier density and increasing potential performance –

an important end in advancing Li batteries along the power density axis of the Ragone plot.

Several ionic liquids have been studied for their performance while carrying Li^3 . A common feature in many ionic liquids studies is a drastic reduction in carrier mobilities⁴ as the lithium loading is increased. The dramatic rise in viscosity places severe limits on the achievable currents, which limits the performance attainable from any battery. The source of this effect in the bis(trifluoromethanesulfonyl) $[\text{NTf}_2]^-$ class of ionic liquids, which are promising class of electrolyte ionic liquids for their large Li loadings, has been studied by several means. Two sources of possible influence have been strongly identified as contributing to the loss of carrier mobility. The first is an increase in ion pairing, reducing the number of effective carriers. This harkens to the ideas of ionicity in ionic liquids, and the various deviations of Walden's rule for bulk electrolytes^{5,6}. Specific evidence for this mechanism has been derived from Raman experiments looking at a vibrational mode on the $[\text{NTf}_2]^-$ ion⁷. An increasing vibrational shift with increased Li loading would indicate a perturbation in the local environment closest to the anion. One interpretation of this is a coordinated, direct interaction between the anion and Li which causes the shift. This is not unreasonable, as the positively charged, hard Li cation will energetically favor the anion. But being able to attribute a specific set of interactions and configurations, especially within the broader structure of a concentrated ion solution, is less clear. None the less, MD simulations have suggested specific coordinations between the Li and $[\text{NTf}_2]^-$ that are thought to be responsible⁸.

The second possible mechanism for a loss of carrier mobility is an ionic liquid version of the Chemla effect⁹, which is known in many higher temperature inorganic salts. The

compositional dependence of the viscosity results from geometric effects that propagate over many solvation shells. These extended structures, which are the complex interplay of Madelung energy, ion size, and specific interactions, can greatly increase the viscosity of the medium. Since the carrier mobility depends on the inverse viscosity of the solution, this can also lead to a loss in carrier mobility. In some sense these two effects are very similar – being an interaction between the introduced cation and ionic liquid. What is to be determined is the specificity of the interaction, which would direct the search for anions that could potentially minimize this specific interaction. If the dominant source of mobility loss is non-specific, then tailoring of the ionic liquid in this fashion would be less effective.

As demonstrated by the Raman studies, the local environment of the ions can strongly modify their dynamical properties. Optical heterodyne detected optical Kerr effect spectroscopy (OKE) is one such technique for measuring the orientation and librational relaxation of bulk solutions. The ability to study bulk solutions is very important for studying this problem, as the size of a Li ion interacting with a single anion is much smaller than fluorescence or even EPR probe. The structure would be lost to the perturbation caused by any introduced probe. OKE spectroscopy measures the relaxation of a sample that has been partially aligned by a strong electric field, provided by an ultrafast pulse. Because ultrafast light is used, as opposed to microwave pulses as in NMR, dynamics can be measured from sub-picoseconds to almost arbitrarily slow timescales. The breadth of timescales followed by OKE experiments allows the full hierarchy of correlated dynamics to be examined through a single technique, removing the ambiguities that often result from comparing related experiments.

An OKE experiment is initiated by an ultrafast optical pulse. The strong electric field creates a torque on any anisotropically polarizable molecules in the medium, which orient during the duration of the optical pulse. For very short pulses, the orientation can also involve stimulated Raman modes that fall within the bandwidth of the laser. The oriented sample is allowed to relax field-free for a varied amount of time. Because the sample has been partially oriented, it becomes birefringent. The birefringence is detected by monitoring the polarization rotation of another time-delayed, ultrafast optical pulse. Several features contribute to this signal. After a short time, the predominate contribution comes from the orientational motions of the individual molecules in the form of an orientational correlation function.

Different motions are encapsulated in this orientational correlation function. The organization of the first solvation shell around the rotating molecule creates an effective confinement potential. This correlates the orientation of the molecule with local fluctuations in the surrounding structure, leading to librational motions. These librational motions are dependent on the detailed geometry and interactions comprising the orienting molecule's nearest solvation shell. Moreover, the fact that these solvating molecules themselves are subject to their own confinement propagates the sensitivity outward, sampling a more extensive volume of the solvent. One result of this is a separation of motions into two regimes, those happening within the cage of surrounding solvent, and those motions which evolve as the structure of the cage itself reorients and relaxes. These two apportionments are a common hallmark of liquid structures as probed by OKE.

Although the time dependence of the OKE signal gives the orientational correlation function, additional input is required to connect it to the structural features of interest. One theoretical approach is through mode-coupling theory (MCT). Originally developed to understand density fluctuations in fluids, the model has been expanded to include orientational motions. Within MCT, the relaxation of the perturbation occurs in a harmonic potential with the inclusion of a memory term. The memory term in the time domain is equated with a frequency dependent viscosity in the frequency domain. The theory of MCT is rich with structural models for the functional form of the memory kernel, which generates different dynamical processes such as phase transitions and catastrophes. The schematic model couple theory of Sjorgen¹⁰ is chosen because it has successfully been applied to a variety of liquid systems, including normal liquids¹¹, supercooled liquids¹², and pure ionic liquids¹³. The Sjorgen model uses the F_{12} model to describe the density fluctuations, which expands the memory kernel in powers of the correlation function up to second order. Secondly, it specifies coupling of the density and orientational correlators as a product. Because mode-couple theory is derived for density fluctuations, it requires this connection between the orientational motions and the density fluctuations that they create.

Once the form of the MCT model is specified, the equations of motion are integrated to generate the predicted theoretical curves. These are dependent upon a number of constants that define the magnitude of the various couplings and damping strength. Solutions to the F_{12} model have been shown to correspond to an empirical fitting model, whose benefit is a direct connection to experiment. The functional form of this fitting equation is specified as

$$C(t) = (at^{-s} + pt^{-z} + dt^{b-1}) * e^{\frac{-t}{\tau}} \quad (4.1)$$

The various coefficients correspond to different relaxation processes. The first power law is known as the fast- β processes, which occur on the sub-picosecond timescale. These are small amplitude fluctuations within the tightly confining shell. The second power law is the intermediate power law. It is often times difficult to resolve, as its amplitude is fairly small and occurs on an intermediate timescale between two stronger processes. But in cases with strong separation of timescales, it can be resolved. The third power law is the well known von Schweidler power law from neutron scattering experiments. Although the specific origin of these two latter power laws in terms of molecular motions is not well understood, MCT does predict certain scaling relationships between the parameters as a function of temperature (relative to a phase transition temperature). All three power laws are multiplied by an exponential decay that describes the global re-orientation of the complex network of surrounding molecules. From this form, it is apparent that the three power laws are tied to processes happening within this confinement, which decays as the final exponential in the empirical fitting function.

4.2 Experimental Setup

The laser system used to perform these experiments is previously described. Scans were collected at both phases of the local oscillator, and subtracted to remove the homodyne component. Different pulse energies and pulse durations were used for different decades of time in the experiment. Over the first 20ps, fully compressed ~50fs FWHM optical pulses were used, at a pulse energy of a few hundred nJ/pulse. This affords maximal time resolution for the fast processes. At longer time, collected out to 600ps, the pulses are stretched to 2 ps and 10 μ J/pulse. The longer pulses allow more

energy per pulse while avoiding the threshold of driving other non-linear processes, such as white light generation. The higher pulse energy creates a stronger birefringence, and therefore more signal. To collect data out to 16ns, 200ps pulses are used by bypassing the compressor entirely as the laser leaves the amplifier. While the first two time blocks are performed using a precision stepper motor to afford the appropriate delay, the 16ns delay (corresponding to over 1 meter in double pass) requires a longer delay line driven by a continuous motor. Data is collected continuously, and automatically binned based on a precision position detector. All three data sets are combined using the electronic signal to set $t=0$. The scans are scaled and overlapped, with care taken to ensure the scans can be precisely matched in the overlap region.

Samples were prepared by dissolving an appropriate amount of LiNTf_2 in the ionic liquid 1-butyl-3-methylimidazolium bis(trifluoromethanesulfonyl)imide. The ionic liquid was obtained from Iolitec at maximum purity, 99+%, and further dried under high vacuum and moderate temperature for 1 week prior to use. Water content was quantified using Coulometric Karl-Fischer titration on Mettler-Toledo DL39, and ensured to be less than 50ppm water. The salt-loaded ionic liquids were particle filtered to $0.2\mu\text{m}$, because Mie scattering from dissolved particles is particularly detrimental to the OKE signal. The filtered ionic liquid is sealed in a dust-free glass cuvette which is made air-tight. After data collection, the samples were again measured for water content to ensure sample fidelity. Because the dynamics of ionic liquids are extremely sensitive to small amounts of water, absolute care must be taken to ensure total exclusion of water. Viscosities were measured on a TA Instruments AR-G2 rheometer at different shear rates. All viscosities measured showed Newtonian behavior over the stress rates

accessible by the device. The rheometer was enclosed in a heavily purged nitrogen glovebag to exclude fugitive water.

4.3 Results and Discussion

Figure 4.1 shows combined OKE curves for the pure ionic liquid at different temperatures, vertically offset for clarity. Several features from the empirical fit equation are apparent, including the intermediate power law, von Schweidler power law, and the exponential decay. For higher temperatures, the intermediate power law is difficult to resolve. The fast beta processes are mixed with the instrument response function and stimulated Raman signals. They are not further considered, as they are difficult to resolve and do not show up in the future calculations. From empirical fits to the data, the amplitudes and decay constants for both power laws are determined. Both exponents show no dependence on temperature, as shown in Figure 4.2. This is what is expected from previous work on other systems. The von Schweidler power law is 0.5, which is roughly consistent with the value previously measured in another ionic liquid¹³. Both ionic liquids have exponents which are slightly lower than those normally measured in other molecular systems like supercooled liquids¹². The intermediate power law exponent value of 2.2 is substantially different from anything that has been previously measured. Subsequent to this measurement, other unpublished studies on different cations of the bis(trifluoromethanesulfonyl) family have shown similar coefficients, indicating this is not an experimental artifact. The abnormally large exponent, and therefore much faster dynamics, are not fully understood.

Mode-coupling theory predicts critical phenomena in a liquid as a function of temperature. At sufficiently low temperature, the caging effect from the surrounding

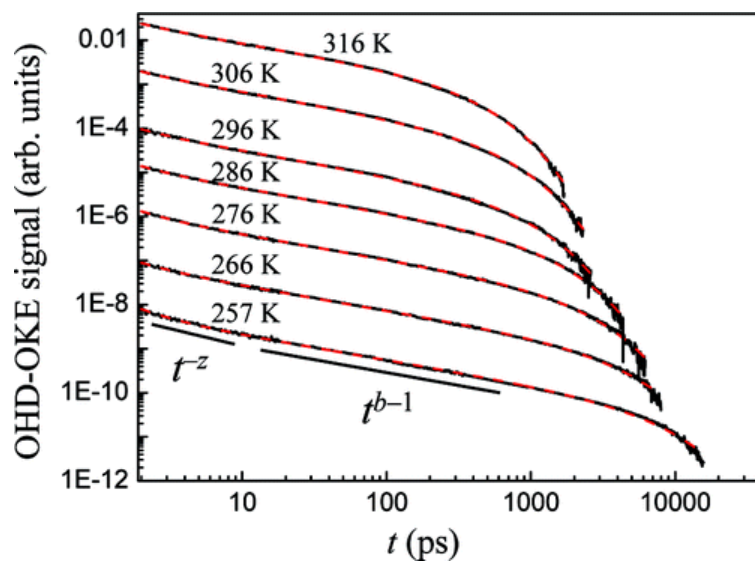


Figure 4.1 Time dependent OKE data and fits for pure Bmim NTf₂. Shown is both the data and fits. For visual clarity, the curves are vertically offset. Highlighted are the different features, including the intermediate power law t^{-z} and von Schweidler power law t^{b-1} .

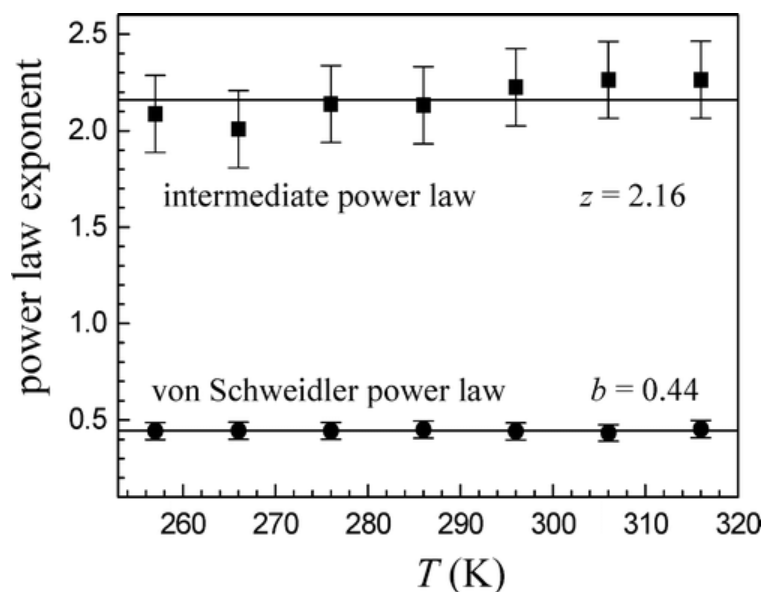


Figure 4.2 The temperature dependence of the power law exponents for the pure ionic liquid.

molecules can become sufficiently strong for a phase transition to occur (associated with the glass transition). This happens as a type A or B catastrophe from the catastrophe theory of Thom¹⁴. The transition is one from an ergodic system to non-ergodic, meaning that dynamically the molecule will no longer be able to sample all off of phase space. Although this picture of the glass transition fails to account for collective modes that allow the system to relax, it captures the essentials of the dynamics in the region near the transition. From the temperature at which this transition occurs, known as T_c or the critical transition, scaling relationships can be derived. These relate the amplitude and exponent of the von Schweidler power law to the global relaxation. The specific scaling relationships are:

$$\begin{aligned}\tau &\propto (T - T_c)^{-\gamma} \\ d &\propto (T - T_c)^\delta\end{aligned}\tag{4.3}$$

T_c is the critical temperature, and the scaling exponents are derived from the exponent of the von Schweidler power law as

$$\begin{aligned}\gamma &= \frac{(a+b)}{2ab} \\ \delta &= \frac{(a+b)}{2a} \\ \frac{\Gamma^2(1-a)}{\Gamma(1-2a)} &= \frac{\Gamma^2(1+b)}{\Gamma(1+2b)}\end{aligned}\tag{4.4}$$

Γ is the incomplete gamma function. The temperature dependence of the exponential relaxation and von Schweidler amplitude can be plotted on a linearizing scale to extrapolate the critical temperature. Figure 4.3 shows these plots. The linearity in both is outstanding, and both extrapolate to the same approximate temperature of 225K. For many of the liquids studied by mode-coupling theory, it is found that the critical

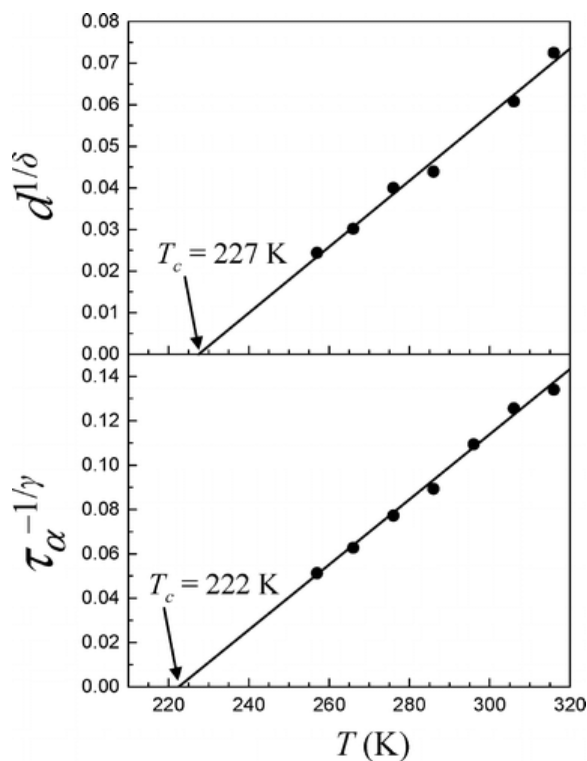


Figure 4.3 Temperature dependent scaling laws predicted by mode-coupling theory. Both show strong linearity, and extrapolate to almost identical critical temperatures.

temperature is greater than the actual glass transition. This owes to the interplay of activated modes that are not treated by MCT. Normally, the MCT T_c is approximately 20% greater than the glass transition temperature T_g . For BmimNTf₂, the glass transition has been measured calorimetrically to occur at 182K¹⁵. Comparing T_g and T_c shows that that ionic liquid obeys this relationship.

Retreating to the full schematic mode coupling theory treatment, solutions are derived from the equations of motion

$$\begin{aligned}
\ddot{\phi}_i &= -\Omega_i^2 \phi_i - \mu \dot{\phi} - \Omega_i^2 \int_0^t m_i(t-\tau) \dot{\phi} d\tau \\
m_1 &= v_1 \phi_1 + v_2 \phi^2 \\
m_2 &= \kappa \phi_1 \phi_2
\end{aligned} \tag{4.5}$$

These equations contain a substantial number of coefficients. Outside the memory kernel, the quantities Ω_i are characteristic oscillation frequencies. They are in the terahertz region, and do not strongly affect the ability to fit the data. μ is a damping constant. Both Ω and μ govern the behavior of fast oscillations which occur and damp at early time. For slower processes, the memory kernel creates the time dependence. The entire F_{12} model is the sum of two correlators, the first being the density and the second being the rotation. Thus, the v coefficients in m_1 describe the strength at which the oscillations are coupled through the memory kernel. κ is the strength of the coupling between the density and rotational correlators. In terms of the glass transition, it is the interplay of these coupling strengths that leads to the glass transition and loss of ergodicity, primarily between v_1 and v_2 .

The temperature dependence of the pair of density couplings defines a trajectory in MCT that leads the system towards the glass transition. The boundary of these points occurs at the theoretical transition to non-ergodic behavior in MCT. Thus, extrapolating the temperature dependent trajectory of coupling constants will provide their values at the critical temperature. From the full treatment of MCT, these values have special meaning in that they are again related to the fitting parameters through scaling relationships. The ergodicity parameter λ is the previously encountered relationship based on the von Schweidler power law

$$\lambda = \frac{\Gamma^2(1+b)}{\Gamma(1+2b)} \quad (4.6)$$

The critical values of the coupling parameters can be established as solutions to

$$\frac{\lambda}{1-\lambda} = \nu_{1c}\lambda + \nu_{2c}\lambda^2 \quad (4.7)$$

From the functional form of these two equations, two crossings are possible. For values of ν_2 less than one, the boundary occurs at a constant ν_1 . This is a type A catastrophe. Outside this region, a downward sloping boundary in the ν_1, ν_2 plane sets the glass transition. Across this boundary is a type B catastrophe. For most liquids, the glass transition occurs at the boundary corresponding to the type B catastrophe. Taking the von Schweidler exponent of 0.4, the critical coupling constants are calculated to be .95 and 1.5. Comparing this to the trajectory in figure 4.4 gives excellent agreement between the prediction and experiment. BmimNTf₂ is shown to be behaving as a typical liquid, with dynamics that are well described by mode-coupling theory.

Having examined the mode-coupling fits to the bulk ionic liquid, the treatment is expanded to find the influence of dissolved Li. The sensitivity of previously mentioned Raman experiments suggest that any change in local structure should affect the librational relaxations, because the two mechanisms share many common features. For the Li loaded ionic liquid samples, the temperature was not varied, but instead singly collected at 295K. As the applicability of mode-coupling theory has already been established in the pure ionic liquid, the collected critical parameters that these extra measurements would generate would not significantly influence the discussion. What is important are the single temperature fit parameters, because these would already contain any signature of a structural change.

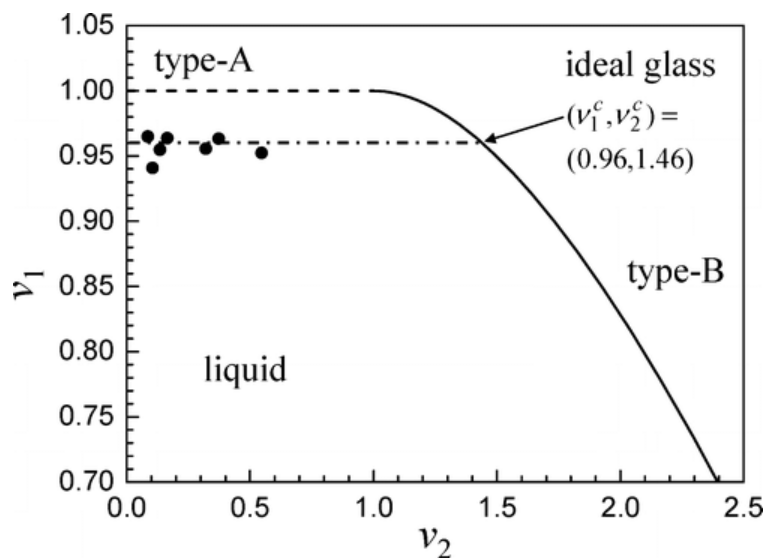


Figure 4.4 The trajectory of the mode-coupling parameters v_1 and v_2 . The boundary shows the point at which the system undergoes a phase transition from liquid to ideal glass. The two boundaries showing the different types of transitions are indicated. The trajectory for the pure ionic liquid crosses at the type B boundary, giving the critical coupling parameters.

Lithium loaded ionic liquids from lithium mole fraction $x = 0$ to 0.4 were prepared and scanned over all timescales. 0.4 is the approximate limit of solubility of the LiNTf_2 salt in BmimNTf_2 . Because both the ionic liquid and Li salt contain the same anion, there is no confluence of interactions between different anions – so that the interactions seen even in the highly loaded solutions should be characteristic of the Li interactions with the pure ionic liquid. As the Li content increases, the viscosity also dramatically increases. Therefore, the changes that result from altered dynamics and those from changes in structure must be separated.

Figure 4.5 gives the exponent for the intermediate and von Schweidler power laws as a function of Li loading. In the case of the pure liquid, these were not temperature

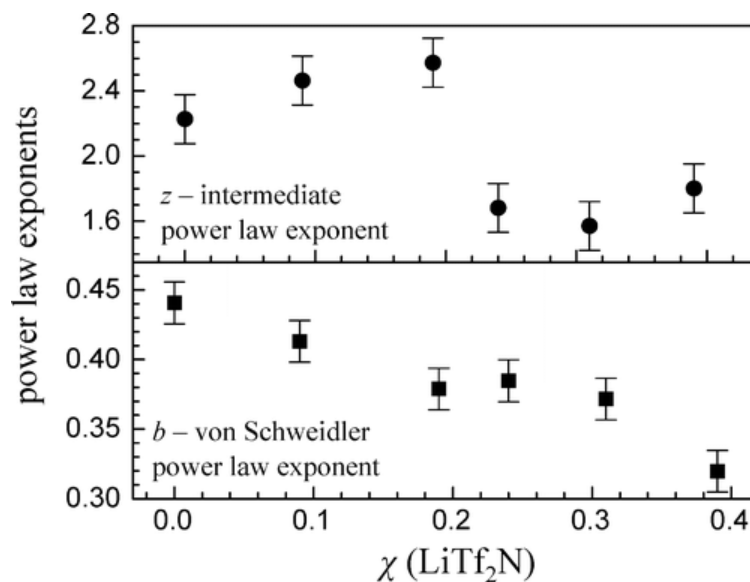


Figure 4.5 Intermediate and von Schweidler power law exponents for the different lithium solutions, expressed as mole fraction Li salt to ionic liquid. The magnitudes are similar, but the trends are different from the temperature dependent values for the pure ionic liquid. Most notable is the discontinuity in the intermediate power law around $\chi=0.2$.

dependent. As the viscosity changes substantially with temperature, this suggests that the parameters are largely sensitive to the structural properties of the cage, which would scale less severely with temperature (density vs. viscosity effects). For the Li loaded salts, there is a statistically significant difference in both exponentials. The von Schweidler power law shows a monotonic, almost linear, decrease in value as Li increases. In terms of structure, the von Schweidler is comprised of the most hindered motions that occur within the solvent cage. The decrease in exponent means these processes slow down with increasing Li loading. Possible causes are stronger geometric frustration through closer packing, or an extension of the cage through interactions which increase the

number of effective partners whose motions are correlated. The intermediate power law shows an interesting behavior. Within error, the power law appears to be bimodal and constant, with different values above and below the mole fraction 0.2. The significance of 0.2 will be later discussed, but the discontinuity could indicate an abrupt structural change.

The final structural re-organization is the alpha relaxation. This relaxation is universally appreciated across a wide range of experiments, including scattering¹⁶ and dielectric spectroscopy¹⁷. The alpha relaxation is the total re-organization of the solvent structure, which relaxes all remaining perturbations to the system. These re-organizations are connected to bulk solution properties (and therefore structure) via the fluctuation-dissipation theorem of linear response. For this reason, a Green-Kubo relationship can be derived which connects the macroscopic viscosity to the orientational diffusion. For diffusion, this leads to the Debye-Stokes-Einstein relation

$$\tau_{\alpha} = \frac{\eta V}{kTC} \quad (4.8)$$

where η is the macroscopic viscosity and kT is the Boltzmann factor. V is the effective hydrodynamic volume of the rotator, and C is a friction term related to the type of boundary conditions. It is shape dependent, and varies from a maximum of 1 to values of .1 or .2 for a typical molecule. For non-spherical particles, the effective volume also includes shape dependent correction factors. The Debye-Stokes-Einstein (DSE) equation is a hydrodynamic result, meaning that surrounding medium is treated as a continuum with only a frequency independent viscosity to retard the orientation. To visualize the DSE equation, the product of orientational diffusion coefficient, which is the inverse of

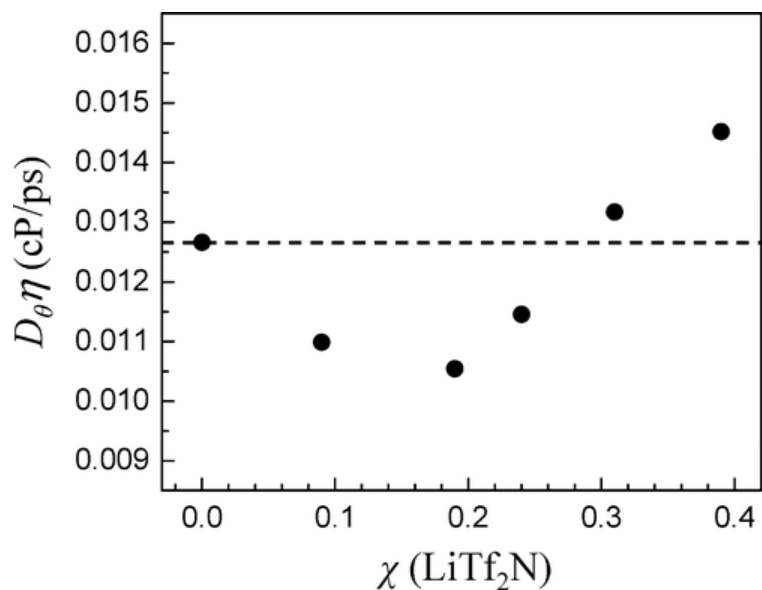


Figure 4.6 The product of orientational diffusion coefficient and viscosity, as a function of lithium mole fraction. The Debye-Stokes-Einstein relation predicts this to be a flat line, which is illustrated relative to the pure ionic liquid. Deviations from Debye-Stokes-Einstein are evident, with a change in behavior again around $\chi=0.2$

$6\tau_r$, is multiplied by the solution viscosity. At a constant temperature, this should also be constant in hydrodynamic theory.

Figure 4.6 shows this result, which is clearly not a constant line. From value at no Li, the product initially decreases. In terms of the parameters in the DSE equation, this represents a slowing down of the orientational diffusion that is greater than predicted by the change in bulk viscosity. Within the DSE equation, the parameters that can accomplish this are contained in the V and C terms. The former can be influenced by strong coordination with other species in solution, which anchor on the rotator and increase the volume of the rotating species. The friction term can also change due to

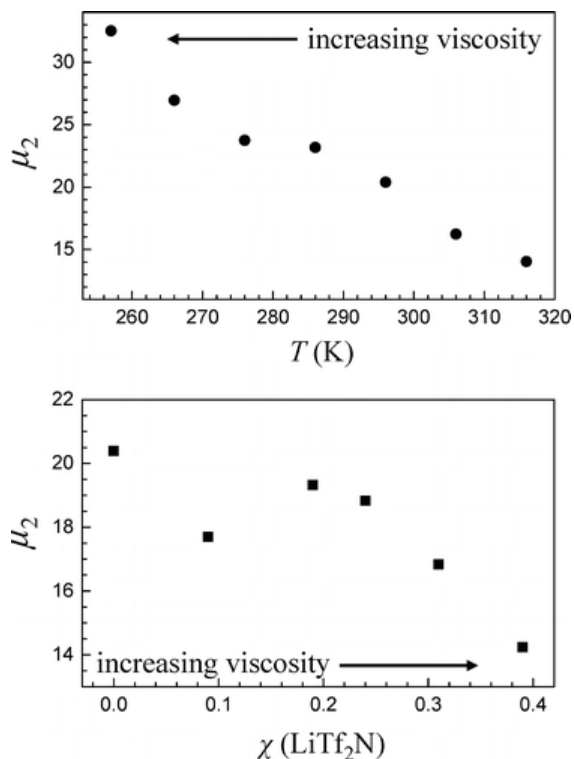


Figure 4.7 The behavior of orientational damping constant, comparing the temperature dependence of the pure ionic liquid to the Li concentration dependence of the salt loaded solutions. The direction of change in viscosity is illustrated to show that the changes are not caused by viscosity. Around $\chi=0.2$ there is potentially a feature, although it may be a consequence of the fitting process.

structural changes and changes in interaction strengths. In the context of low Li rotation, there appears to be some increase in interactions which slows down the rotation. At Li loadings greater than 0.2, the curve ascends and increase above the value measured for the pure solvent. In these situations, the rotation is faster than predicted by viscosity. Again, the change can be due to the previously mentioned factors, but working in the opposite direction. Although no specific interaction can be specified with this analysis, a

more important feature is the transition from slower to faster dynamics at 0.2 mole fraction Li. This is the same Li loading at which the intermediate power law was observed to almost discontinuously change values.

To complement the analysis using the empirical fitting function, single temperature mode coupling theory fits were produced at each Li loading. The abundance of parameters in the models required that each parameter be assessed for its sensitivity and correlation with other parameters. Both characteristic frequencies Ω were found to be relatively insensitive, and so their values were fixed to those used in fitting the pure ionic liquid. Their insensitivity means that fixing them should not affect the fits, although it does also mean no information can be gained from them. Both density coupling constants v_i are calculated from the von Schweidler power law. They show identical trends, except that a decrease in the von Schweidler power law corresponds to an increase in the v_i . This leaves the damping coefficients μ_i and rotational-density coupling κ . For κ , the coupling decreases as viscosity increases, a similar trend to the temperature dependent trajectory in the pure liquid. Similarly, the density damping coefficient constantly trends downward, similar to the case of temperature dependence in the pure liquid. The orientational damping μ_2 shows an altogether different kind of behavior. Plotted in Figure 4.7, there appears to be a feature around Li mole fraction of 0.2. The existence of this feature is difficult to establish with certainty, as the damping coefficient is somewhat correlated with the values of the other coefficients, especially the density damping. While not conclusive, it is evocative again of a change in dynamics in the vicinity of 0.2 Li mole fraction, consistent with the results from the intermediate power law and alpha relaxation.

With three dynamical quantities showing non-monotonic behavior around 0.2 mole fraction Li, it is instructive to question what is special about this composition. The three measurements would indicate that structural changes occur in this region, whose different fundamental nature leads to the different kind of behavior on opposing sides of the transition. Another piece of evidence comes from Raman studies on the anion vibrations⁷. There is a shift in the vibration around 0.2 mole fraction Li, which was interpreted as a structural change. This is consistent with the OKE data. To understand what it is in the structure that changes, MD simulations are required^{8 18}. The results of these simulations show a change in the structure of the ionic liquid brought about by the intrusion of the Li^+ . Initially, the Li^+ incorporates into the charge ordered structure of the ionic liquid by displacing a cation in the solvation of the NTf_2^- . As the Li^+ increases, it reaches a concentration at which its intrusion begins to disrupt the charge ordering of the ionic liquid. As anions crowd around the Li^+ cations, extended structures or clusters are formed. The coordination number for each Li^+ changes from 1 or 2 to more as Li loading proceeds past the 0.2 mole fraction point. While the small Li^+ initially incorporates into the ionic liquid with little perturbation to the structure, their small size and polarizability hardness causes their increased concentration to dominate the interactions with the anions.

From the dynamical measurements, it is clear that a change in the basic features of the ionic liquid solvent occurs in the vicinity of 0.2 mole fraction Li. This supports the results from MD simulations, which indicate clustering of anions around the Li is the source of this structural change, and drives part of the physicochemical changes in the rheology of the mixture. Clearly, the nature of the anion and its interaction with Li^+ will

dominate the system specifics of these changes. The energetics favouring the anion cluster formation are the difference in energy for solvating the small, non-polarizable Li^+ as opposed to the large, polarizable imidazolium cation. It is therefore predicted that larger, more polarizable anions should be less energetically discriminating. Unfortunately, anions of this sort will tend to be more coordinating, which generally causes a salt to crystallize at a higher temperature and rendering it no longer an ionic liquid. Another potential approach would be to combine anions, either as a mixture of ionic liquids or through the anion choice of the Li salt. If the anion coordinating the Li does not couple strongly to the extended ionic structure of the ionic liquid (as is the case when the anion is the same as for the ionic liquid), it may be possible to decouple the clusters from the rheology of the solvent, which would reduce the viscosity increase and mobility decrease. Minimizing the size of the anions would decrease the hydrodynamic volume of the Li-anion clusters, which factors negatively into the ion mobility. The important result from these dynamical measurements is an experimental substantiation of the computational results. This is not inconsequential, as computational results for ionic liquids can vary widely, sometimes arriving at opposing conclusions¹⁹⁻²¹.

4.5 Concluding Remarks

The temperature dependent orientational dynamics of pure 1-butyl-3-methylimidazolium bis(trifluoromethanesulfonyl)imide were measured using optical heterodyne detected optical Kerr effect spectroscopy. The results were accurately fit using an empirical fitting function related to mode coupling theory, as well as with the full mode coupling treatment. Both successfully fit the data, with fits that were consistent with other molecular systems, and with another ionic liquid. Critical values from mode

coupling theory were calculated, and found to be consistent with the supercooled liquid like dynamics that have been measured in other ionic liquids. Room temperature optical Kerr experiments were then performed on 1-butyl-3-methylimidazolium bis(trifluoromethanesulfonyl)imide solutions of lithium bis(trifluoromethanesulfonyl)imide, with lithium salt mole fractions from 0 to 0.4. The resulting dynamics were well fit again by the empirical fitting function and full mode coupling theory. Several of the concentration dependent fitting parameters showed changes in behavior at or around 0.2 mole fraction Li salt. This was compared to MD simulations, which suggest clustering of anions in the ionic liquid around the Li^+ cations. Since optical Kerr spectra are keenly sensitive to the local solvation structure, the experiments support the MD interpretation and its consequences for the physicochemical behavior of lithium loading ionic liquids. The results suggest an understanding of the reasons for the loss of Li mobility in the ionic liquid electrolyte of Li secondary batteries.

4.6 Acknowledgements

This work was a collaboration between several entities. The author gratefully acknowledges Bruno Nicolau and Marcel Ribeiro of University of Sao Paulo, as well as Adam Sturlaugson. The work originated in discussions with Bruno, for which experiments were devised and conducted collectively by Bruno, Adam, and the author. Reproduced with permission from the American Chemical Society.

4.7 References

- (1) Rogers, E. I.; Sljukić, B.; Hardacre, C.; Compton, R. G. *Journal of Chemical & Engineering Data* **2009**, *54*, 2049.
- (2) Fox, D. M.; Gilman, J. W.; Morgan, A. B.; Shields, J. R.; Maupin, P. H.; Lyon, R. E.; De Long, H. C.; Trulove, P. C. *Industrial & Engineering Chemistry Research* **2008**, *47*, 6327.
- (3) Moosbauer, D.; Zugmann, S.; Amereller, M.; Gores, H. J. *Journal of Chemical & Engineering Data* **2010**, *55*, 1794.
- (4) Umecky, T.; Saito, Y.; Okumura, Y.; Maeda, S.; Sakai, T. *J. Phys. Chem. B.* **2008**, *112*, 3357.
- (5) Schreiner, C.; Zugmann, S.; Hartl, R.; Gores, H. J. *Journal of Chemical & Engineering Data* **2010**, *55*, 4372.
- (6) MacFarlane, D. R.; Forsyth, M.; Izgorodina, E. I.; Abbott, A. P.; Annat, G.; Fraser, K. *Phys. Chem. Chem. Phys.* **2009**, *11*, 4962.
- (7) Umebayashi, Y.; Mitsugi, T.; Fukuda, S.; Fujimori, T.; Fujii, K.; Kanzaki, R.; Takeuchi, M.; Ishiguro, S.-I. *J. Phys. Chem. B.* **2007**, *111*, 13028.
- (8) Borodin, O.; Smith, G. D.; Henderson, W. *J. Phys. Chem. B.* **2006**, *110*, 16879.
- (9) Ribeiro, M. C. C. *J. Phys. Chem. B.* **2003**, *107*, 4392.
- (10) Ouml; tze, W.; Sperl, M. *Physical Review Letters* **2004**, *92*, 105701.
- (11) Greenfield, S. R.; Sengupta, A.; Stankus, J. J.; Terazima, M.; Fayer, M. D. *J. Phys. Chem.* **1994**, *98*, 313.

- (12) Brace, D. D.; Gottke, S. D.; Cang, H.; Fayer, M. D. *J. Chem. Phys.* **2002**, *116*, 1598.
- (13) Li, J.; Wang, I.; Fruchey, K.; Fayer, M. D. *J. Phys. Chem. A* **2006**, *110*, 10384.
- (14) Saunders, P. *An Introduction to Catastrophe Theory*; University Press: Cambridge, England, 1980.
- (15) Blokhin, A. V.; Paulechka, Y. U.; Strechan, A. A.; Kabo, G. J. *J. Phys. Chem. B.* **2008**, *112*, 4357.
- (16) Gotze, W.; Sjogren, L. *Reports on Progress in Physics* **1992**, *55*, 241.
- (17) Lunkenheimer, P.; Pardo, L. C.; Ouml; hler, M.; Loidl, A. *Phys. Rev. E* **2008**, *77*, 031506.
- (18) Monteiro, M. J.; Bazito, F. F. C.; Siqueira, L. J. A.; Ribeiro, M. C. C.; Torresi, R. M. *J. Phys. Chem. B.* **2008**, *112*, 2102.
- (19) Gutel, T.; Santini, C. C.; Pádua, A. I. A. H.; Fenet, B.; Chauvin, Y.; Canongia Lopes, J. N.; Bayard, F. o.; Costa Gomes, M. F.; Pensado, A. S. *J. Phys. Chem. B.* **2008**, *113*, 170.
- (20) Chaumont, A.; Wipff, G. *Journal of Molecular Liquids* **2007**, *131*, 36.
- (21) Padua, A. A. H.; Gomes, M. F.; Lopes, J. N. A. C. *Acc. Chem. Res.* **2007**, *40*, 1087.

Chapter 5: Dynamics in Organic Ionic Liquids in Distinct Regions Using Charged and Uncharged Orientational Relaxation Probes

Abstract

The temperature-dependent fluorescence anisotropy decay (orientational relaxation) of perylene and sodium 8-methoxypyrene-1,3,6-sulfonate (MPTS) were measured in a series of 1-alkyl-3-methylimidazolium bis(trifluoromethanesulfonyl)imide (alkyl = ethyl, butyl, hexyl, octyl) organic room temperature ionic liquids (RTIL). The two fluorescent probe molecules display markedly different rotational dynamics when analyzed using Stokes-Einstein-Debye theory demonstrating that they are located in distinct environments within the RTILs and have very different interactions with their surroundings. Perylene rotates with sub-slip behavior, becoming increasingly sub-slip as the length of ionic liquid alkyl chain is increased. The dynamics approach those of perylene in an organic oil. In contrast, MPTS shows super-stick behavior, likely reflecting very strong coordination with the RTIL cations. These results are consistent with different elements of rotational friction within the ionic liquid structure, which are available to solutes depending on their chemical functionality.

5.1 Introduction

As experimental studies on organic room temperature ionic liquids (RTIL) converge on a cogent picture of liquid structure and dynamics, important questions remain regarding the influence of local chemical environments on solute molecules. The

interaction of an ionic liquid solvent with dissolved solute is of particular importance to many of the proposed applications such as reaction solvents,¹⁻³ separations,⁴ and batteries⁵. These issues have strong dynamical underpinnings that time dependent studies can address.

A particularly important and distinguishing characteristic of organic ionic liquids is the concept of nanoscale heterogeneity. Originally identified in MD simulations⁶, the concept has gained considerable traction as a diverse range of experimental studies appear to confirm the existence of structures that persist on non-negligible time scales.⁷⁻¹¹ These proposed ionic liquid structures contain hydrophobic regions of alkyl “tails,” and charge-ordered, hydrophilic “head group” regions. In the context of this liquid structure, strong elements of selective solvation are possible. The resulting diversity of local environments can have a direct impact on the dynamics of processes where solvation environment is important. The effect of environment has been observed in the context of a photoisomerization.¹² It is not difficult to consider the importance of dynamic heterogeneity being expanded beyond selective excitation in photochemical reactions to include differences in transport properties and availability of reagents and catalysts in the ionic liquid matrix.

One appeal of RTILs as a reaction medium is the breadth of molecules they can solvate. It is not unreasonable to ascribe this to the presence of multiple chemical environments. Dynamic heterogeneity may have a non-trivial impact on the reaction dynamics, and therefore influence “task-specific” organic ionic liquids.¹³ The design of task-specific organic ionic liquids may depend on the dynamics of molecules in distinct environments in addition to the specific substrate interactions.

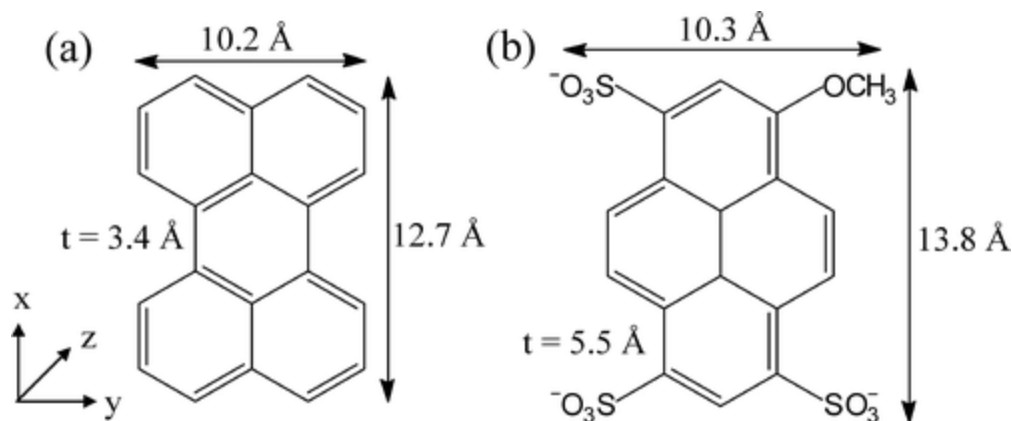


Figure 5.1 The structures, dimensions, and coordinate systems used for (a) Perylene and (b) MPTS.

In this study, the orientational relaxation dynamics of perylene and sodium 8-methoxypyrene-1,3,6-sulfonate (MPTS) were determined using time dependent fluorescence anisotropy measurements. Perylene and MPTS reflect two extremes of chemical functionalities (see Figure 5.1). Perylene is neutral and nonpolar. In contrast, MPTS has three negatively charge sulfonate groups. These two probe molecules will likely interact with the separate elements of the charged and nonpolar environments in the ionic liquid structure. The series of ionic liquids of alkyl-substituted imidazolium bis(trifluoromethanesulfonyl)imide (abbreviated as $\text{C}_n\text{mim}^+ \text{NTf}_2^-$) was chosen as a class of relatively hydrophobic ionic liquids that can be obtained at high purities. They have fairly low viscosities and should demonstrate prototypical ionic liquid behavior. Furthermore, for imidazolium cations, there have been indications that a minimum chain length is required for formation of nanostructure environments.⁶

For each liquid, the orientational relaxation and the viscosity were measured as a function of temperature. These measurement permit the details of the probe interactions

with its environment to be explicated. The results demonstrate that perylene and MPTS are located in distinct environments and experience very different interactions with their surroundings. Perylene rotates with sub-slip behavior, becoming increasingly sub-slip as the length of RTIL alkyl chain is increased. In contrast, MPTS shows super-stick behavior, likely reflecting very strong coordination with the RTIL cations. These results are consistent with different elements of rotational friction within the ionic liquid local structures that are available to solutes depending on their chemical functionality.

Previous fluorescence studies of orientational relaxation of RTILs have seen Debye-Stokes-Einstein (DSE) behavior¹⁴ and possibly deviations from DSE behavior.¹⁵⁻¹⁷ Most of the studies examined very polar and charged dye molecules. Mali, et al. studied a charged dye molecule and a non-polar chromophore in a single RTIL.¹⁵ The studies presented here examine a triply charged fluorophore and a neutral non-polar fluorophore that are similar in size (see Figure 1) in a series of RTILs with increasing hydrocarbon chain lengths. The temperature dependent studies of the orientational relaxation permit the local friction to be extracted from the data. By measuring the orientational relaxation on the series of liquids, it is possible to examine changes in the nature of the local environments experience by the two types of probe molecules.

5.2 Experimental Setup

All ionic liquids were purchased from IoLiTec at 99+% HP grade. The fluorophores were purchased from Aldrich, and used without further purification. HPLC grade water (Fisher) and DMSO (Mallinckrodt AR Grade) were distilled prior to use. Light paraffin oil (Fisher) was used without modification. The ionic liquids were dried upon receipt under vacuum at 60°C for 1 day, and then transferred into a nitrogen glove box for

storage and sample preparation. Water content was measured for all ionic liquid samples using Karl-Fisher titration (Mettler DL39) and is less than 75 ppm water by weight. The optical samples were prepared from stock solutions by dissolving the chromophore at a standardized concentration in a volatile solvent (hexane for perylene and methanol for MPTS). A 1-cm quartz cuvette was filled with an appropriate amount of stock solution and then the solvent evaporated under gentle heat and dry nitrogen. These were transferred into the glove box and stirred with aliquots of the ionic liquid to a 0.3 optical density, corresponding to a chromophore concentration of approximately 8×10^{-6} M for both dyes. One consequence of note resulting from the sample preparation technique is the absence of dissolved O₂ in any of the ionic liquid samples. Non-ionic liquid solvents were purged with nitrogen to remove O₂, but the fluorophores showed slightly shorter lifetimes owing to the incomplete removal of oxygen.

The measurements were made with time correlated single photon counting (TCSPC), and the experimental setup is described elsewhere¹⁸. The samples were housed in a computer controlled cryostat (Janis ST-100) stable to ± 0.1 K. The instrument response was measured to be 40 ps using a scattering sample. Time dependent fluorescence data were collected at each temperature (298 K to 333 K in 5 K increments) in parallel, perpendicular, and magic angle (54.7°) polarizer orientations. Samples were excited at 380 nm for MPTS and 409 nm for perylene. The excitation pulses were single pulses selected at 4 MHz rate from a Ti:Sapphire oscillator and doubled to the excitation wavelengths. Fluorescence, after passing through an appropriate long pass filter to remove excitation light, was observed at 420 nm for MPTS and 469 nm for perylene with a channel plate detector on a monochromator.

Steady-state fluorescence spectra were collected at room temperature using a Fluorolog-3 fluorimeter. Fluorescence spectra were collected in the forward-facing geometry with excitation at 380 nm with correction for lamp fluctuation and monochromator/detector efficiency. Temperature dependent viscosities of paraffin oil were measured using a Cannon-Ubbelohde viscometer in a constant temperature bath. Other viscosities were taken from the literature.¹⁹ Since RTIL viscosity can be dramatically affected by small impurity concentrations, the room temperature viscosities were confirmed in a nitrogen purged environment using a Texas Instruments AR-G2 rheometer with 40-mm parallel plate geometry.

5.3 Results and Discussion

The fluorescence experiments measure the time dependent anisotropy, $r(t)$, defined as

$$r(t) = \frac{I_{\parallel}(t) - I_{\perp}(t)}{I_{\parallel}(t) + 2I_{\perp}(t)}, \quad (5.1)$$

with I_{\parallel} and I_{\perp} the time dependent fluorescence intensities polarized parallel and perpendicular to the excitation beam, respectively. Eisinger and Chaung presented the functional form of the fluorescence anisotropy decay for the most general case of orientational diffusion.²⁰ The result is a sum of 5 exponentially decaying terms containing rotational diffusion constants D_j about the j th molecular axis as:

$$r(t) = \frac{6}{5}(q_y q_z \gamma_y \gamma_z e^{-3(D_x + D)t} + q_x q_z \gamma_x \gamma_z e^{-3(D_y + D)t} + q_x q_y \gamma_x \gamma_y e^{-3(D_z + D)t}) + \frac{3}{10}(\beta + \alpha)e^{-(6D + 2\Delta)} + \frac{3}{10}(\beta - \alpha)e^{-(6D - 2\Delta)} \quad (5.2)$$

for

$$\alpha = \frac{1}{\Delta} [D_x (q_y^2 \gamma_y^2 + q_z^2 \gamma_z^2 - 2q_x^2 \gamma_x^2 + q_x^2 + \gamma_x^2) + D_y (q_x^2 \gamma_x^2 + q_z^2 \gamma_z^2 - 2q_y^2 \gamma_y^2 + q_y^2 + \gamma_y^2) + D_z (q_x^2 \gamma_x^2 + q_y^2 \gamma_y^2 - 2q_z^2 \gamma_z^2 + q_z^2 + \gamma_z^2) - 2D]$$

$$\beta = q_x^2 \gamma_x^2 + q_y^2 \gamma_y^2 + q_z^2 \gamma_z^2 - \frac{1}{3}$$

$$D = \frac{1}{3} (D_x + D_y + D_z)$$

$$\Delta = \sqrt{(D_x^2 + D_y^2 + D_z^2 - D_x D_y - D_x D_z - D_y D_z)}$$

The quantities q_j and γ_j are projections of the excitation and emission dipole onto the molecular axes. For most rotators, the similarity of the rotational diffusion constants generally causes there to be fewer than 5 resolvable exponentials, often times generating only a single rotational diffusion constant.

In the experiments presented here, the observed exponential decays were related to hydrodynamic properties through the Debye-Stokes-Einstein relation:

$$\tau = \frac{1}{6D} = \frac{\eta V f C}{kT} \quad (5.3)$$

where τ is the measured orientational relaxation time constant, η the viscosity, k is the Boltzmann constant, V is the molecular volume, C is a friction coefficient, and f is the shape factor. For a given molecule, the friction coefficient will contain information on the rotational friction experienced by the molecule. For large particles, the stick boundary condition ($C = 1$) almost always holds. For rotators of similar size to the solvent molecules, the continuum approximation of the solvent begins to break down. This is manifest as a decrease in friction toward the slip limit, for which the value of C depends on the geometry of the rotator.

Figure 5.1 shows the structures and dimensions of the fluorophores used in this study. For both molecules, the shape is close to ellipsoidal based on a geometrically

Shape Factors					Slip Coefficients			
	f_x	f_y	f_z	f	C_x	C_y	C_z	C
Perylene	1.86	1.38	2.03	1.76	0.23	0.65	0.015	0.085
MPTS	1.43	1.01	1.55	1.33	0.10	0.54	0.032	0.110

Table 5.1 Shape factors and slip coefficients for the two dye molecules.

minimized structure. Using the van der Waal radii of the constituent atoms, molecular volumes of 225 Å³ for perylene and 343 Å³ MPTS were calculated. From the molecular dimensions, the shape factors²¹ and theoretical slip friction coefficients^{22,23} can also be generated. These quantities are listed in Table 1.

5.3.1 Perylene

Due to the high D_{2h} symmetry of perylene, the equation for the fluorescence anisotropy simplifies to

$$r(t) = 0.3(\alpha - \beta)e^{-(6D+2\Delta)t} + 0.3(\alpha + \beta)e^{-(6D-2\Delta)t} . \quad (5.4)$$

Equation 4 can be further simplified if one assumes the behavior of an oblate spheroid rotator, that is $D_x = D_y \ll D_z$, using the coordinate system of Figure 1. Under these conditions, equation 4 can be expressed as

$$r(t) = 0.1e^{-(2D_x+4D_z)t} + 0.3e^{-6D_x t} \quad (5.5)$$

Anisotropy studies of perylene have often encountered a well-known “anisotropy deficit,” that is, an initial anisotropy of less than the theoretical 0.4.²⁴ While this does not directly impact the information content of the experiment, the prefactors in equation 5.5 have smaller than the theoretical values of 0.1 and 0.3.

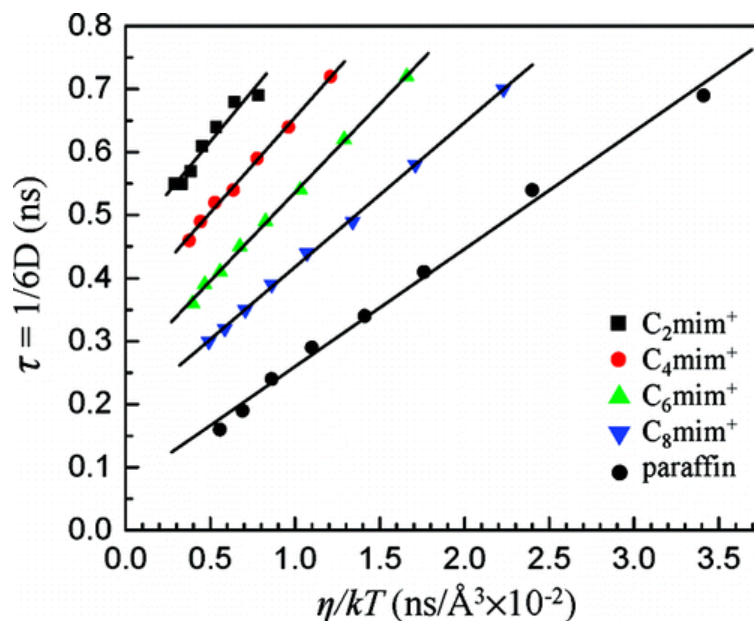


Figure 5.2 Debye-Stokes-Einstein plots for the different ionic liquids. The lines are linear least square regression. For visual clarity, the curves have been shifted upward by 0.4 ns for C_2mim^+ , 0.3 ns for C_4mim^+ , 0.2 ns for C_6mim^+ , and 0.1 ns for C_8mim^+

To extract the rotational diffusion constants, measured time dependent anisotropies were fit to a biexponential function convolved with the instrument response using nonlinear least squares. From the fits, the appropriate diffusion constants can be extracted from linear combinations of the exponential time constants using equation 4. Figure 5.2 shows the temperature dependent orientational relaxation decay constant, $\tau = 1/6D$, where here D is the average diffusion constant. In all cases except C_2mim^+ ($r^2 = 0.95$), linear regression yields an adjusted correlation coefficient of greater than 0.99, which confirms Debye-Stokes-Einstein behavior.

The results of the analysis are presented in Table 5.2 as a list of the experimentally determined average friction coefficients (C in equation 5.3). As the alkyl chain length increases, the friction coefficient approaches that of perylene in paraffin oil. From the

Solvent	Friction Coefficient
C ₂ mim ⁺	0.0858 ± 0.008
C ₄ mim ⁺	0.0799 ± 0.002
C ₆ mim ⁺	0.0733 ± 0.001
C ₈ mim ⁺	0.0583 ± 0.0007
paraffin oil	0.0483 ± 0.001
Theory Slip	0.085

Table 5.2 Rotational friction coefficients C for perylene in the different solvents.

values listed in Table 2, perylene is found to rotate with slip to sub-slip boundary conditions.

Because perylene is only slightly larger than the ionic liquid ions, some contribution to the sub-slip behavior can come from the coarseness of solvent media, which can be treated using Gierer-Wirtz theory. The Gierer-Wirtz theory takes the solvent to be concentric shells of spherical particles around the probe solute. For a solvent volume V_s smaller than probe solute volume V_p , the theory expresses the friction coefficient as:

$$C = \sigma C_0$$

$$\sigma = \frac{1}{1 + 6(V_s/V_p)^{1/3}} C_0 \quad (5.6)$$

$$C_0 = \left[\frac{6(V_s/V_p)^{1/3}}{\left(1 + 3(V_s/V_p)^{1/3}\right)^4} + \frac{1}{\left(1 + 4(V_s/V_p)^{1/3}\right)^3} \right]^{-1}$$

A volume of 163 Å³ was used for V_s , which is approximately the value for both the C₄mim⁺ and NTf₂⁻ ions. Using equation 6, a value of $C = 0.18$ for perylene is computed. Because the calculated value is a factor of 2 greater than the measured friction coefficient, and since no reasonable value for V_s can replicate the measurements, the

	in-plane	out of plane
C ₂ mim ⁺	1.2	0.39
C ₄ mim ⁺	1.0	0.44
C ₆ mim ⁺	0.90	0.53
C ₈ mim ⁺	0.67	0.54
paraffin oil	0.55	0.60

Table 5.3 Ratios of the in-plane and out-of-plane rotational constants relative to their slip values.

treatment that only considers the sizes of the solvent and solute molecules cannot explain the sub-slip rotational dynamics of perylene in the RTILs.

Rotational dynamics in the sub-slip regime have been studied previously^{25,26} and are often attributed to complex solvation structure in the vicinity of the probe molecule. This structuring can lead to effective void spaces through which the molecule can rotate with little hindrance, leading to a decrease in rotational friction below slip. This picture is used to describe the rotational dynamics of tetracene in alcohols.²⁷

In the perylene/RTIL experiments, the degree of sub-slip increases with increasing alkyl tail length, approaching the value for perylene in paraffin oil at C₈mim⁺. Due to the high symmetry of perylene, the bi-exponential experimental decays permit the rotational diffusion to be further decomposed into components of rotation in-plane (D_z) and out-of-plane (D_x). The results are presented in Table 3 as the ratio of the appropriate friction coefficient to its theoretical value for slip boundary conditions. A value of 1 means that the measured and calculated values are the same. A ratio larger than 1 indicates that the measured value is slower than slip, and a ratio smaller than 1 shows that the experimental value is faster than slip. The trends displayed in Table 5.3 demonstrate that as the length

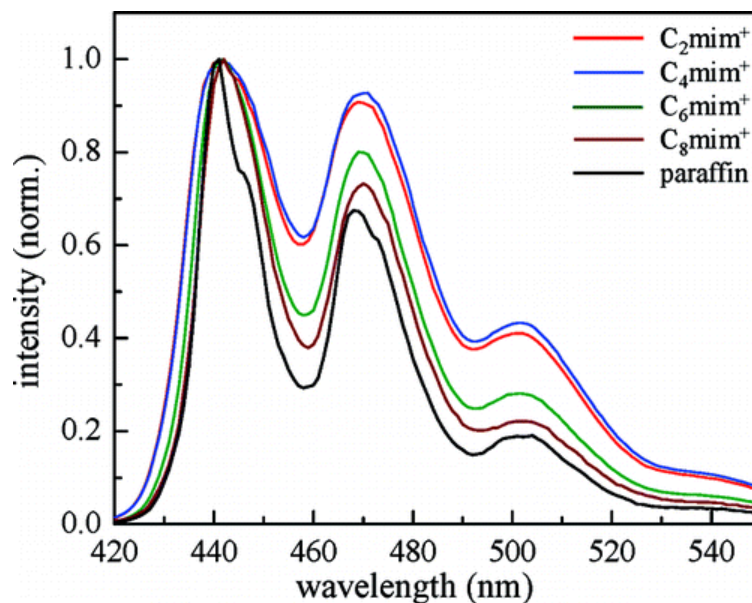


Figure 5.3 Normalized, steady-state fluorescence intensity spectra for perylene in the different solvents.

of the ionic liquid alkyl chain length increases, relative to the theoretical slip values, the in plane rotational diffusion becomes faster with a concurrent slower rotational diffusion out of plane. Both the in-plane and out of plane rotational diffusion are converging on the values found in the paraffin oil. The increase of in-plane rotational diffusion constant with alkyl chain length is consistent with previous work on perylene in n-alkanes. For longer alkanes, the results are interpreted as a partial alignment of the alkane chains along the long axis of the perylene^{28,29}. This interpretation is supported by studies of gas phase van der Waal complexes³⁰. Therefore, the orientational relaxation trends with RTIL chain length indicate that the environment experienced by perylene is increasingly like that of a partially ordered alkane.

The convergence of the perylene environment to that of an alkane as the RTIL alkyl chain length increases is also manifest in the perylene fluorescence spectra displayed in

Figure 5.3. The spectra are normalized at their peaks for clarity. As the RTIL chain length increases, the spectra become closer to that of perylene in the paraffin oil. The spectra are in accord with the trends seen in the friction coefficient data given in Table 5.3. The fluorescence spectra are sensitive to the local solvent environment and the orientational relaxation data depend on how the environment influences the dynamic interactions between the non-polar perylene fluorophore and its environment. Both types of data show that as the chain length increases, perylene finds its environment approaching that of a hydrocarbon liquid.

These convergent trends of perylene demonstrate that the solvation environment of perylene in the ionic liquids becomes more alkane-like as the alkyl chain increases in length. In the context of ionic liquid structure, one might conclude that the aliphatic moiety is dominant in solvating the perylene. This is consistent with simulations on solvation in ionic liquids^{31,32}, as well as a recent optical Kerr effect experiment³³. The selective solvation constitutes an effective partitioning of the perylene into the hydrophobic regions of the bulk ionic liquid structure. The sub-slip rotational behavior is describing the structure and microviscosity of the hydrophobic pockets. It is important to note the apparent lack of a “turn-on” of nanoscale segregation. Both the in plane and out of plane friction coefficients change continuously toward those of perylene in paraffin oil.

This interpretation leads to several interesting possibilities. Although not necessarily of the same origin, void spaces in RTILs have been evoked when discussing the solubility of CO₂.³⁴ The directionality of the rotational friction (see Table 5.3) may provide insight into anomalous Diels-Alder reactions in RTILs.³⁵ Tiwari and coworkers

find that the rate of an intra-molecular Diels-Alder reaction involving a nonpolar reactant does not change significantly in going from $C_4mim^+ NTf_2^-$ to $C_4mim^+ [BF_4^-]$, even though the viscosity changes substantially. The reaction involves the rotation of the dienophile over the plane of the molecule. This is the direction of rotation in C_4mim^+ that is most strongly sub-slip, indicating a relatively unhindered rotation produced by the ionic liquid structure that should be relatively insensitive to the anion.

5.3.2 MPTS

The anisotropy decays of MPTS in all liquids are single exponential, reflecting the lower symmetry of MPTS compared to perylene and indicating similar MPTS rotational diffusion

coefficients for the various axes. The decay times vs. η/kT are shown in Figure 4 for three RTILs, DMSO, and water. MPTS is essentially insoluble in C_8mim^+ , so this liquid could not be studied. Because of the low viscosity, the data for MPTS in DMSO and water have very fast decay times. The data for these two liquids are shown in the inset. As is the case for perylene, the MPTS temperature dependent data in each liquid is linear within a very small error, demonstrating Debye-Stokes-Einstein behavior.

The friction coefficients for the five liquids are given in Table 5.4. The friction coefficient for stick boundary conditions is 1. In contrast to the perylene (see Table 5.2), the MPTS friction coefficients are all greater than 1 for the ionic liquid samples (Table 5.4), indicating super-stick boundary conditions. MPTS in water and DMSO were used as control solvents for comparison. MPTS in these two solvents yield close to stick boundary conditions. Super-stick conditions observed in the RTILs are traditionally

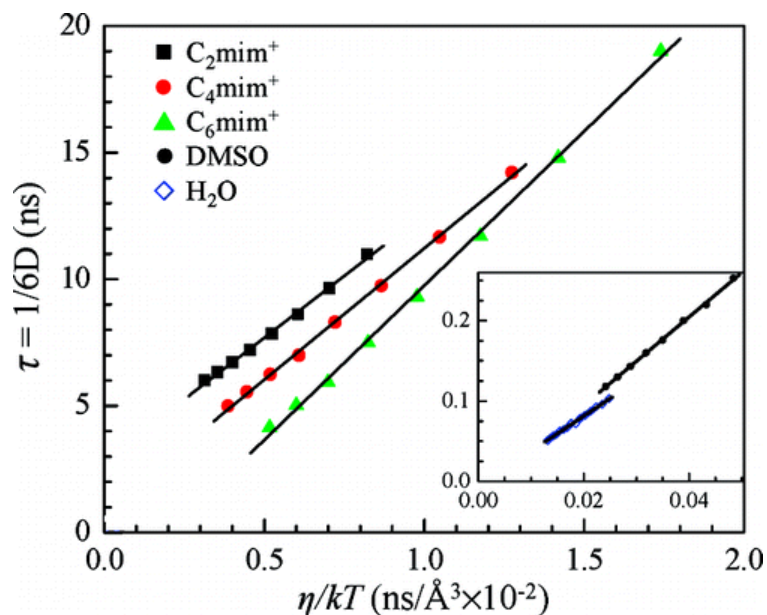


Figure 5.4 Debye-Stokes-Einstein plot for MPTS in different solvents. For clarity, the plots for C_2mim^+ and C_4mim^+ have been vertically displaced 4 and 2 ns, respectively. The inset shows a close-up view of the DMSO and water, which are not easily seen on the full scale. The lines through the data are linear least square regressions.

Solvent	Friction Coefficient
C_2mim^+	2.22 ± 0.05
C_4mim^+	2.36 ± 0.03
C_6mim^+	2.77 ± 0.04
Water	0.99 ± 0.02
DMSO	1.25 ± 0.01

Table 5.4 Rotational friction coefficients for MPTS in the different solvents

explained using either the “solventberg” model³⁶ or Nee-Zwanzig dielectric friction³⁷ (equation 5.7). The former assumes specific solvent-solute interactions anchor solvent molecules of non-negligible size to the solute, effectively increasing the rotator volume.

The latter involves the electrostatic torque between a dipole and the reactive field of the surrounding dielectric cavity, as

$$D = \frac{kT}{6\eta V f C + \zeta_{NZ}} \quad (5.7)$$

$$\zeta_{NZ} = \frac{2\mu^2}{a^3} \frac{(\epsilon_\infty + 2)^2 (\epsilon_0 - \epsilon_\infty)}{3(2\epsilon_0 + \epsilon_\infty)} \tau_D$$

where μ is the dipole moment of the solute, a is the dielectric cavity radius, τ_D is the Debye relaxation time, and ϵ_0 and ϵ_∞ are the static and optical dielectric constants, respectively.

Given the structure of MPTS, both mechanisms are expected to contribute in the ionic liquid samples. The 3 formal -1 charged sulfonate groups should interact very strongly with the charged cations of the ionic liquid. Similarly, the presence of a reasonably strong dipole and long Debye relaxation time could also contribute to a dielectric friction. For alcohol solvents that can hydrogen bond to the solute research on the relative contributions of the two mechanisms has indicated that the “solventberg” effect dominates.³⁸

For the RTILs studied here, the contribution from the dielectric friction was estimated using equation 7 with aggressive but not unrealistic physical parameters and measured properties of the ionic liquids. Taking $\mu = 15$ D,³⁹ $a = 6$ Å³⁹ $\tau_D = 500$ ps,⁴⁰ $\epsilon_0 = 10$,⁴¹ and $n^2 = \epsilon_\infty = 1.4$,⁴⁰ one arrives at an additional contribution to the friction that is <0.8 . This contribution is in addition to the value of 1, which is the mechanical friction for stick boundary conditions. The actual contribution will most likely be significantly smaller because the RTIL solvents are charged resulting in a reduction caused by the kinetic polarization deficiency and shielding.⁴² With rotational frictions that exceeds stick

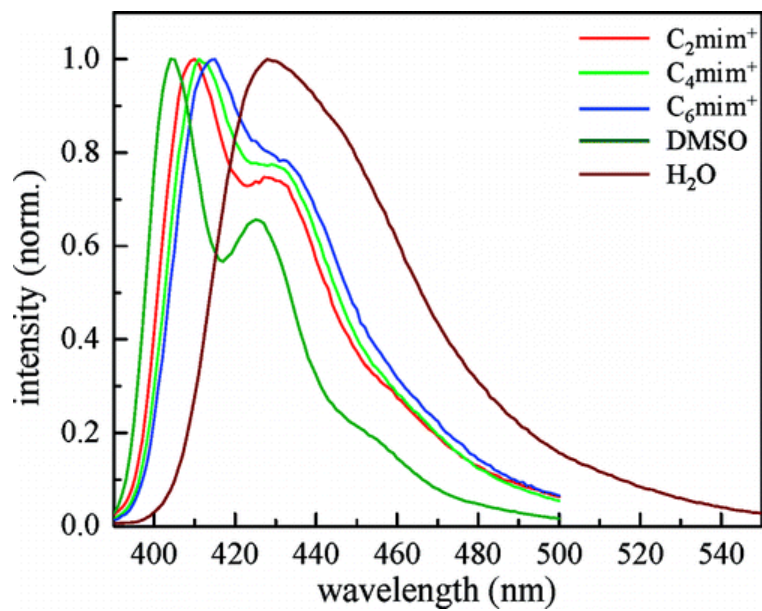


Figure 5.5 Normalized, steady-state fluorescence intensity spectra for MPTS in different solvents.

boundary conditions by greater than a factor of 2 (see Table 5.4), the dielectric friction alone cannot account for the observed super-stick results.

Figure 5.5 shows the fluorescence spectra of MPTS in the three RTILs and in DMSO and water. MPTS in the three RTILs shows a significant shift to longer wave lengths and a reduction of vibronic structure relative to DMSO. The loss of vibronic structure and bathochromic shift of the fluorescence is indicative of strong solvent-solute interactions.⁴³ The shift and reduction of vibronic structure increases as the alkyl chain length of the RTIL increases. This trend may indicate stronger solute-solvent interactions because of increased segregation of the liquid into ionic regions and alkane-like regions, which is in accord with the trends seen for perylene. The shift in the MPTS spectrum and reduction in vibronic structure with increasing RTIL chain length tracks the observed increase in the friction coefficient (see Table 5.4). The fluorescence spectrum of MPTS

in water shows a very large shift and virtual complete loss of vibronic structure. The spectrum in water indicates that water has a very strong interaction with MPTS. Water is both a hydrogen bond donor and acceptor. Water can solvate the sulfonate anions, and it may also donate π -hydrogen bonds to the aromatic rings. In spite of the spectroscopic evidence for strong interaction between MPTS and water, orientational relaxation occurs with a diffusion constant that is consistent with stick boundary condition. This is in contrast to MPTS in the RTILs that undergoes orientational relaxation that is much slower than stick boundary conditions (see Table 5.4). Therefore, the strength of the fluorophore-solvent interaction that influences the fluorescence spectrum alone is not sufficient to explain the very slow diffusion, that is, super-stick boundary conditions (see Table 5.4).

The MPTS orientational relaxation data show strongly hindered motion that is likely caused by strongly associated solvent molecules. The most obvious possibility is that RTIL cations are bound to the sulfonate anions. A simple calculation can estimate the number of associated solvent molecules assuming the overall shape factor does not change substantially. Using the cation van der Waals volumes, the results yield 3.0, 2.8, and 3.1 cations are “attached” to each MPTS in C_2mim^+ , C_4mim^+ , and C_6mim^+ , respectively. These numbers, which are all basically 3, correspond to the number of sulfonate groups on MPTS, supporting the idea that cation coordination is responsible for the slow (super-stick) orientational relaxation of MPTS in the RTILs. Furthermore, the friction coefficient increases as the RTIL cation alkyl chain increases. The increase in friction is consistent with larger and larger cations being strongly bound to the MPTS sulfonate groups as RTIL solvent goes from C_2mim^+ to C_4mim^+ to C_6mim^+ .

5.4 Concluding Remarks

The rotational friction of perylene and MPTS have been studied in a series of 1-alkyl-3-methylimidazolium bis(trifluoromethanesulfonyl)imide ionic liquids from 298 K to 333 K. Based on these measurements, two distinct rotational environments were found. Perylene undergoes orientational relaxation in the slip to sub-slip regime, that is orientational relaxation is faster than predicted by hydrodynamic theory. As the alkyl chain length of the cation increases, the in plane and out of plane orientational relaxation friction coefficients converge to those of perylene in paraffin oil (see Table 3). The results indicate that perylene partitions into alkane-like environments. The trends in the in plane and out of plane friction coefficients suggest some degree of alkyl chain alignment along the perylene long molecular axis.

MPTS undergoes orientational relaxation with super-stick boundary conditions, in contrast to MPTS in DMSO and water, which show approximately stick boundary conditions. The slow orientational relaxation of MPTS in the RTILs cannot be ascribed to a non-specific strong solute solvent interaction. The fluorescence spectrum of MPTS in water indicates stronger interactions with water than with the RTILs yet water does not produce anomalously slow orientational relaxation. The results indicate that three RTIL cations are bound to the three MPTS sulfonate anions, and the entire assembly undergoes orientational diffusion. The increased volume of MPTS accounts for the slow orientational diffusion. The friction increases with increasing size of the solvent cation, which is consistent with the picture of cations bound to the MPTS sulfonate anion.

The results presented here provide clear evidence for solutes partitioning into distinct environments in RTILs. The location of the solute depends on its properties, in this case

non-ionic/non-polar (perylene) vs. highly charged (MPTS) solutes. For both solutes, the orientational dynamics change with the cation alkyl chain length, but for different reasons. As the alkyl chain length increases, perylene finds itself in an increasingly alkane like environment, while MPTS has increasingly large cations bound to it. Subsequent to the publication of this work, the concept of nanostructural heterogeneity has substantially evolved. At present, the feeling within the field is that the organization is not strong enough to be well represented by the micelle like cartoons drawn from MD snapshots. The results in this work are agnostic to these facts. The work clearly demonstrates strong selective solvation, to an extent that cannot be rationalized without building a local solvent phase that is nonpolar alkyl chains. For the case where a probe is present, which is the case that is of interest for the majority of applications where nanostructuring is a concern, the difference between what is experienced in this study and nanostructuring would be little more than semantics.

This work is reproduced with permission from the American Chemical Society.

5.5 References

- (1) Sureshkumar, M.; Lee, C. K. *J Mol Catal B-Enzym* **2009**, 60, 1.
- (2) Paczal, A.; Kotschy, A. *Monatshefte Fur Chemie* **2007**, 138, 1115.
- (3) Harjani, J. R.; Naik, P. U.; Nara, S. J.; Salunkhe, M. M. *Curr. Org. Synth.* **2007**, 4, 354.
- (4) Li, Z. J.; Chang, J.; Shan, H. X.; Pan, J. M. *Rev. Anal. Chem.* **2007**, 26, 109.
- (5) Hagiwara, R.; Lee, J. S. *Electrochem.* **2007**, 75, 23.
- (6) Canongia Lopes, J.; Padua, A. A. H. *The Journal of Physical Chemistry B* **2006**, 110, 3330.
- (7) Triolo, A.; Russina, O.; Bleif, H. J.; Di Cola, E. *J. Phys. Chem. B* **2007**, 111, 4641.
- (8) Iwata, K.; Okajima, H.; Saha, S.; Hamaguchi, H. *Accounts of Chemical Research* **2007**, 40, 1174.
- (9) Xiao, D.; Rajian, J. R.; Hines, L. G.; Li, S.; Bartsch, R. A.; Quitevis, E. L. *The Journal of Physical Chemistry B* **2008**, 112, 13316.
- (10) Shigeto, S.; Hamaguchi, H. *Chemical Physics Letters* **2006**, 427, 329.
- (11) Hu, Z. H.; Margulis, C. J. *Proceedings of the National Academy of Sciences of the United States of America* **2006**, 103, 831.
- (12) Jin, H.; Li, X.; Maroncelli, M. *The Journal of Physical Chemistry B* **2007**, 111, 13473.
- (13) Davis, J. H. *Chem. Lett.* **2004**, 33, 1072.

- (14) Ingram, J. A.; Moog, R. S.; Ito, N.; Biswas, R.; Maroncelli, M. *J. Phys. Chem. B* **2003**, *107*, 5926.
- (15) Mali, K. S.; Dutt, G. B.; Mukherjee, T. *Journal of Chemical Physics* **2008**, *128*.
- (16) Ito, N.; Arzhantsev, S.; Maroncelli, M. *Chemical Physics Letters* **2004**, *396*, 83.
- (17) Funston, A. M.; Fadeeva, T. A.; Wishart, J. F.; Castner, E. W. *J. Phys. Chem. B* **2007**, *111*, 4963.
- (18) Spry, D. B.; Goun, A.; Glusac, K.; Moilanen, D. E.; Fayer, M. D. *Journal of the American Chemical Society* **2007**, *129*, 8122.
- (19) Tokuda, H.; Hayamizu, K.; Ishii, K.; Susan, M. A. B. H.; Watanabe, M. *The Journal of Physical Chemistry B* **2005**, *109*, 6103.
- (20) Chuang, T. J.; Eisenthal, K. B. *The Journal of Chemical Physics* **1972**, *57*, 5094.
- (21) Perrin, F. *J. Phys. Radium* **1936**, *7*, 1.
- (22) Sension, R. J.; Hochstrasser, R. M. *The Journal of Chemical Physics* **1993**, *98*, 2490.
- (23) Youngren, G. K.; Acrivos, A. *J. Chem. Phys.* **1975**, *63*, 3846.
- (24) Xu, J.; Shen, X.; Knutson, J. R. *The Journal of Physical Chemistry A* **2003**, *107*, 8383.
- (25) Kim, Y. R.; Hochstrasser, R. M. *The Journal of Physical Chemistry* **1992**, *96*, 9595.

- (26) Manneikutla, J. R.; Ramamurthy, P.; Mulimani, B. G.; Inamdar, S. R. *Chemical Physics* **2007**, *340*, 149.
- (27) Wirth, M. J.; Chou, S. H. *The Journal of Physical Chemistry* **1991**, *95*, 1786.
- (28) Pauls, S. W.; Hedstrom, J. F.; Johnson, C. K. *J. Chem. Phys.* **1998**, *237*, 205.
- (29) Jiang, Y.; Blanchard, G. J. *Journal of Physical Chemistry* **1994**, *98*, 6436.
- (30) Troxler, T.; Stratton, J. R.; Smith, P. G.; Topp, M. R. *The Journal of Chemical Physics* **1994**, *101*, 9219.
- (31) Chaumont, A.; Wipff, G. *Journal of Molecular Liquids* **2007**, *131*, 36.
- (32) Padua, A. A. H.; Gomes, M. F.; Lopes, J. N. A. C. *Accounts of Chemical Research* **2007**, *40*, 1087.
- (33) Xiao, D.; Hines, L. G.; Bartsch, R. A.; Quitevis, E. L. *The Journal of Physical Chemistry B* **2009**, *113*, 4544.
- (34) Blanchard, L. A.; Gu, Z.; Brennecke, J. F. *The Journal of Physical Chemistry B* **2001**, *105*, 2437.
- (35) Tiwari, S.; Khupse, N.; Kumar, A. *The Journal of Organic Chemistry* **2008**, *73*, 9075.
- (36) Spears, K. G.; Cramer, L. E. *J. Chem. Phys.* **1978**, *30*, 1.
- (37) Nee, T.-W.; Zwanzig, R. *The Journal of Chemical Physics* **1970**, *52*, 6353.
- (38) Horng, M.-L.; Gardecki, J. A.; Maroncelli, M. *The Journal of Physical Chemistry A* **1997**, *101*, 1030.

- (39) Balabai, N.; Sukharevsky, A.; Read, I.; Strazisar, B.; Kurnikova, M.; Hartman, R. S.; Coalson, R. D.; Waldeck, D. H. *Journal of Molecular Liquids* **1998**, 77, 37.
- (40) Dagenet, C.; Dyson, P. J.; Krossing, I.; Oleinikova, A.; Slattery, J.; Wakai, C.; Weingartner, H. *The Journal of Physical Chemistry B* **2006**, 110, 12682.
- (41) Weingärtner, H. *Zeitschrift für Physikalische Chemie* **2006**, 220, 1395.
- (42) Hubbard, J. B.; Onsager, L.; van Beek, W. M.; Mandel, M. *Proceedings of the National Academy of Sciences of the United States of America* **1977**, 74, 401.
- (43) Lakowicz, J. R. *Principles of Fluorescence Spectroscopy*; 3rd ed.; Springer: New York, 2006.

Chapter 6: Electronic Excitation Transfer Probing of Ionic Liquid Nanostructure

Abstract

The donor-donor electronic excitation transfer of 9-phenylanthracene was measured in the ionic liquid 1-methyl-3-octylimidazolium chloride using time dependent fluorescence depolarization. The excitation transfer rate, which is sensitive to the distribution of chromophores in solution, was modeled using different configurations of dye molecules in solution. These include an isotropic distribution of chromophores to represent a totally random distribution, and also a clustered sphere model to represent the hydrophobic regions of a nanostructured environment. Model calculations were performed to demonstrate the sensitivity of excitation transfer to different distributions of probe molecules. When compared to the experiment, the isotropic model could adequately match the data. Using the clustered sphere model, an upper bound for the radius of a sphere of 6-8Å is placed on the length scale on which the heterogeneity is likely to exist.

5.1 Introduction

The concept of nanostructuring in room temperature ionic liquids (RTILs) has been an important question in understanding their structure. In addition to fundamental interest, the possible nanostructuring of RTILs has been invoked in explaining phenomena in their applications, such as gas sequestration¹, photochemistry², solar devices³, and electrodeposition⁴.

The concept of spatial heterogeneity, or nanostructuring, in RTILs has been difficult to quantify. The concept is roughly defined as an aggregation of the long alkyl chains

due to a combination of electrostatics and the hydrophobic effect. The structure has also been likened to that of a bicontinuous emulsion on a much smaller scale⁴. The effect was first detected in computer simulations, most notably those of Wang and Voth⁵ and Canongia-Lopes and Pádua⁶. While some effort to quantify the properties of the nanostructural organization were undertaken based on these simulations, especially with the development of a heterogeneity order parameter⁷, there was substantial ambiguity on what the concept meant. In some sense, the strongest understanding came from the color coded snapshots from simulation trajectories that, while visually striking, did not fully quantify the phenomenon. Experimental indications of spatial heterogeneity came from other sources^{8,9}, the strongest of which were x-ray scattering experiments¹⁰⁻¹⁴. The connection between these studies and what is typically understood when discussing the nanostructuring has, however, been called into question by neutron studies which do not seem to indicate the presence of substantial nanostructuring¹⁵. This and other work¹⁶ has contracted the length scale on which the hydrophobic regions likely exist. The length scale of the nanostructuring is still an outstanding question. Size estimates have also varied widely, from tens of nanometers⁹ to 18 Å¹⁷, to 6-8 Å¹⁸.

One consequence of the amphiphilic nature of the ionic liquid is the selective solvation of small molecules dissolved in the RTIL. In the context of a nanostructured solvent, this is equated with partitioning of the solute into the appropriate phase. Evidence for this phenomena have be seen in fluorescence^{19,20} and Optical Kerr effect studies²¹. This partitioning appears to preserve the features of the surrounding solvent, such that the intruding probe molecules do not completely perturb the surrounding solvent structure. For an ionic liquid where minimizing the highly energetic Coulomb

interactions between ions is likely the dominant force, this is not particularly surprising. This suggests that the distribution of an appropriately chosen probe may be capable of reporting on the structure of the moiety into which it prefers to interact.

Excitation transfer has been successfully used as a tool to spectroscopically address structural problems. Most commonly this is manifested in FRET experiments involving a system with a single transfer between donor and acceptor. This is in part due to the simplicity of the mathematical treatment and amicability to a number of experimental techniques. At its heart is high spatial sensitivity due to the $1/r^6$ dependence of the Forster transfer mechanism. The sensitivity is retained for more concentrated chromophore systems; however the mathematical treatment of the problem becomes more intense. This is because the presence of many donors and acceptors creates far more numerous pathways for the excitation to migrate. The first highly exact solution to this problem was provided by Gochanour et. al.²². Using a topological reduction, they were able to provide a solution to the problem of energy migration that incorporated an infinite number of particles over different pathways. The results were found to be highly accurate²³, and these results were then expanded to consider cases of restricted and other complex geometries²⁴⁻²⁸.

In many cases, it was found that a simpler theory, derived from a two-body approximation was able to reproduce experimental results²⁹. This was important, because the two body theory is easier to treat. For a distribution of chromophores, it is straightforward to calculate easily measured spectroscopic observables. This approach has been applied to understanding spatial relations in a number of systems, especially polymers³⁰⁻³³ and micelles^{34,35}. The treatment of clustered systems is capable of treating

an inhomogeneous solvent similar to the structure postulated to exist in the ionic liquids³⁶. Prior studies have shown that nonpolar solutes appear to selectively interact with the nonpolar tails of the ionic liquids. In the context of a nanostructured ionic liquid, this corresponds to segregating into the nonpolar domains. Since these restrict the distribution of chromophores on length scales similar to the Forster radius, the effect should modulate the electronic excitation pathways available to a concentrated chromophore system.

In this study, the nonpolar chromophore 9-phenylanthracene (9PA) was used to study the process of excitation transfer in a highly viscous ionic liquid 1-methyl-3-octylimidazolium chloride (OmimCl). 9PA was chosen to be relatively small in size, nonpolar, soluble in relatively large concentrations without forming dimers, and to have a donor-donor Forster radius on the order of the expected spatial heterogeneity. OmimCl was chosen because prior experiments indicate it is potentially nanostructured, and because high viscosity is required to separate the effect of molecular rotation from the excitation transfer. The nanostructuring corresponds to a restricted spatial distribution of the 9PA, which is expected to partition into any nonpolar domains. This deviation from the isotropic distribution of dye molecules one would expect in a simple solvent will have a direct effect on the excitation transfer process. Moreover, using a clustered model, it is possible to approximate a length scale on which the heterogeneity exists.

5.2 Excitation Transfer Theory

The basis for this work is an expansion of the original two-body theory to consider clustered systems²⁹. The quantity of interest throughout is $\langle G_s(t) \rangle$, which denotes the probability that an excitation resides on the originally excited molecule at time t . For a

spatial configuration of other chromophores, the rate at which the excitation is transferred away from the originally excited molecule depends on the configuration and also the transfer rate from the Forster dipole-dipole coupling³⁷

$$E(t) = \frac{1}{2} (1 + \exp(-\frac{2t}{\tau} * (\frac{R_o}{r})^6)) \quad (6.1)$$

If the assumption is made that the rate of decay between two particles is independent of other particles (the two-body approximation), then the total decay of $\langle G_s(t) \rangle$ becomes the product of all pairwise rates. Taking the logarithm and truncating the power series at first order yields

$$\langle G_s(t) \rangle = \frac{c}{2} \int (1 - \exp(-\frac{2t}{\tau} * (\frac{R_o}{r})^6)) * u(\mathbf{r}) d\mathbf{r} \quad (6.2)$$

where c is the concentration of chromophores, τ the fluorescence lifetime, R_o the Forster radius. $u(\mathbf{r})$ is the vector distribution defined so that $c u(\mathbf{r}) d\mathbf{r}$ is the probability of finding another chromophore at \mathbf{r} relative to the initially excited molecule, which is set at the origin. For an isotropic system in which all initial positions are equivalent, Equation 6.2 can be directly evaluated analytically yielding

$$\langle G_s(t) \rangle = \exp[-\frac{\sqrt{8\pi^3}}{3} c R_o^3 \sqrt{\frac{t}{\tau}}] \quad (6.3)$$

This has been experimentally verified in a number of randomly distributed systems^{23,32}, and also compares very well with the more exact treatment of Gochanour for relatively short times ($t < 2\tau$) and lower reduced concentrations ($C = \frac{4\pi}{3} * c * R_o^3 < 2$)³⁸. For chromophores on non-identical sites, an average over initial configurations must be performed on Equation 6.2, yielding

$$\langle G_s(t, N) \rangle = 1/V_d \int_{V_d} G_s^1(t, \mathbf{r}_d) u(\mathbf{r}_d) d\mathbf{r}_d \quad (6.4a)$$

$$G_s^1(t, \mathbf{r}_d, N) = \exp\left[-\frac{(N-1)}{2V_a} \int_{V_a} [1 - \exp(-\frac{2t}{\tau} \left(\frac{R_o}{r_{ad}}\right)^6)] u(\mathbf{r}_a) d\mathbf{r}_a\right] \quad (6.4b)$$

where $u(\mathbf{r}_j)$ is the distribution of donors and acceptor molecules, V_j is the volume occupied by the donors and acceptors, N is the total number of chromophores (donor + acceptors) and r_{ad} is the distance between donor and acceptor. Equation 6.4 is the basis for all subsequent manipulation, by incorporating the appropriate forms of $u(\mathbf{r})$.

At this point, a particular form of $u(\mathbf{r})$ must be supplied, based on a hypothesized distribution of chromophores in the system. To describe the possible nanostructuring of RTILs in a form that manifests the important characteristics of the nanostructuring while remaining computationally tractable, a form of clustered spheres is taken. Because the 9PA is likely to partition into the hydrophobic regions, these are treated as spherical cavities of radius R_s that pack like hard spheres. This incorporates the important feature of nanostructuring with the hydrophobic regions as populated cavities and excluded exterior spaces as the hydrophilic region of head groups and anions. Within the hydrophobic pocket, the dye can be distributed anywhere – it is locally isotropic.

Marcus et. al. give a complete treatment of excitation transport in clustered systems³⁶. An important result is that the excitation transport and $\langle G_s(t) \rangle$ can be factored into two parts

$$\langle G_s \rangle = \langle G_s^{on} \rangle * \langle G_s^{off} \rangle \quad (6.5)$$

corresponding to the probability decay as the result of excitation transfers within the cluster (on), and excitation transfer between clusters (off). This comes directly from the

two-body approximation use to arrive at Equation 6.4. Breaking up the calculation simplifies the necessary expressions, both parts of which will be treated separately.

$\langle G_s^{\text{on}}(t) \rangle$ can be obtained by applying the appropriate spherical geometry to Equation 6.4. A change of coordinates can simplify this calculation. The interior integration is performed of the vector separating the donor and acceptor, r_{ad} . The exterior integration is still over all r_d relative to the sphere's center, but r_a is recast as a function of spherical coordinates of r_{ad} and θ_{ad} , where θ_{ad} is the angle between the r_d and r_a . Using this transformation, Equation 6.4 becomes

$$\langle G_s^{\text{on}}(t, N) \rangle = \frac{4\pi}{V} \int_0^{R_s} r_d^2 \exp\left[\frac{-\pi(N-1)}{V} \int_{-1}^1 dq \int_0^{f(r_d, q)} \left(1 - \exp\left[\frac{-2t}{\tau} * \left(\frac{R_o}{r_{\text{ad}}}\right)^6\right]\right) r_{\text{ad}}^2 dr_{\text{ad}}\right] r_d^2 dr_d \quad (6.6)$$

where

$$q = \cos(\theta_{\text{ad}})$$

$$f(q, \theta_{\text{ad}}) = \sqrt{R_s^2 + r_d^2 - 2r_d^2(1 - q^2) - 2qr_d\sqrt{R_s^2 - r_d^2(1 - q^2)}}$$

The tendency of the curves for $\langle G_s^{\text{on}}(t) \rangle$ to unity at small R_s is the result of a constant chromophores density, which makes the population on individual spheres scale with R_s^3 . This result has been compared to a more exact treatment, and found to agree well in the normal limits^{25,39,40}.

$\langle G_s^{\text{off}}(t) \rangle$ is obtained in a similar fashion from Equation 6.4, except that the integration for the donor and acceptor molecules are over separate spheres separated by distance D . The problem is first treated with a single, fixed D , and then expanded to consider a large number of spheres at different separations. To compactly perform the

required integrations, a multi-frame coordinate system is used³⁶. The transformation of $\mathbf{r}_a \rightarrow \mathbf{A}\mathbf{r}_{ad}$ transforms Equation 6.4 into

$$G_s^{off}(t, D, N) = \frac{2\pi}{V_d} \int_0^{R_s} \int_0^\pi G_s^1(r_d, t) \sin(\theta) r_d^2 dr_d d\theta_d \quad (6.7)$$

$$G_s^1(r_d, t, N) = \exp\left[\frac{N-1}{\pi V_a} \int_0^{R_s} \int_0^\pi (\exp\left[\frac{-2t}{\tau} \left(\frac{R_o}{r_{ad}}\right)^6\right] - 1) r_a^2 \sin(\theta_a) dr_a d\theta_a\right]$$

$$|r_{ad}|^6 = [r_d^2 + r_a^2 + 2D[r_a \cos(\theta_a) - r_d \cos(\theta_d)] - 2r_a r_d \cos(\theta_a - \theta_d) + D^2]^3$$

The limit of $D=0$ gives the case of two spheres sitting on top of one another, which yields another route to $\langle G_s^{on}(t, N) \rangle$. For all other cases, Equation 6.7 must be treated numerically.

To approach a realistic picture of the ionic liquid structure, the result of integrating Equation 6.7 must be expanded to consider a large number of spheres at different spacings. Again appealing to the two-body nature of the problem, the decay of $\langle G_s^{off}(t, D, N) \rangle$ can be written as a product of all two sphere interactions between pairs of spheres. Taking the limit as the number of spheres becomes large leads to the thermodynamic limit of $\langle G_s^{off}(t, N) \rangle$, which can be expressed as³⁶

$$\langle G_s^{off}(t, N) \rangle = \exp\left[-4\pi c_s \int_{2R_s}^\infty [1 - G_s^{off}(t, D, N)] g(D) D^2 dD\right] \quad (6.8)$$

for a distribution of spheres of macroscopic concentration c_s and radial distribution $g(D)$. The lower bound is set to prevent overlap of spheres, and the upper limit is expanded to infinity because the contribution from spheres outside several R_o is negligible.

At this point, $\langle G_s(t, N) \rangle$ has been solved at constant number of chromophores per cluster. Since only the macroscopic cluster concentration is specified, the distribution in chromophores number must be treated. Assuming the chromophores do not interact, the

number of chromophores within any sphere will follow a Poisson distribution. Therefore, the observed $\langle G_s(t,c) \rangle$ will be the product of Poisson weighted contributions of $\langle G_s^{on}(t,N) \rangle$ and $\langle G_s^{off}(t,N) \rangle$, with Equation 6.6 becoming

$$\langle G_s^{on}(t,c) \rangle = \sum_{N=1}^{\infty} \left(\frac{e^{-v} v^{N-1}}{(N-1)!} \right) \frac{4\pi}{V} \int_0^{R_s} r_d^2 \exp\left[\frac{-\pi(N-1)}{V} \int_{-1}^1 dq \int_0^{f(r_d,q)} (1 - \exp\left[\frac{-2t}{\tau} * \left(\frac{R_o}{r_{ad}} \right)^6 \right]) * r_{ad}^2 dr_{ad} \right] r_d^2 dr_d \quad (6.9)$$

and Equation 6.7 becoming

$$\langle G_s^{off}(t,c) \rangle = \exp[-4\pi c_s] \sum_{N=1}^{\infty} \left(\frac{e^{-v} v^{N-1}}{(N-1)!} \right) \int_{2R_s}^{\infty} [1 - G_s^{off}(t,D,N)] g(D) D^2 dD \quad (6.10)$$

where v is the expectation number of chromophores on a cluster, equal to the macroscopic concentration of chromophores divided by the concentration of clusters. This form of the Poisson distribution neglects all contributions from clusters containing $N=0$, because they will not contribute to any fluorescence events.

Combining Equations 6.9 and 6.10 in Equation 6.5 gives the final result for the $\langle G_s(t,c) \rangle$. The importance in this quantity lies with its connection to experimental observables. For a randomly oriented distribution of chromophores, the dominant source of polarized fluorescence emission comes from the initially excited molecule⁴¹. Therefore, the decay in the polarization of the fluorescence emission reports on the probability that the emission comes from the same molecule that was initially excited, i.e. $\langle G_s(t) \rangle$. If the molecular rotation is slow and uncorrelated with the excitation transfer, then the anisotropy, defined as

$$r(t) = \frac{I_{\parallel}(t) - I_{\perp}(t)}{I_{\parallel}(t) + 2I_{\perp}(t)} \quad (6.11)$$

can be represented as the product of the anisotropy decay due to molecular rotation, and the anisotropy decay due to excitation transfer, i.e.

$$r(t) = \Theta(t) * \langle G_s(t, c) \rangle \quad (6.12)$$

The contribution from molecular rotation, $\Theta(t)$, can be measured in a low concentration sample, where excitation transfer will be negligible. Because the chromophores in this experiment are slowly rotating, the typically used orientationally averaged Forster rate is not applicable. This can be calculated from the orientational relaxation rate and the expected excitation transfer rate through a correction factor included in the Forster transfer rate⁴². The correction applies to the orientational factor $\langle \kappa^2 \rangle$ in the Forster coupling to reflect the amount of orientational averaging experienced while undergoing excitation transport. For these experiments, $\tau_{rot} \approx 5 * \tau_{transfer}$, for which the correction is between .84 and .90, depending on chromophores concentration. Thus, each instance of the Forster rate incorporates this concentration correction $\Gamma(c)$, as

$$\left(\exp\left(-\frac{2t}{\tau} \Gamma(c) \left(\frac{R_o}{r_{ad}^6}\right)\right) - 1 \right) \quad (6.13)$$

5.3 Experimental Methods

The 1-methyl-3-octylimidazolium chloride (OmimCl) was obtained from Iolitec at 99+% purity. 9-phenylanthracene (9PA) was obtained Aldrich at maximum purity and used without further purification. The OmimCl was dried upon reception under vacuum at 60°C for 5 days and then transferred into a nitrogen glove box. Water content was measured using Karl-Fischer titration (Mettler DL39) to be less than 500ppm by weight.

A carefully prepared stock solution of 9PA in methylene chloride was made using calibrated glassware. Measured amounts of this stock solution were added to a test tube and the solvent gently evaporated, leaving behind the dye. These were transferred to the glove box and then stirred with precisely weighed quantities of dry OmimCl. The ionic liquid solution was then transferred to a custom sample cell with variable path length, and sealed in a constant temperature cryostat (Janus ST-100) under dry nitrogen. Absolute exclusion of additional water was imperative, as small quantities of absorbed water will change the viscosity of the sample, making correction for the solute rotation impossible. Samples were prepared with peak optical densities around .3 to minimize fluorescence absorption and re-emission.

The experimental setup for the time correlated single photon counting system has been described previously. Samples were excited at 375nm, and the fluorescence was detected at 426nm after passing through a longpass Schott glass filter to remove scattered excitation light. On each sample, time dependent fluorescence intensities were collected in parallel, perpendicular, and magic angle (54.7°) geometries. For the low concentration sample, the excitation volume in the cuvette was moved around to minimize the impact of photobleaching, which could interfere with proper removal of background fluorescence. For all high concentration samples, the effect of background fluorescence was negligible. For the low concentration sample, the background fluorescence of trace impurities in the OmimCl was removed by swapping in a blank sample under equivalent equipment settings.

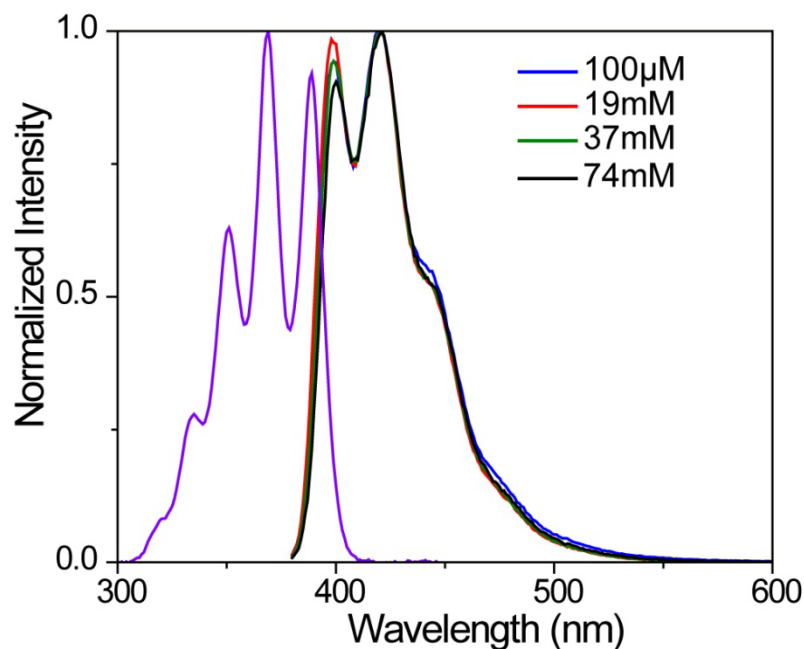


Figure 6.1 – Normalized fluorescence and absorption spectra for the 9PA dissolved in OmimCl. All spectra shared nearly identical absorption spectra. The different fluorescence curves correspond to the different 9PA concentrations used in the study. Any excimer or dimer formation would be expected to result in a shoulder at long wavelengths.

On each sample, a UV/Vis absorption was taken with a Cary 6000i spectrometer. Steady state fluorescence scans were taken at 375nm excitation wavelength on a Fluorolog 3 fluorimeter. No evidence for excimers or dimers was seen in the fluorescence emission spectra for the concentrations used, as seen in Figure 6.1. The Forster radius of 9PA was also calculated as 19.7Å from a measured overlap integral, quantum yield, and using literature values for index of refraction⁴³.

5.4 Results and Discussion

5.4.1 Model Calculations

In performing calculations using Equation 6.10, a bulk cluster concentration is required. Whereas in the cases of polymers or micelles the cluster concentration is straightforward (being the bulk concentration of polymer or micelles), for the possible spatial heterogeneity in the RTILs, a different approach must be taken. The concentration of spheres is estimated by assuming a bulk volume fraction of spheres ϕ , which lends itself to the cluster concentration by

$$c_{cluster} = \frac{3\phi}{4\pi} \left(\frac{R_o}{R_s} \right)^3 \quad (6.14)$$

Similarly, the expectation value for the chromophore number per sphere is given by

$$\nu = \frac{CR_s^3}{\phi} \quad (6.15)$$

For the case of OmimCl, the volume fraction was estimated using the Van der Waals volumes of the ions. The hydrophobic region was assumed to be composed of the eight carbons on the octyl chain. The hydrophilic region was taken to be the methylimidazolium part of the cation, and the entirety of the chloride anion. Using these divisions, a volume fraction of 0.72 is calculated. At low occupation numbers ν , where time dependent contributions to the Poisson averaging are dominated by the $N=2$ term, the factors of ϕ cancel.

Using Equations 6.9 and 6.10, it is possible to model possible $\langle G_s(t) \rangle$ curves for different spatial distributions. Numerical integration of the data was done using iterated 30 point Legendre-Gauss quadrature. Figure 2 shows some predicted curves for a reduced bulk chromophores concentration of $C=1$ using clustered spheres and the

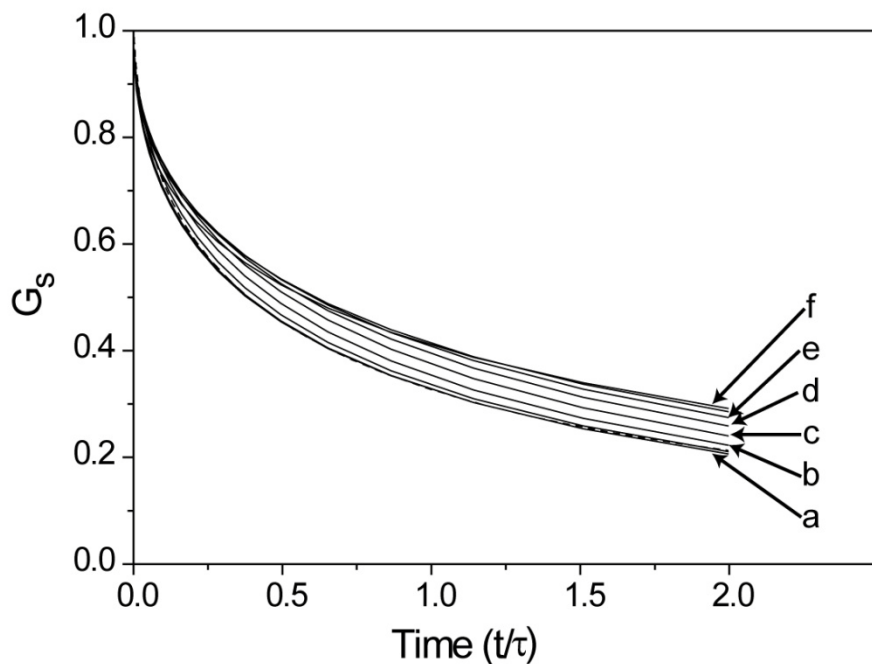


Figure 6.2 $\langle G_s(t) \rangle$ calculated for various normalized R_s (R_s/R_o) and the isotropic model. Curves for $R_s = 0.1, 0.2, 0.3$ and the isotropic model all fall within (a). Curve (b) through (e) are $R_s = 0.4, 0.5, 0.6, 0.7$ and 0.8 respectively. (f) contains $R_s = 0.9, 1.0$. For larger values of R_s , the shape begins to substantially change and the excitation transfer speeds up (left out for clarity). The time coordinate is normalized relative to the fluorescence lifetime for this and all subsequent plots.

isotropic model. At very small sphere radii, the curves predicted by the clustered sphere model approach the isotropic model. The similarity comes from the short distances over which the distribution of the chromophores changes relative to R_o , which averages out any structure. In effect, the clusters themselves act like individual chromophores. Since the spheres are almost isotropically distributed, the effective chromophores distribution also looks isotropic. There is a slight amount of difference between the small sphere

limit and isotropic model owing to the quantization in the Poisson average used for the sphere calculation. The shape of the curve is still a stretched exponential, but the effective reduced concentration is slightly reduced by 5%. Since the value of R_o cannot be that closely established, the two cases are effectively identical. The other limiting case is at very large sphere radii. The model again begins to look isotropic because the majority of the chromophores are too far removed from the boundary to feel its effect. Since the chromophores inside the spheres are isotropically distributed, this recovers the bulk isotropic curve shape. Again the concentration is scale, but this time by the inverse volume fraction. The excitation transfer in this limit is dominated by the $\langle G_s^{(on)} \rangle$. But within the sphere, the effective chromophores concentration is enhanced relative to the apparent bulk concentration by the volume fraction, increasing the rate of excitation transfer. Between these two extremes, the clustered sphere model shows a difference from the isotropic model that is very sensitive to the size of spheres.

The region of sensitivity of the excitation transfer to sphere size is for sphere radii from approximately $0.3 \cdot R_o$ to $3 \cdot R_o$. The range of sensitivity depends slightly on the average chromophores number per sphere. As the size of the sphere is increased at constant bulk concentration and volume fraction, the rate of excitation transfer initially decreases as the excluded regions between spheres becomes important. The trend continues until about $R_s = R_o$, when the excitation transfer reaches its slowest rate. Further increasing the size of the sphere will then begin increasing the rate of excitation transfer, especially at early time. The acceleration at early time comes from the excitations occurring in the center of the sphere. The time coordinate of $\langle G_s(t) \rangle$ is in some sense a measure of distance. The transfer rate in Equation 6.1 contains the ratio of t/r_{ad}^6 . Thus,

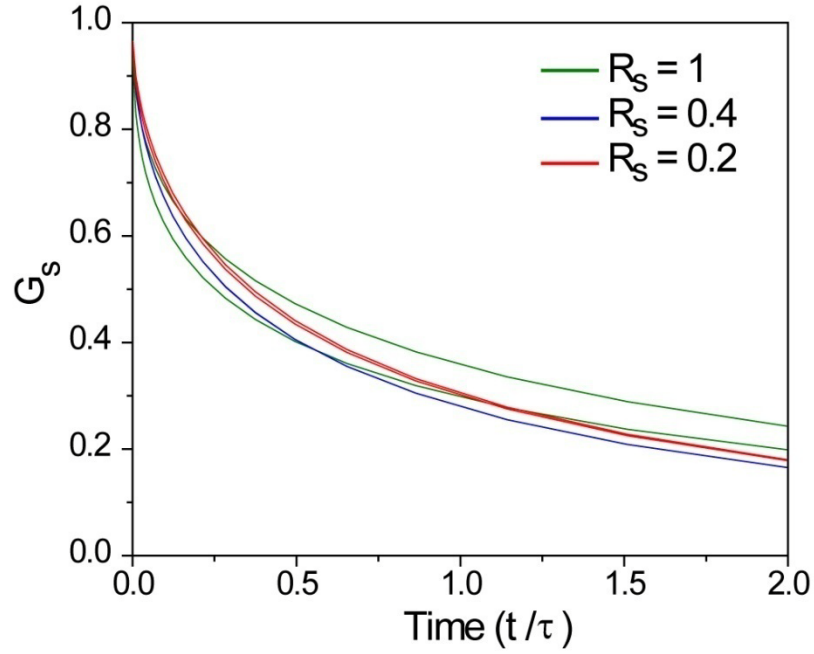


Figure 6.3 $\langle G_s(t) \rangle$ plotted for volume fractions $\phi=0.5$ and 0.7 for three R_s . Both red curves for $R_s=0.2$ are identical, and the blue curves for $R_s=0.4$ are almost identical. For $R_s=1$, there is significant difference, owing to the substantial contribution from multiply populated spheres.

all things otherwise equal, the transfer events happening at earliest time will be dominated by close neighbors, to maintain the ratio of t/r_{ad}^6 . For larger spheres, this means that excitations happening in the center of the sphere will be enhanced by the lessened influence of the far away boundary. As the sphere is made larger, the excitation transfer accelerates at later times, eventually converging on its limit.

It is important to consider the sensitivity of the model to auxiliary inputs such as the radial distribution function of spheres and volume fraction. An excessive sensitivity will lead to model selection problems and limit the robustness of the sphere model as an

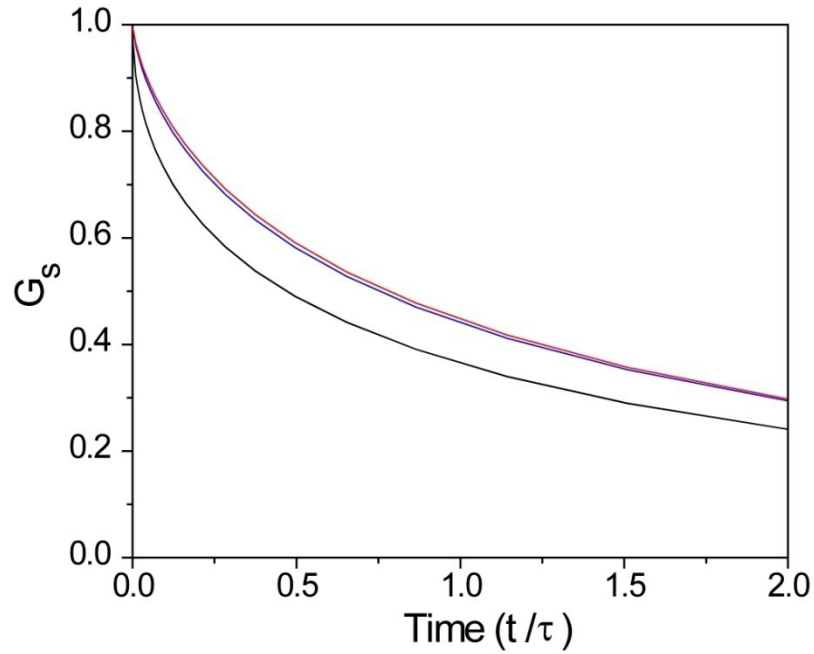


Figure 6.4 $\langle G_s(t) \rangle$ for different models of sphere packing at different R_s . The curves for $R_s=2$ are identical for both a uniform packing of spheres and using the radial distribution function for a hard sphere liquid. At $R_s=6$, the curves for the two sphere packings are again very similar.

analogy to nanostructuring. The Figure 6.3 shows the expected observable for two cases of sphere volume fractions, 0.5 and 0.7, at a bulk concentration of $C=1$. At small R_s the curves are identical, consistent with the limits described above. The difference between the curves is still relatively minor at an intermediate size, and starts to become substantial once R_s approaches R_0 . For 9PA, R_0 is about 20\AA . While the volume fraction makes a difference at these large sizes, structure on very large scale is considered unlikely. At smaller length scales that more closely resemble the sizes implicated in other experiments, the sensitivity is much less. A second input is the radial distribution

function for the spheres. Three cases are calculated for a small and intermediate sphere size. One uses a simple isotropic distribution of clusters. The second uses the same functional form, but with the inner cutoff extended outward. This simulates to a degree the hydrophilic region that serves to separate different spheres. The last case includes a slightly modulated radial distribution function in Equation 6.10 to include the $g(D)$ for a hard sphere liquid at the same packing density⁴⁴. Again a similar trend is shown in Figure 6.4, with increasing, but modest effect over the range of sphere sizes expected. These results support the robustness of using the sphere model to capture the essence of any nanostructuring at small scales (R_s relative to R_o) while containing only a few parameters. At larger scales, these inputs become important and must be addressed. However, for the data in this experiment, discussed below, the length scales appear to be small enough to warrant the simple picture at small sphere distances.

Another important distinction evident in the model calculations is the functional form of the calculated decay curves. For the isotropic model of chromophores distribution, a near universal curve is predicted. Outside the weak dependence of the orientational factor correction on chromophores concentration, the curves are all stretched exponentials with a stretching factor of 0.5 and time coordinate scaled by C^2 . Most measurements are going to be bound by the errors in effectively measuring the Forster radius of the donor-donor excitation transfer. The challenge is especially strong in these RTIL samples, where autofluorescence and scattering from entrained bubbles over long pathlengths amplify the challenges of an already difficult measurement. Errors in R_o make a zero-parameter fit of the data difficult. However, even with errors in R_o , the universality of the curve shape means a fit to the isotropic

model can be made by adjusting R_o as a parameter. Comparison between isotropic chromophores distribution and clustered sphere models show that only in the limiting cases of R_o ($R_o \rightarrow 0$ or $R_o \rightarrow \infty$) can fully overlap the two sets of curves at all times. Thus, model selection can be successful even in the face of errors in measuring the Forster radius because the shape of the curves contains the signature of the appropriate model.

5.4.2 Experimental Results

$\langle G_s(t) \rangle$ for 9PA taken by removing the rotational contribution from the fluorescence anisotropy via Equation 6.12. These are compared to the predictions from the isotropic and clustered sphere models of excitation transfer. In Figure 6.4, the data are compared to the isotropic model of chromophores distribution using the best estimate for the Forster radius. Here, there is reasonable agreement at early and late time, with large deviations at intermediate time. This comparison contains no adjustable parameters, and is not contingent upon externally supplied values for radial distribution functions or volume fraction. It is, however, sensitive to the errors in measuring the Forster radius. To accommodate this, the data is also fit using the isotropic model, but with R_o made into an adjustable parameter. To include the information from all three concentrations simultaneously, the fit is performed globally using weighted non-linear least squares. The variances for the experimental data, are used as weighting factors. The results are shown in Figure 6.5. By adjusting R_o downward from 19.7 to 19.5, this treatment improves the fit, decreasing the value of the reduced χ^2 from 185 to 143. The large values for χ^2 indicate the bias in the model relative to the data, as also evident from the residuals. For this reason, standard errors from the least square fit are not the appropriate statistic to compute fit errors and confidence intervals. To approximate the confidence

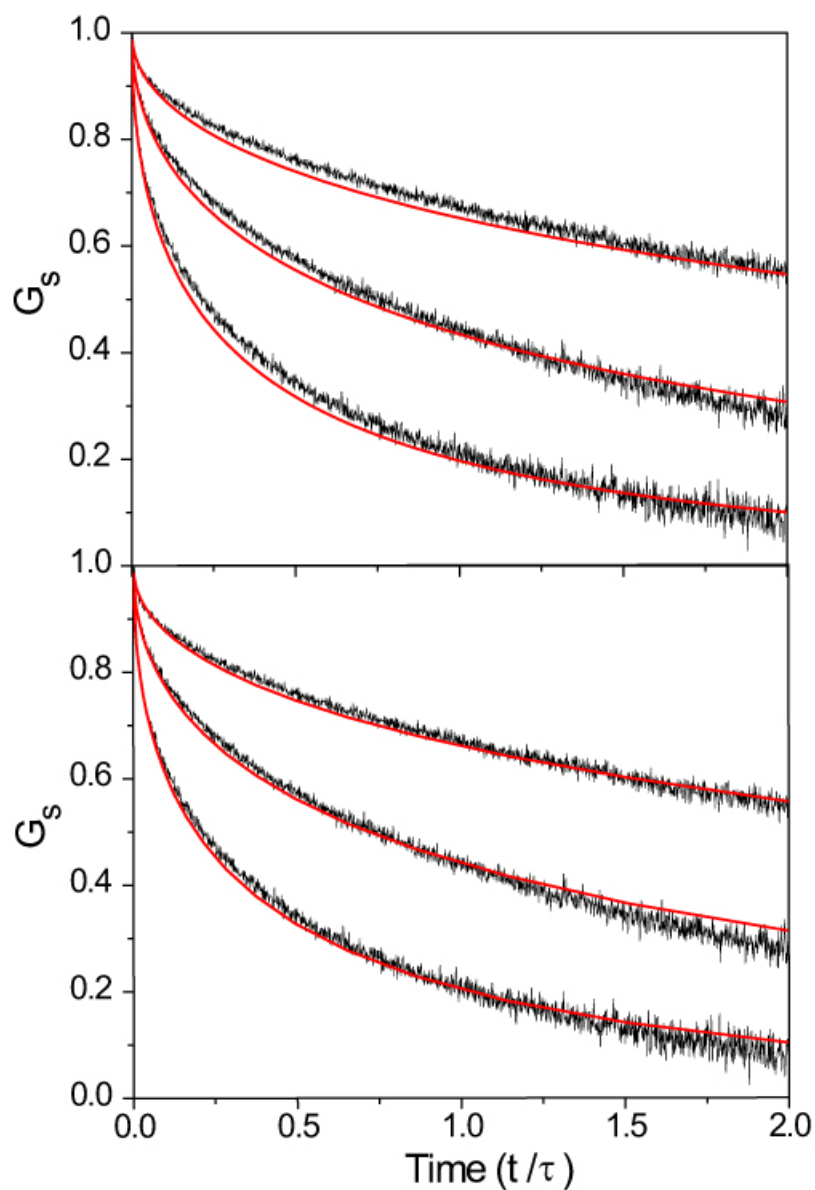


Figure 6.5 Global fits to the experimental data using the isotropic model. The top graph uses the experimental value of 19.7Å for R_0 and contains no adjustable parameters. The bottom graph uses R_0 as an adjustable parameter, arriving at a value of 19.3Å. There is a slight improvement in the fit for the second graph.

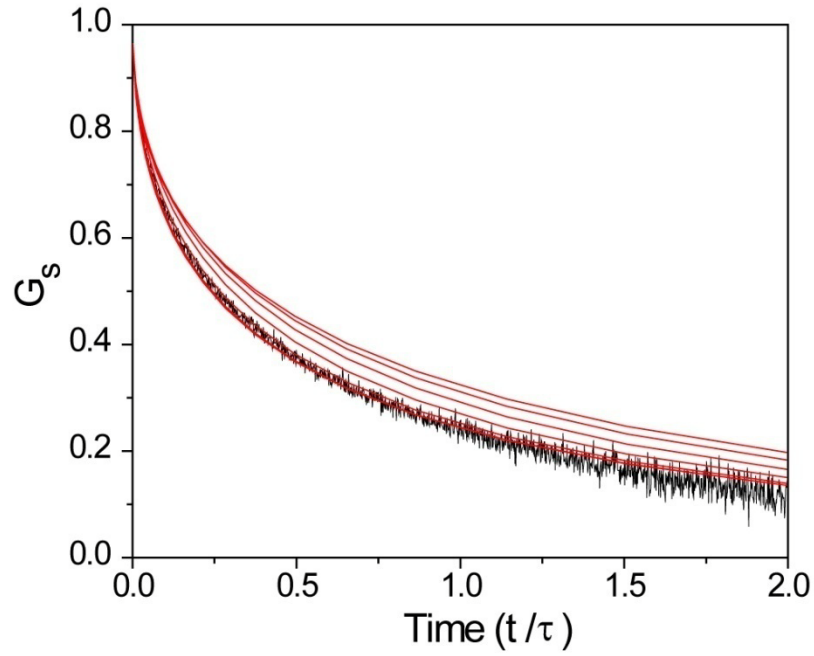


Figure 6.6 Experimental data compared to different R_s for the clustered sphere model. For clarity, only the curves for the most concentrated sample are shown, although all concentrations are very similar. The red curves shown are for, in ascending order, $R_s = 0.1, 0.2, 0.3, 0.4, 0.5, 0.6$, and 0.7 . The best fit corresponds to the curve for $R_s = 0.1$, which is identical to the isotropic fit.

intervals for this fit, resampling of the residues is performed⁴⁵. This is a bootstrap method that uses the residuals and fit parameters to create a synthetic data set to refit. Repetition builds up sufficient statistics to approximate the true distribution from which the estimates of R_0 are drawn. Using this approach, a 95% confidence interval for R_0 is constructed by ordering each estimate and finding the appropriate cutoffs from the list. For the isotropic model, this leads to a 95% confidence interval of [19.0, 20.3]. The skew in this interval relative to the global maximum is a consequence of the bias in the model.

Figure 6.6 shows the same treatment, but instead using the clustered sphere calculations. Because the small sphere limit corresponds with the isotropic model, the fits look rather similar when using the best estimate for the Forster radius. For the case of clustered spheres, no simple regression can be performed because the model contains two parameters (R_o and R_s), both of which are coupled when optimizing fits to $\langle G_s(t) \rangle$. Thus, there the risk that the bias will cause a poor selection of parameters, even though the least square fit is better. There is additional information, however, in that there is some estimate of what the Forster radius should be. Using Bayesian inference, this corresponds to prior knowledge on the distribution of parameters that the model parameter R_o . By incorporating this information into the fitting of the data, an optimum solution can be found which allows for a better fit of the data without using unrealistic parameters.

One way to accomplish this is using regularized optimization. Here, the data is fit using a cost function C that has the form

$$C(\theta) = L((x - x')^2) + \lambda R(\theta) \quad (6.16)$$

where L is the least square loss function, and R is a penalty function on the parameters of the model θ . In the Bayesian interpretation, L corresponds to the likelihood function, and R to the prior probability for the model parameters⁴⁶. The parameter λ is left as a tuning parameter, and is usually somewhat difficult to set. One approach is to fit the data using many values of λ , and then use some external approach such as cross-validation to choose the best value. However, given the structure of the data and the prior, this approach is not likely to accurately incorporate the certainty of the prior. To estimate the value of λ , one needs information on the magnitude of the loss function and its confidence intervals.

Under the assumption that these are similar to the values approximated from the isotropic fit to the data, the tuning parameter is set to equate the uncertainties in the loss function to those in those uncertainties in the prior at the 95% confidence interval. For the prior on R_o , this is taken to be Gaussian with a standard deviation of 1\AA . This value is significantly larger than would be predicted from the individual errors when measuring the Forster radius. But given the difficulties in measuring the constituents to the Forster radius, the added width makes the prior more conservative to account for unknown sources of error. For the sphere radius, a uniform prior from 0 to R_o is chosen which effectively removes it from the regularization. Larger values of R_s are excluded based on the impossibility of constructing a sphere using the ions of OmimCl that can maintain ion pairing requirements. This length corresponds to the approximate length of an 1-methyl-3-octylimidazolium ion with the octyl tail with all carbons in the trans conformation.

Using the values of χ^2 over the resampled confidence intervals, and a penalty function as the inverse of the Gaussian prior,

$$R = \left[\frac{1}{\sqrt{2\pi}} \exp\left(-\frac{(R_o - 19.7)^2}{2}\right) \right]^{-1} \quad (6.17)$$

a value of 3.1 is obtained for λ . Using this functional form, small deviations from the spectroscopic R_o will be lightly penalized, while large deviations (greater than 2σ) will be strongly penalized. With this value, the data are fit to obtain a best estimate for the clustered sphere model with respect to the data. The optimization gives $R_o=19.9$, and $R_s=0.3$. Clearly these values are sensitive to the functional form of the penalty and tuning parameter. Because the prior was very generously chosen, what the regularized approach suggests is a boundary on the size of the spheres in the model. Larger values of R_o will lend themselves to slightly better fits at larger R_s . To do so, however, means

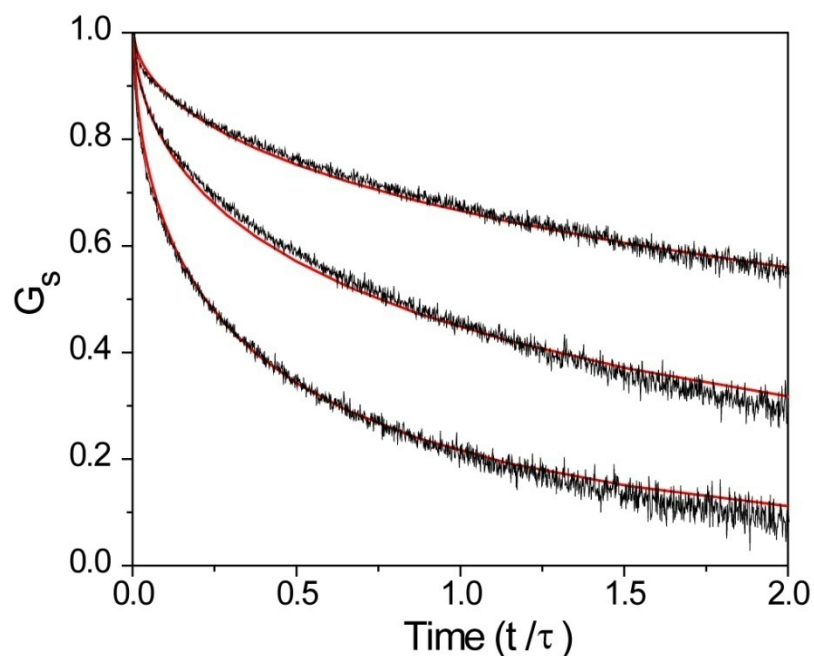


Figure 6.7 $\langle G_s(t) \rangle$ fits for the regularization optimized clustered sphere model. The three curves correspond to the three concentrations used in the study. The fits correspond to curves for $R_o = 19.9$ and $R_s = 0.3$.

pushing further from the spectroscopically measured value of R_o , and increasing the chances of accidental improvements in the fit. Figure 6.7 shows the fits for this data set.

Comparing the results, the isotropic model was substantially able to fit the data, especially when R_o was allowed to vary slightly. Since the isotropic model is effectively a limiting case of the clustered sphere model, it too was able to fit the data. The regularized optimization further allows the parameters to vary within conservative estimates of what R_o should be. Under this slightly relaxed condition, a sphere radius of 0.3 was obtained. All of these values fall within small sphere limit for clustered sphere model when considering the effect of additional parameters such as sphere volume

fraction and the radial distribution of the spheres. Therefore, their effect is expected to be minimal. Using the fact that the 9PA molecules are likely selectively solvated by the aliphatic moieties, corresponding to partitioning in a nanostructured phase, what these result suggest is an upper bound on the length scale at which any nanoscale heterogeneity can exist – as represented by the spheres in the clustered sphere model. From the regularized fits, this corresponds to a length scale of about 6\AA radius.

The value of 6\AA puts the results of this experiment in line with more experiments,^{15,16} which have tended to reduce the prominence which nanostructural organization is expected to play. 12\AA (the diameter of the spherical representation) is not substantially bigger than normal molecular dimensions for solvents and solutes, such as 9PA which has a long axis of about 9\AA . At these lengths scales, it is not entirely obvious when a phenomena is nanostructural organization, and when it is simply a consequence of selective solvation paired with the finite size of molecules. These conclusions are drawn based on the ionic liquid solvating a probe. This means that the experiment does not necessarily directly relate to the structure of the pure ionic liquid accessed in most scattering experiments conducted to date. It is unlikely, though; that the presence of a probe would decrease the length scales of homogeneity, such that the upper bound still stands. Moreover, the upper bound forces one to reconsider what the actual mechanism is for results using ionic liquids in macro-assemblies. For large nanostructures, it is unlikely that any nanostructural organization is being template, but rather the amphiphilic nature of the ionic liquid coupled with specific traits of importance. While the widespread success in using ionic liquids to facilitate nanostructures is not in question⁴⁷⁻⁴⁹, it does present caution for the mental model when attempting to develop new systems.

5.5 Concluding Remarks

The donor-donor excitation transfer of 9-phenylanthracene dissolved in the room temperature ionic liquid 1-methyl-3-octylimidazolium chloride was measured at room temperature. Models for the excitation transfer were computed for an unstructured solvent (isotropic model), and a nanostructurally organized solvent model using spheres to represent the hydrophobic domains. The spectroscopic observables were computed, and shown that the excitation transfer can differentiate the structured and unstructured models for sufficiently large sphere sizes. When compared to the time correlated fluorescence data for the 9-phenylanthracene in the viscous ionic liquid, an upper limit of about 6\AA radius was proposed for the size of any nanostructural organization, should it exist.

Because the isotropic model is effectively a subset of the clustered sphere model, no model selection or inference can be taken from the regularization approach. Other statistical methods, using the Bayes factors and Jeffry's criteria, have the ability to choose which of the models is most supported by the data. Future work intends to utilize the approach to quantify the strength at which the evidence favors the more expanded clustered model over the isotropic model, which seems to adequately fit the data under reasonable parameters.

5.6 Acknowledgements

The author would like to acknowledge Greg von Winckel of Karl-Franzens Universität for routines used to perform numerical integration. Daniel Rosenfeld of Stanford University gave important commentary.

5.7 References

- (1) Hu, Y.-F.; Liu, Z.-C.; Xu, C.-M.; Zhang, X.-M. *Chem. Soc. Rev.* **2011**.
- (2) Castner, E. W.; Margulis, C. J.; Maroncelli, M.; Wishart, J. F. *Annual Review of Physical Chemistry* **2011**, 62, 85.
- (3) Wishart, J. J. *Phys. Chem. Lett.* **2010**, 1, 1629.
- (4) Hayes, R.; Warr, G. G.; Atkin, R. *Phys. Chem. Chem. Phys.* **2010**, 12, 1709.
- (5) Wang, Y.; Voth, G. A. *Journal of the American Chemical Society* **2005**, 127, 12192.
- (6) Canongia Lopes, J. N. A.; Pádua, A. A. H. *J. Phys. Chem. B.* **2006**, 110, 3330.
- (7) Yanting, W.; Voth, G. A. *J. Phys. Chem. B* **2006**, 110, 18601.
- (8) Mandal, P. K.; Sarkar, M.; Samanta, A. *J. Phys. Chem. A* **2004**, 108, 9048.
- (9) Shigeto, S.; Hamaguchi, H.-o. *Chem. Phys. Lett.* **2006**, 427, 329.
- (10) Triolo, A.; Russina, O.; Bleif, H. J.; Cola, E. D. *J. Phys. Chem. B* **2007**, 111, 4641.
- (11) Triolo, A.; Russina, O.; Fazio, B.; Appetecchi, G. B.; Carewska, M.; Passerini, S. *J. Chem. Phys.* **2009**, 130, 164521.
- (12) Pott, T.; Meleard, P. *Phys. Chem. Chem. Phys.* **2009**, 11, 5469.
- (13) Russina, O.; Triolo, A.; Gontrani, L.; Caminiti, R.; Xiao, D.; Hines, L. G.; Bartsch, R. A.; Quitevis, E. L.; Pleckhova, N.; Seddon, K. R. *J. Phys.-Condes. Matter* **2009**, 21.

- (14) Greaves, T. L.; Kennedy, D. F.; Mudie, S. T.; Drummond, C. J. *J. Phys. Chem. B* **2010**, *114*, 10022.
- (15) Hardacre, C.; Holbrey, J. D.; Mullan, C. L.; Youngs, T. G. A.; Bowron, D. *T. J. Chem. Phys.* **2010**, *133*.
- (16) Annapureddy, H. V. R.; Kashyap, H. K.; De Biase, P. M.; Margulis, C. J. *J. Phys. Chem. B* **2010**, *114*, 16838.
- (17) Wakasa, M.; Yago, T.; Hamasaki, A. *J. Phys. Chem. B* **2009**, *113*, 10559.
- (18) Aoun, B.; Goldbach, A.; Gonzalez, M. A.; Kohara, S.; Price, D. L.; Saboungi, M.-L. *J. Chem. Phys.* **2011**, *134*, 104509.
- (19) Fruchey, K.; Fayer, M. D. *J. Phys. Chem. B* **2010**, *114*, 2840.
- (20) Coleman, S.; Byrne, R.; Minkovska, S.; Diamond, D. *J. Phys. Chem. B* **2009**, *113*, 15589.
- (21) Xiao, D.; Hines, L. G.; Bartsch, R. A.; Quitevis, E. L. *J. Phys. Chem. B* **2009**, *113*, 4544.
- (22) Gochanour, C. R.; Andersen, H. C.; Fayer, M. D. *J. Chem. Phys.* **1979**, *70*, 4254.
- (23) Gochanour, C. R.; Fayer, M. D. *J. Phys. Chem.* **1981**, *85*, 1989.
- (24) Ediger, M. D.; Domingue, R. P.; Fayer, M. D. *J. Chem. Phys.* **1984**, *80*, 1246.
- (25) Ediger, M. D.; Fayer, M. D. *J. Phys. Chem.* **1984**, *88*, 6108.
- (26) Ediger, M. D.; Domingue, R. P.; Peterson, K. A.; Fayer, M. D. *Macromolecules* **1985**, *18*, 1182.
- (27) Klafter, J.; Blumen, A. *Journal of Luminescence* **1985**, *34*, 77.

- (28) Baumann, J.; Fayer, M. D. *J. Chem. Phys.* **1986**, 85, 4087.
- (29) Huber, D. L. *Physical Review B* **1979**, 20, 2307.
- (30) Peterson, K. A.; Zimmt, M. B.; Linse, S.; Domingue, R. P.; Fayer, M. D. *Macromolecules* **1987**, 20, 168.
- (31) Peterson, K. A.; Zimmt, M. B.; Linse, S.; Fayer, M. D. *Acs Symposium Series* **1987**, 358, 323.
- (32) Peterson, K. A.; Zimmt, M. B.; Fayer, M. D.; Jeng, Y. H.; Frank, C. W. *Macromolecules* **1989**, 22, 874.
- (33) Stein, A. D.; Peterson, K. A.; Fayer, M. D. *Chem. Phys. Lett.* **1989**, 161, 16.
- (34) Marcus, A. H.; Diachun, N. A.; Fayer, M. D. *J. Phys. Chem.* **1992**, 96, 8930.
- (35) Hussey, D. M.; Keller, L.; Fayer, M. D. *Mol. Cryst. Liq. Cryst. Sci. Technol. Sect. A-Mol. Cryst. Liq. Cryst.* **1996**, 283, 173.
- (36) Marcus, A. H.; Fayer, M. D. *J. Chem. Phys.* **1991**, 94, 5622.
- (37) Forster, T. *Ann. Phys.* **1948**, 2, 55.
- (38) Peterson, K. A.; Fayer, M. D. *J. Chem. Phys.* **1986**, 85, 4702.
- (39) Ediger, M. D.; Fayer, M. D. *J. Chem. Phys.* **1983**, 78, 2518.
- (40) Ediger, M. D.; Fayer, M. D. *J. Chem. Phys.* **1983**, 78, 2518.
- (41) Hemenger, R. P. a. P., R. M *J. Chem. Phys.* **1973**, 59, 4064.
- (42) Bojarski, C.; Dudkiewicz, J. *Chem. Phys. Lett.* **1979**, 67, 450.
- (43) Singh, T. K., A. *J. Solution. Chem.* **2009**, 38, 1043.
- (44) de Haro, M. L.; Santos, A.; Yuste, S. B. *J. Chem. Phys.* **2006**, 124.

- (45) Carroll, R. J., Ruppert, D., and Stefanski, L. A. *Measurement Error in Non-linear Models*; CRC: Boca Raton, FL, 1995; Vol. 63.
- (46) Li, B. a. G., P. *Statistica Sinica* **2006**, *16*, 411.
- (47) Kim, T.; Li, H. B.; Lian, J. B.; Jin, H. H.; Ma, J. M.; Duan, X. C.; Yao, G.; Zheng, W. J. *Cryst. Res. Technol.* **2010**, *45*, 767.
- (48) Zhou, Y.; Antonietti, M. *Chemistry of Materials* **2003**, *16*, 544.
- (49) Wheatley, P. S.; Allan, P. K.; Teat, S. J.; Ashbrook, S. E.; Morris, R. E. *Chemical Science* **2010**, *1*, 483.

Appendix 1: Ti:Sapphire Oscillator System

A1.1 Introduction

The heart of almost every modern ultrafast spectroscopy setup is the Ti:Sapphire oscillator. No other system can reliably generate femtosecond optical pulses with the reliability, compactness, and cost levels that Ti:Sapphire affords. This chapter describes the basic concepts and construction of a Ti:Sapphire oscillator and regenerative amplifier system. These were constructed to update a failing system on the Optical Kerr Spectroscopy setup. Emphasis is placed on the specific procedures and knowledge gained during the construction of the system. The designs for both the oscillator and chirped pulse amplifier were taken from Gottke ¹, with various levels of upgrade and modification. Due to a significant amount of accumulated change, most dimensions and distances have been updated to reflect the current configuration.

A1.2 Theoretical Background

The Ti:Sapphire oscillator employs two complementary characteristics of the Ti:Sapphire gain medium – large gain bandwidth and strong non-linear index of refraction. For any optical system, the time-bandwidth product is a fundamental limit of system performance, expressed as

$$\Delta\tau\Delta\nu = .44 \tag{A1.1}$$

This results from the conjugate variable nature of the time and energy, and requires that short operation light generation will require a large gain bandwidth. Due to the vibronic coupling of the Ti^{+3} lattice sites to the sapphire matrix, the energy levels are significantly broadened. This leads to the large gain bandwidth required for generating short optical pulses. A large gain bandwidth in itself will not generate ultrafast pulses without the

addition of a second component which provides mode-locking. While many less desirable mechanisms are available of mode-locking, the intrinsic non-linear index of refraction can be used to passively mode-lock the Ti:sapphire. By introducing an aperture effect, either physically or via overlap with the pumping volume of the gain medium in concert with control over the group velocity dispersion, it is possible to make very short pulses at high repetition rates and moderate powers. Owing to the broadband nature of ultrafast lasers, dispersion compensation is required to maintain short pulses. The primary source of dispersion is the Ti:Sapphire rod, through which the nascent pulses make numerous round trips. To offset this, a prism pair is oriented in a negative dispersion configuration. The amount of negative dispersion is largely fixed, and then the additional dispersion is added using the glass of the prisms themselves to balance positive and negative dispersion.

A1.3 Oscillator Construction

The following sequence of events details a total alignment procedure which largely replicates the experiences of constructing the system from scratch. The first step is to rotate the normally vertically polarized pump laser to a horizontal polarization used to simplify table top geometries. Nd:VO₄ is used as the pump material because it has outstanding mode characteristics and power stability. The former is especially necessary as the ultimate mechanism for passive Kerr lens mode-locking is the differential overlap between the pump mode and the mode-locked and unmode-locked mode. For this reason, it is recommended that the pump laser be profiled. Absent a dedicated beam profiler, a razor blade mounted on a translation stage with a power meter can be used to get an approximate beam shape. As the razor blade is introduced into the beam, the

power is measured as a function of position. For a Gaussian beam, the functional form of this operation is:

$$\frac{I}{I_o} = (1 + \operatorname{erfc}(\frac{\sqrt{2}}{w_o} z)) / 2 \quad (\text{A1.2})$$

Deviation from this shape, especially asymmetry between the positive and negative tails may indicate the presence of a satellite pulse caused by damage to an internal optic in the pump laser. The beam profiling should be carried out at a distance comparable to the ultimate position of the Ti:sapphire rod, because the satellite beams can have very different divergences.

Assuming a good pump mode, the next step is to level the beam with the table and shoot it down a row of screw holes on the table. This can be achieved with two equally leveled irises on posts. Although not strictly required, these facilitate future alignments. With the laser beam leveled, the next step is to introduce the first curved mirror C1, focusing lens L1, crystal X1, and second curved mirror C2 into the path of the pump beam. For the case of C1 and L1, the optics are repositioned until the pump beam emerges undeflected, as measured by the second iris. The distances should correspond roughly to those in the design, and will be optimized later. The crystal is introduced, and due to the oblique angle, will translate the beam a few millimeters. At this point, it is possible to rotate the crystal to Brewster's angle by minimizing the intensity of the reflection off the crystal front surface. The second curved mirror is then introduced at its appropriate position and moved until the beam is returned to the second iris. This procedure ensures that both curved mirrors are slightly off center with respect to the pump beam. This allows one to rotate the mirror should damage occur without changing the alignment significantly.

With these optics in place, there should be a relatively collimated beam of fluorescence from the crystal being reflected off of each curved mirror. The angle of the curved mirrors should be set to 22° , which is used to compensate for the astigmatism caused by a Brewster cut rod. This setting is relatively insensitive, and can be set using a protractor. Aligning the green down a row of holes makes this measurement much easier. The fluorescence emission from the rod can then be used to roughly set the positions of the two end mirrors, and prisms. The angles of the two prisms are set to minimum deviation first using the fluorescence. The condition for minimum deviation is dependent on wavelength, so an infrared viewer should be used to minimize the strong bias towards blue wavelengths of the eye's photoresponse. With the fluorescence shining through the prism, adjust the angle until a minimum in the angle of deflection is found. This is the angle of minimum deviation, and for a Brewster prism, corresponds to Brewster's angle for the beam crossing through the prism. Setting this condition accurately does two things. First, it minimizes the loss contribution from reflections off the uncoated prism. More importantly, it is a fairly sensitive way to ensure both prisms are set at the same angle. To achieve stable operation, chirp compensation is highly important. Any mismatch in the relative angle of the two prisms will contribute to higher order dispersions. In addition to being uncompensatable downstream, and therefore leading to longer pulses, a large amount of uncompensated chirp will disrupt the mode-locking. This will lead to unstable laser operation.

With all components in the laser, it is possible to begin adjusting the laser parameters to achieve CW lasing. First, adjust the translation of the crystal so that the fluorescence spot on the second prism is a fairly collimated beam of approximately 4-5mm diameter.

Any movement in the crystal position should be accompanied by adjustments of the lens position to keep the focus in the center of the crystal. Then, use the output coupler to retroreflect the fluorescence onto itself, first at the curved mirror, and then further downstream. By blinking the fluorescence between the curved mirror and output coupler, it is possible to see the retroreflection all the way at the second prism. Adjust the position of the second curved mirror until the size of the retroreflected fluorescence is approximately the same as the fluorescence spot that is directly from the rod. Also, adjust the aiming so that both beams are on top one another. Using this fluorescence beam, retroreflect the fluorescence off the high reflector. This is difficult to do accurately, so a rough adjustment is sufficient. In this configuration, the laser should be capable of lasing. Increase the pump power to 4.5W, and watch the output coupler with an infrared viewer. Because the high reflector is difficult to accurately set a priori, this is the adjustment that should be used to achieve lasing. As soon as the cavity is largely aligned, a bright spot will appear on any mirror, signifying lasing. The task is to simultaneously scan both angular deflections of the high reflector while watching for signs of lasing. This can be a slow process. It is recommended that after several minutes of scanning, one attempts to retroreflect the fluorescence from the high reflector to return the system to a near-accurate configuration. If numerous sweeps do not result in lasing, check for clipping on the prisms. The prisms should be translated so that they clip 50-70% of the visible fluorescence. A higher reflectivity optic can also be substituted for the output coupler to achieve first light. Once the system is lasing, it should be peaked on power by adjusting the end mirrors. The axial translation of the lens can also be adjusted,

but it is recommended that otherwise the lens not be adjusted, to keep the alignment close to the table alignment.

Once optimized in CW operation, the cavity is altered to initiate mode-locking. The mechanism for passive mode-locking is the differential overlap between the CW and mode-locked cavity mode with the pump volume resulting from the non-linear Kerr lens. The distortion in cavity mode is created by extending the inner cavity (the separation between the two curved mirrors). Based on numerical simulation of the cavity, there are two ² zones of stability, between which the cavity becomes completely destabilized and will not lase, either CW or mode-locked. The existence of a zone of stability results from the asymmetry in length of the two arms of the cavity, and is beneficial in that it allows the researcher to ensure the laser is operating in the optimal regime. The zone of choice is the outer zone of stability, which is the zone with the second curved mirror furthest from the crystal. This region is known to give the best mode shape, pulse duration, and stability. But within the second zone of stability, the region of mode-locking is with the curved mirror closest to the crystal. Beginning from the initial configuration, the tweaking of the laser in CW should be with the curved mirror well within the second zone of stability. The process of priming the cavity for mode-locking is therefore to walk the cavity toward the inner boundary of the second zone of stability. The strongly coupled degrees of freedom require that this process be done slowly, in many iterations. The second curved mirror is translated slightly toward the crystal, and then the CW power is peaked by adjusting the end mirrors. This process is repeated until the CW mode begins to appear vertically elongated, and the laser spectrum should begin to jump between colors. It is normal for the CW power to decrease as the curved mirror is

translated, owing to the changing overlap with the pump volume. The jumping in spectrum results from the coupling of cavity modes, which are beginning to interact through the non-linear coupling of the crystal. If the second curved mirror was substantially translated, it may be necessary to adjust the position of the crystal within the inner cavity, and also the lens z translation to maintain focus in the center of the crystal. The coupling of these two parameters makes adjusting the crystal translation difficult. A good heuristic is to place it exactly between the two curved mirrors, and then make very small adjustments to optimize power.

When evidence for the potential to mode-lock is present, the prisms are set approximately and mode-locking can be attempted. The prism closest to the crystal should be withdrawn until about half of the fluorescence is clipped by the apex of the prism. This minimizes the amount of glass while ensuring that the laser beam will not also be clipped. The second prism is then nearly fully withdrawn from the laser beam. It is important that the spring-loaded direction of the translation stage mounting the second prism allows more glass to be introduced by sliding the stage against the spring. The technique for achieving mode locking is an art that is difficult to describe. Even if the laser cavity were fully optimized for mode locking, the system will not mode lock on its own. A perturbation must be introduced whose Fourier components included the overlap of many modes in phase. This creates a partial soliton, which is sufficient to non-linearly feedback and dynamically shift the system to mode-locking. The easiest way to do this is with the second prism translation. By jarring it suddenly to increase the dispersion, the cavity receives an impulsive perturbation which ideally contains all components of mode phase relations. With this shock, the system relaxes via cavity

oscillations. These relaxations can lead to soliton formation, and thus mode-locking. When first initiating mode-locking, there is an additional component in needing to also find the optimal dispersion. An easy way to do this is to jar the prism into the beam, and then hold it against the spring at some point further into the laser. By watching the spectrum and cavity relaxation on a fast photodiode, biofeedback can be used to adjust the location in the beam until mode-locking occurs. It is important to try several speeds and positions in jarring the prism. The same apparent combination may fail many times before resulting in mode-locking, even in an optimized system. At the point at which the laser mode-locks, the translation stage for the second prism should be advanced to hold the prism in the position currently being held by hand. This corresponds to the approximately correct amount of dispersion, which will be adjusted later.

If repeated attempts fail to generate mode-locking, the second curved mirror should be further translated toward the crystal, and the process repeated. If the system mode-locks, a number of striking changes should result. The mode shape should shift from a vertically elongated ellipse to a smaller circle. The power should ideally increase, and the spectrum should broaden substantially and become stable. These are all signatures of successful mode-locking. If the system remains mode-locked for an extended period of time, the system can be tweaked in this configuration to increase power. There are a number of parameters that must be optimized to guarantee long-term oscillator stability. One is the total power, which is dominated by the cavity alignment and pump overlap. The former is optimized by adjusting the cavity end mirrors to maximize power. Because it is difficult to effectively translate the cavity mode relative to the pump volume, adjustments to the cavity end mirrors should be periodically alternated with minor

adjustments to the pump focusing lens. These alternations in adjustment parameters will enhance the convergence of cavity parameters while maintaining approximate alignments to avoid clipping.

A second parameter of adjustment is the CW discrimination, which is the difference of circulating power between the mode-locked and CW cavity operation. This parameter primarily affects long term stability of the oscillator. If the discrimination is low, then there is not a significant selection for mode-locked operation. Small perturbations will therefore be able to unmode-lock the systems. The power discrimination is dominated by the translation of the second curved mirror. The cavity stability parameter is strongly dependent on the focusing characteristics of the inner cavity, comprised of the two curved mirrors and the effective Kerr lens. The addition of a Kerr lens tends to expand the zone of stability, such that translating the second curved mirror toward the crystal will move the cavity into a zone where mode-locking is stable but CW operation is not. Therefore, continuing to translate the second curved mirror toward the crystal will increase the CW power discrimination. There are two difficulties in this process. The first is that the cavity must initially stably operate in CW mode to be able to mode-lock the system. Too little power, and an insufficient Kerr lens will occur in the relaxation oscillations to initiate mode-locking. This prevents moving the inner cavity to such dimensions where mode-locked operation is stable but CW is completely unstable. The second confluence is that the alignments of the cavity in CW and mode-locked operation often differ slightly due to the Kerr lensing. The asymmetry in the cavity lengths is partially to blame. Thus, creating too much CW discrimination will migrate the system into a completely CW unstable operating regime if the system is mode-locked and then optimized on mode-lock

power. For these reasons, a power discrimination of 100mW between CW and mode-locked operation has been found sufficient to maintain long term stability while avoiding the problems associated with excessive power discrimination. This is set by the translation of the second curved mirror.

In addition to total power and CW discrimination, the final adjustment is for spectrum. The spectrum is important for a number of reasons. First, the total bandwidth of the oscillator limits the time resolution possible for the emitted pulses. Too little bandwidth and the system will not generate short pulses. The bandwidth is tempered by the geometry of the stretcher, which generally limits the wavelengths to about 50nm of bandwidth. But even if the spectrum will ultimately be lost in the stretcher, a broad laser spectrum is desirable for oscillator power stability. More bandwidth means shorter pulses, which gives a stronger Kerr lens. This will tend to stabilize the oscillator, ensuring long running stability without the need for frequent intervention and tweaking. The laser bandwidth is dominated by the dispersion control in the two prisms. At a fixed approximate prism separation, as afforded by the cavity, dispersion is controlled by over-compensating for the crystal dispersion in the negative dispersion from the prism separation, and then introducing additional chirp from the prism glass itself. For maximally short pulses, this should be minimized because the higher order chirps from the nonlinear dispersion in any material will broaden pulses in a manner than cannot be compensated for in the compressor. Within the approximately compensating prism separation, the addition of glass will tend to compensate the chirp and minimize the output pulse duration. This is easily monitored in the laser spectrum. At substantial negative dispersion, corresponding to insufficient prism glass, the spectrum will be fairly

narrow and centered around the gain maximum of 800nm. As glass is introduced, the laser bandwidth will increase as the pulses shorten. As the laser approaches zero dispersion, the operating frequency will begin to shift to the blue, and eventually bifurcate into a large pulse at around 750nm, and a smaller pulse at 800nm. This signifies the approach to zero dispersion. Zero dispersion is actually undesirable for oscillator stability, as it is maximally sensitive to small perturbations. The cavity is therefore operated at a slightly negative dispersion. Because there is substantial hysteresis in the cavity operation, the procedure for setting the chirp is to increase the prism glass until the spectrum bifurcates. The glass is then backed off until the spectrum coalesces at 800nm, yielding a broad, single peak. In this configuration, the cavity should be stable for months, with a power of greater than 300mW and pulse to pulse fluctuations of less than 0.1% RMS.

While tweaking the laser, it is important to continually monitor the laser spectrum, intensity, pulse train, and mode. Each can indicate misbehavior in the cavity, and help narrow down the source of problem. The power is the chief tool for manipulating cavity alignment. In CW operation, this is the only metric that needs to be closely examined. But when tweaking the mode-locked cavity, the adjustments made to increase power must always be weighed against changes in the laser spectrum. If the laser is operating with substantial bandwidth, it is common for an adjustment, especially in the plane of the table, to increase the total output power at the expense of laser bandwidth. By narrowing the bandwidth, the overlap with the gain spectrum is improved, and therefore the total power. For this reason, adjustments that create this situation are not actually improving the cavity alignment, but playing different mis-alignments against one another. The

response to this is vigilant monitoring of the spectrum, with frequent iterations between the angular adjustment and the prism dispersion. By returning the bandwidth to its previous amount, it is possible to see if the angular adjustment actually improved the total output power.

The mode is important to monitor, although less frequently than the other metrics. Its primary use is in determining which zone of operation the mode locked laser is in. In the second stability zone, the mode will be round to vertically elliptical. But in the inner stability region, a triangular mode known as the Angelfish mode can result. Although the laser will be reasonably stable, the poor mode shape coupled with the heightened sensitivity to environmental fluctuations makes this zone undesirable. The output mode can also quickly diagnose clipping, especially with the apex of the prism.

The output of a fast photodiode is invaluable in monitoring the progress of laser development. Toward the final stages of adjustment, the target shifts from optimizing power to optimizing laser stability. This can be slightly difficult to follow in real time, as small air currents in the room are generally sufficient to cause noticeable intensity fluctuations that damp when the laser is covered. None the less, it is generally sufficient to determine if a polishing adjustment has potentially upset the pulse to pulse stability. It is also invaluable in diagnosing two common problems. The first is double-pulsing, where two interacting pulse trains are circulating in the cavity. This can be seen as two distinct pulses on the photodiode if the separation is large, or sinusoidal modulation of the laser spectral envelope if the pulses are close together (being the Fourier transform of two nearby Delta functions). If the cavity is double-pulsing, small adjustments to the output coupler will usually disrupt this. The cavity can then be retweaked at the new

output coupler alignment. The second phenomena is self q-switching, which is a nonlinear process in the crystal resulting from poor circulating power. Similar to q-switching in a solid state laser, the modulation of phases helps increase the Kerr lensing to maintain mode locking. Self q-switching is readily evident on the fast photodiode, being a wave-like undulation in the pulse train occurring on a couple of microsecond period. The solution to self q-switching is to either improve the cavity alignment to increase the circulating power, or increase the pump power. Unless something significant has changed in the cavity, the latter is generally not recommended, as one is likely masking a structural problem in the current alignment of the system.

An important improvement to the oscillator design described above was the shift from 12cm to 10.5cm focusing lens on the pump. Seemingly small, this changes the pump beam waist by almost 20%. The smaller pump volume makes the conditions for mode locking more severe. While this makes setting the system up initially more challenging, it pays dividends by greatly improving the long term stability of the oscillator. It also allows for lower pumping powers (3W vs 4.5W) and a contaminant increase in pump diode lifetime. The only negative consequence of this change was a significant increase in the amount of higher order mode power. The TEM₀₀ mode contains the majority of the laser power, but higher order modes can be populated in very broadband operation. The more diffuse higher order modes partially compensate for the difference in chirp resulting from non-linear dispersion in the crystal and glass. Evidence for higher order modes shows up as bright decoration around the central laser, frequently looking like a vertically oriented cross. Substantial amounts of this light will miss the prism and be lost, but enough is carried with the laser exiting the cavity that spatial filtering is

required. This is not so much to improve the mode quality for better amplifier function as it is to allow collimation of the beam. Without good collimation, the divergence in the stretcher will create uncompensatable chirp, degrading ultimate time resolution.

Another discovery while setting up the oscillator is the sensitivity to mirror coatings. There are two types of ultrafast high reflectors. The first are relatively narrow band, although still sufficient to realize 70-80nm of bandwidth. The second, more recent, coated mirrors have very broad reflectivities with very low phase pick-up. In theory, these should be excellent for creating the shortest pulses. However, the ultra-broadband coating comes at the expense of high frequency oscillation in the reflectivity and phase. Because mode-locking involves achieving constant phase between nearby colors, these fluctuations can actually be very destructive to stable mode-locking. It is therefore recommended that the narrower band mirrors be used in the cavity, where many round-trips accumulate this error. Outside the cavity, the broader band mirrors can be use without problem.

A1.4 References

- (1) Gottke, S. *Thesis, in the Department of Chemistry, Stanford University*
2002.
- (2) Liao, Y.-H.; Unterreiner, A. N.; Arnett, D. C.; Scherer, N. F. *Appl. Opt.*
1999, 38, 7386.

Appendix 2: Additional Experiments

A2.1 Introduction

The preceding chapters reflect several successful experiments on ionic liquids. Since I believe the thesis should reflect the full body of work in my graduate career, this section details some experiments considered and undertaken at various levels. These ideas are fair game for anyone to continue or take inspiration from. Background on any specific experiment is kept brief; the reader is therefore encouraged to seek additional background in the appropriate citations.

A2. 2 Berry Psuedorotation in Iron Pentacarbonyl using 2D-IR

This work was undertaken in 2006, with help from Ilya Finkelstein. The work was abandoned when similar results were announced by Charles Harris¹. The goal was to use exchange 2D-IR to measure the rate of Berry pseudorotation in the trigonal bipyramidal complex FeCO_5 . This is a textbook inorganic example of a fluxional complex, meaning the normally differentiable axial and equatorial ligands rapidly re-orient. For many systems this rate of reorientation is measureable using NMR, but the case of FeCO_5 had eluded accurate measurement. An inspection of the FTIR of FeCO_5 shows two peaks, representing the axial and equatorial carbonyls. This means the re-organization is slow enough that the two components are not motionally averaged. 2D-IR exchange has been successfully used in similar instances, including bond rotation and hydrogen bond exchange².

To measure the re-orientation, the time dependence of the 2D cross peaks is measured. A carbonyl is initially labeled by its first interactions with the exciting IR fields. The system is then allowed to evolve, during which time it is possible that the Berry

pseudorotation will exchange it with a carbonyl in a different position. When the carbonyl emits, it will do so at a different frequency, leading to a cross peak in the 2D spectrum. Measuring the time dependence of this process, as well as a number of competing phenomena (vibrational lifetime, orientational relaxation, etc.) allows a kinetic equation to be derived and fit. Initial experiments on FeCO_5 dissolved in CCl_4 showed promise, with cross peaks growing in on a many picoseconds timescale. The compounding difficulty in this experiment is the presence of coherence and population transfer to the cross peaks. When two distinct chemical species are involved in a reaction, there is no pathway for coherence or population transfer – i.e. the modes of the two species are not coupled. This not necessarily the case on the FeCO_5 molecule, where the axial and equatorial modes could easily be coupled.

Demonstrating the absence of this coupling, or quantifying its contribution to subtract from the cross-peaks represents a substantial challenge. Harris et al used DFT calculations to argue that the anharmonic coupling between modes should be negligible. This assertion is questionable, as the ability to calculate these parameters to the requisite accuracy is far from established. Somewhat comforting was the temperature dependence of the Berry pseudorotation in their experiments – which followed simple Arrhenius behavior. Since the coherence transfer rate should be weakly temperature dependent, a substantial contribution from coherence transfer would therefore shift the temperature dependence away from Arrhenius.

A2.3 Photoacid Dynamics in Hydrated Ionic Liquids

This work was carried out in 2008. The hydrated ionic liquid system is a very interesting one. Simulations by Voth³ et. al. indicated interesting behavior in water

miscible ionic liquids as a function of hydration level. The description incorporates the concept of nanoscale heterogeneity as it was understood at the time. Beginning at low hydration levels, the inclusion of small amounts of water tended to increase the degree of nanoscale heterogeneity. The waters were incorporated individually in the hydrophilic network, and for poorly understood reasons, increased the size of the aliphatic regions as sensed by a heterogeneity order parameter. This continued until a mole fraction of about 0.2 water, at which point the water started to aggregate into pools and disrupt the ionic liquid structure.

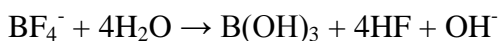
How this hydrated ionic liquid system interacts with protons is interesting for several systems. Ionic liquids have been candidate electrolytes for fuel cells. Their responsibility in this case is to transport the protons from the anode to the cathode. Quantities of merit in this application are the proton mobility, proton carrier density, and electrochemical stability. In addition, there are classes of ionic liquids which are formed by neutralizing a Brønsted acid and base. It follows to question what the proton transport mechanism looks like in this system.

These experiments attempted to use the fluorescence of pyranine dissolved in an appropriate ionic liquid to monitor proton transport. This work is similar to that carried out by Spry et. al. in Nafion⁴. Pyranine, or HPTS, is a strong photoacid, with a ΔpK_a of 7. Photoexcitation of the protonated dye molecule leads to a strong change in the acidity, sufficient to release the proton into the surrounding medium. If proton carriers are nearby, the proton is conducted away from the dye by the transport mechanism of the proton in that solution. However, the fully dissociated pyranine has a -4 charge, so the proton also feels a strong attraction attempting to return it to, and thereby neutralize, the

pyranine. This is known as geminate recombination. The process can be modeled, or compared to model systems.

In these experiments, pyranine was dissolved in water/ionic liquid solutions of various concentrations, using 1-butyl-3-methylimidazolium tetrafluoroborate and 1-butyl-3-methylimidazolium dicyanamide. These ionic liquids were chosen because they were miscible with water, and have been elsewhere well studied as binary water mixtures. The protonated dye was excited, and the deprotonated fluorescence measured at the magic angle to remove rotational dynamics. Initial experiments showed single exponential decays of the deprotonated state, indicating the absence of geminate recombination at all but the highest water concentrations.

There were serious complications that came about when conducting these experiments. To achieve a sufficient level of signal, the photoacid must be in the protonated state when it is excited. For pyranine, which has a ground state pKa of 7, solutions of similar pH are required. At first glance, simple solutions with water and ionic liquid should have a pH similar to 7. But examination with absorbance indicated the dye was almost fully deprotonated. To compensate, ionic liquid solutions using an acetate buffer were prepared, which should have a nominal buffered pH of 5. In theory, this should be sufficient to almost completely protonate the dye; but again the absorption spectrum showed an almost fully deprotonated dye. In fact, it took a sizeable amount of concentrated HCl to titrate the solution to the deprotonated state. The cause of this was found to be the intrinsic basicity of the ionic liquid themselves. Tetrafluoroborate can undergo a hydrolysis reaction as



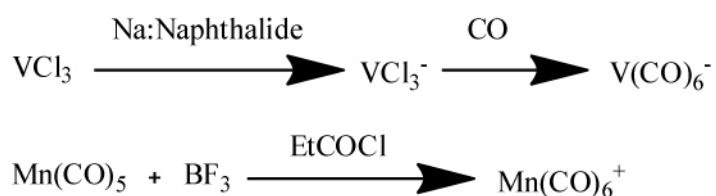
Although the equilibrium constant for this reaction is slight, the very high concentration of ionic liquid leads to appreciable amounts of OH^- when compared to the very low concentration of water and dye. The amount of buffer required to remove this contribution was substantial, which makes the results questionable as to their validity in a system without the large concentration of buffer ions. While dicyanamide does not itself undergo hydrolysis, the anion is a weak conjugate base, leading to similar problems.

Although photoacids are available with groundstate pKas sufficiently high to operate in these conditions, most absorb light at a wavelength too short to be excitable by the Mai Tai (being less than 355nm). Others are excitable, but lack the strong negative formal charge of pyranine. This will diminish the strength of geminate recombination. The experiment essentially became a combinatorial problem of testing ionic liquids and dyes for compatibility. After limited success, it was suspended to pursue other fluorescence work. An interesting development arose subsequent to the project's suspension, with researchers have prepared an ionic liquid using pyranine as the anion⁵. The ionic liquid has been demonstrated as a fluorescent pH indicator. If it is sufficiently miscible with water, this ionic liquid may enable studies similar to those described above to be carried out. One other concern is the influence of ionic screening on the geminate recombination. The prevalence of ions will be expected to screen the HPTS charge, on a length scale similar to the Bjerrum length. This was estimated from molecular parameters to be 5nm. Although this will not necessarily prevent an accurate measurement, it will limit the experiment to proton diffusivities that cannot remove the proton from the unscreened field of the dye.

A2.4 2D-IR measurement of Carbonyls in Ionic Liquids

This work was conducted in 2007, and based upon the measurement by Owrutsky et.al. of ion vibrational lifetimes in some prototypical ionic liquids⁶. It was found that W(CO)_6 had an extremely long vibrational lifetime, greater than 100ps. The goal was to use this long lifetime to probe the spectra diffusion over a very long time. The dynamics measurable in a 2D-IR experiment are always limited by the length over which the vibrations can remain excited. This is typically less than 10ps, which limits the experimental window to 50ps. The spectral diffusion of a solute is related to the time scales over which a heterogeneously broadened line explores the various ensembles. Again based on the current ideas of nanoscopic heterogeneity, the question was what timescales would a solute spend in each environment? Since the carbonyl vibration shifts frequency depending on the polarity of the solvent, it was assumed that the migration of the small metal complex between different domains should dominate the spectral diffusion. Because the domains are expected to be long lived and the viscosity high in ionic liquids, a long lifetime was expected to be necessary.

This idea was expanded upon by using additional metal carbonyl probes. In addition to W(CO)_6 , the charged metal complexes V(CO)_6^- and Mn(CO)_6^+ can both be synthesized as



These two complexes should have similar lifetimes. Being ionic, they would be expected to interact with a different part of the nanostructured ionic liquid environment. By

comparing the spectral diffusion in the charged and uncharged metal carbonyl probes, a comparison might be made of the two environments. Since these metal carbonyls are somewhat similar to a number of homogeneous catalysts, especially those used for hydroformylation, the comparison may provide some useful information about the environment in which a catalyst will reside. If the catalyst truly is segregated into a particular domain, then its availability to reagents will depend on their preference for environment, and the mobility between phases. An additional idea was to use dicyanamide as a vibrational probe, since dicyanamide ionic liquids can be easily made. To avoid excitation transfer in the concentrated dicyanamide solution, isotopic substitution would be made to shift the vibrational frequency. Using ^{13}C labeling, it was calculated that the dicyanamide vibration could be shifted 70cm^{-1} , which is sufficient to resolve it from the unsubstituted parent.

The FTIR for $\text{W}(\text{CO})_6$ was a single, relatively narrow peak for 15 cm^{-1} . When T_w was varied, it was found that by 8ps, the spectral diffusion was almost complete. This is somewhat surprising, because it indicates that in 8ps the carbonyl has sampled all of its environments. There are a number of possible explanations for this. It could indicate that the complex was only in a single domain, in which the metal could quickly sample all configurations. It could also indicate that the vibration is not particularly sensitive to its surrounding environment. It could also indicate the absence of any large scale structure, and such that the carbonyl can fairly quickly sample the entire line.

At this point, the project went into stasis as my time was re-directed toward the laser build project. Some attempts were made at the $\text{V}(\text{CO})_6^-$ synthesis, but faulty equipment admitted air into the final product. Spectroscopy on the residue indicated a likely

successful synthesis. The more challenging $\text{Mn}(\text{CO})_6^+$ was not attempted. The very fast spectra diffusion is still somewhat of an anomaly, although the shift in opinion about the structure of ionic liquids may mean that probe is simply spectrally diffusing in a fairly homogeneous environment; therefore displaying behavior characteristic of other simple solvent systems.

Another idea in a similar vein was to do a probe free measurement using the $-\text{CN}$ stretch of dicyanamide, since dicyanamide ionic liquids are easy to come by. To avoid the problems of excitation transfer, ^{13}C isotopic substitution would be used to shift the vibration about 70cm^{-1} . Several attempts were made at synthesizing the isotopically substituted dicyanamide. Starting from K^{13}CN , it was easy to make and isolate isotopically substituted cyanogen bromide. The first attempt was a solid state synthesis to react the cyanogen bromide with NaNH_2 , to avoid the reactivity of the amide. This approach was unsuccessfully applied, likely due to reactions with the neoprene ball mill. Another attempt was to react the cyanogen bromide with cyanamide in methanol. This would lend itself to an asymmetrically substituted dicyanamide, which would increase the shift and also disrupt any mixing between the symmetric and asymmetric $-\text{CN}$ stretch. The reactivity of the methanol should be slow enough to prevent the degradation of the cyanogen bromide to cyanide and bromide, which is a problem in protic solvents. Multiple attempts were unsuccessful, and the project was suspended to focus on fluorescence work.

A2.5 References

- (1) Cahoon, J. F.; Sawyer, K. R.; Schlegel, J. P.; Harris, C. B. *Science* **2008**, *319*, 1820.
- (2) Zheng, J.; Fayer, M. D. In *Ultrafast Phenomena XV*; Corkum, P., Jonas, D. M., Miller, R. J. D., Weiner, A. M., Eds.; Springer Berlin Heidelberg: 2007; Vol. 88, p 323.
- (3) Jiang, W.; Wang, Y. T.; Voth, G. A. *J. Phys. Chem. B* **2007**, *111*, 4812.
- (4) Spry, D. B.; Goun, A.; Glusac, K.; Moilanen, D. E.; Fayer, M. D. *Journal of the American Chemical Society* **2007**, *129*, 8122.
- (5) Yung, K. Y.; Schadock-Hewitt, A. J.; Hunter, N. P.; Bright, F. V.; Baker, G. A. *Chem. Comm.* **2011**.
- (6) Sando, G. M.; Dahl, K.; Owrutsky, J. C. *Chem. Phys. Lett.* **2006**, *418*, 402.